Design of Electrodes for Efficient and Selective Electrical Stimulation of Nervous Tissue

by

Bryan Howell

Department of Biomedical Engineering
Duke University

Date:_____

Approved:

_____
Warren M. Grill, Supervisor

_____
Craig S. Henriquez

_____
Dennis A. Turner

_____
John E. Dolbow

_____
Patrick D. Wolf

Dissertation submitted in partial fulfillment of
the requirements for the degree of Doctor
of Philosophy in the Department of
Biomedical Engineering in the Graduate School
of Duke University

2015

ABSTRACT

Design of Electrodes for Efficient and Selective Electrical Stimulation of Nervous Tissue

by

Bryan Howell

Department of Biomedical Engineering
Duke University

Date:_____
Approved:

_____
Warren M. Grill, Supervisor

_____
Craig S. Henriquez

_____
Dennis A. Turner

_____
John E. Dolbow

_____
Patrick D. Wolf

An abstract of a dissertation submitted in partial
fulfillment of the requirements for the degree
of Doctor of Philosophy in the Department of
Biomedical Engineering in the Graduate School of
Duke University

2015

Abstract

Modulation of neural activity with electrical stimulation is a widespread therapy for treating neurological disorders and diseases. Two notable applications that have had striking clinical success are deep brain stimulation (DBS) for the treatment of movement disorders (e.g., Parkinson's disease) and spinal cord stimulation (SCS) for the treatment of chronic low back and limb pain. In these therapies, the battery life of the stimulators is much less than the required duration of treatment, requiring patients to undergo repeated battery replacement surgeries, which are costly and obligate them to incur repeatedly the risks associated with surgery. Further, deviations in lead position of 2-3 mm can preclude some or all potential clinical benefits, and in some cases, generate side-effects by stimulation of non-target regions. Therefore, despite the success of DBS and SCS, their efficiency and ability to activate target neural elements over non-target elements, termed selectivity, are inadequate and need improvement. We hypothesized that altering the geometry and configuration of the electrode designs currently used in DBS and SCS can lead to improvements in efficiency and selectivity.

We combined computational models of volume conduction in the brain and spine with cable models of neurons to design novel electrode configurations for efficient and selective electrical stimulation of nervous tissue. We measured the efficiency and selectivity of prototype electrode designs in vitro and in vivo. Stimulation efficiency was increased by increasing electrode area and/or perimeter, but the effect of increasing perimeter was not as pronounced as increasing area. Cylindrical electrodes with aspect

(height to diameter) ratios of > 5 were the most efficient for stimulating neural elements oriented perpendicular to the axis of the electrode, whereas electrodes with aspect ratios of $\leq$ 2 were the most efficient for stimulating parallel neural elements.

Stimulation selectivity was increased by combining two or more electrodes in multipolar configurations. Asymmetric bipolar configurations were optimal for activating parallel axons over perpendicular axons; arrays of cathodes with short interelectrode spacing were optimal for activating perpendicular axons over parallel axons; anodes displaced from the center of the target region were optimal for selectively activating terminating axons over passing axons; and symmetric tripolar configurations were optimal for activating neural elements based on their proximity to the electrode. The performance of the efficient and selective designs was not be explained solely by differences in their electrical properties, suggesting that field-shaping effects from changing electrode geometry and polarity can be as large as or larger than the effects of decreasing electrode impedance.

Advancing our understanding of the features of electrode geometry that are important for increasing stimulation efficiency and selectivity facilitates the design of the next generation of stimulation electrodes for the brain and spinal cord. Increased stimulation efficiency will increase the battery life of IPGs, increase the recharge interval of rechargeable IPGs, and potentially reduce stimulator volume. Greater selectivity may improve the success rate of DBS and SCS by mitigating the sensitivity of clinical outcomes to malpositioning of the electrode.

Dedication

I dedicate this to my loving parents, Jesse and Doricela Howell, and my devoted partner, Yiwen Wu.

Contents

List of Tables

List of Figures

Acknowledgements

It is rare to have a mentor that not only invests the time and effort to mold his or her mentee into a strong independent investigator but also puts forth additional energy to ensure that his or her mentee has every opportunity to be successful in their future career, whether it is in academia or industry. My advisor, Warren M. Grill, is one of these rare mentors: he granted me the freedom to pursue my own interests, at my own pace; he constantly presented me with opportunities to enrich my prospective career in academia; he was patient and supportive; and all the while, he was always critical of my ideas and work, forcing me to become a stronger and more confident scientist. I am grateful to have had him as an adviser and mentor.

I would also like to thank my committee members, Patrick D. Wolf, Craig S. Henriquez, Dennis A. Turner, and John E. Dolbow, for their valuable suggestions and insights over the years.

Many thanks are also due to the individuals that made the work on spinal cord stimulation (in Chapter 5) possible. Scott Kokones and Greg Schulte, two of the founders of NeuroAccess Technologies, were pivotal in getting their company to sponsor a research grant for our work. Dr. Nandan Lad, a functional neurosurgeon at Duke University and the chief medical officer of NeuroAccess Technologies, conducted the clinical study, provided the clinical data, and helped me better understand the anatomy and organization of the spinal cord and spine. And, Brandon Swan offered his valuable

assistance in coordinating the clinical study and serving as a liaison between our lab and the staff at the Duke University Hospital.

I am also grateful to the members of the Neural Prostheses Lab that enriched my graduate experience at Duke University. First, there were the graduate students: Tianhe Zhang, our local pain expert, who was always willing to disgorge his knowledge of the neural basis of chronic pain, give us the latest reports on the weather and news, and ensure your immune system was always ready to take on a cold virus. Leo Medina, through many discussions, helped me piece together a solid understanding of the frequency domain. Nikki Pelot, the most scrupulous member of our lab, always asked great questions, forcing me to consider alternative ways of looking at things. Meredith McGee, the most energetic member, brought unity to the lab, planning lunches and holiday parties. Christina Behrend was always willing to engage in a conversation about European history, and if your interests were more on neural signal analysis – or what is trending on Reddit – then David Brocker was the man to see.

Second, there were the postdocs, Zachary Danziger, who helped reinvigorate my love for philosophy, Chintan Oza, whose enthusiasm for basic neuroscience was infectious, and Jim Hokanson, who was always optimistic and truly interested to hear about your work.

Third, there were the three research assistants: Christopher Langdale, Brandon Swan, and Gilda Mills. Chris, never, once, turned down a request to help me with animal experiments, which, in-turn helped increase my ability to carry out animal experiments independently. Brandon, when he wasn't satiating our appetites with delicious cakes or

pies, was keeping clinical studies running smoothly in our lab. And, Gilda Mills deserves a great deal of gratitude for her tireless help with setting up and helping with animal experiments over the years, and aiding me with the administrative responsibilities that came with conducting animal experiments.

Finally, there were the two eager undergraduate research assistants, Sagar Naik and Brian Huynh. Without the efforts of these two individuals, I would not have had the time to pursue additional projects that allowed me to expand the scope of my dissertation work. For this, I am truly grateful.

None of this would have been possible without the loving support of my mother, Doricela Howell; my father, Jesse Howell; my aunts and uncles; and my caring partner, Yiwen Wu.

Yiwen has been by my side since the start of graduate school. When I was inundated with work, Yiwen sacrificed her own free time to help me with cooking and cleaning. At times when I was dispirited and I feared my resolve would waver, Yiwen was there to provide mental support – as well as comedic relief –, which helped me get back on the right track. If I was sick, she would take care of cumbersome errands, allowing me to recuperate more quickly; and if I was conducting 24-hour animal experiments, she would provide me with dinner and company at any time of the night. I could go on, but I think it's enough to say that without Yiwen, I wouldn't have made it this far. Thank you, Yiwen, for carrying me through the times when I couldn't walk on my own. You are truly a wonderful person.

This work was supported financially by a Ruth L. Kirschstein F31 (NS079105) Predoctoral Fellowship and Grant R01 (NS040894) from the National Institute of Neurological Disorders and Stroke of the National Institutes of Health.

Chapter 1 : Introduction and Overview

1.1 Introduction

1.1.1 Neural stimulation and recording electrodes

Electrodes are electrical conductors made of a metal or polymer that electrically join metallic and non-metallic conducting bodies. Throughout the 19th and early 20th century, electrodes were primarily used to study electrochemical processes, make batteries, weld, and apply metal coatings to the surface of materials. However, with the advent of the microchip and micro-fabrication techniques in the past 50-60 years, electrodes have emerged as a promising technology for creating prosthetic devices that treat neurological disorders and restore function following injury to the nervous system.

Electrodes can be used either for stimulation or recording. Stimulation electrodes inject charge into the neural tissue, the flow of charge (i.e., current) generates a distribution of electric potentials, and the extracellular potentials elicit a neural response by polarizing the membranes of electrically excitable cells residing in the tissue. Recording electrodes, on the other hand, do not inject charge, but rather monitor the electrical activity within the nervous system by measuring the electric potentials generated by neural elements (e.g., cells and axons) within the tissue.

1.1.2 Examples of neural prosthetic devices

Examples of devices that stimulate the central nervous system (CNS) include brain stimulation for treating motor symptoms in essential tremor and Parkinson's disease [1, 2]; brain stimulation for treating epilepsy [3, 4] and psychiatric disorders [5, 6]; brain stimulation [7] and spinal cord stimulation [8] for treating chronic pain; stimulation of the cochlea and brainstem for restoring hearing [9]; and stimulation of the retina and visual cortex for restoring vision [10]. Further, examples of devices that stimulate the peripheral nervous system (PNS) include vagus nerve stimulation for treating epilepsy [11] and depression [12], occipital nerve stimulation for the treatment of occipital neuralgia [13], sacral nerve stimulation for treating bladder dysfunction [14], and stimulation of lower motor neurons to restore lost motor function [15].

Although less numerous, there are also devices that record activity from the CNS. These include brain-machine interfaces (BMIs) that use recordings of individual neurons in the cortex to control assistive devices that restore motor function in paralyzed individuals [16] and devices that use recordings of local field potentials in cortical tissue to predict and subsequently prevent – through stimulation – the onset of seizures [17].

Figure 1.1 shows examples of electrode designs that are currently used in neural prostheses. Electrodes used to stimulate the brain, spinal cord, and nerves are typically made of a platinum and iridium (PtIr) alloy and have dimensions on the order of millimeters (Figure 1.1d/e). Smooth cylindrical surfaces are used to mitigate tissue damage from implantation; PtIr is used because of its biocompatibility and relatively

large reversible charge injection capacity; but the choice of electrode dimensions is largely based on trial and error. Recording electrodes vary more in their shape, material composition, and size. Electrodes used to record single neurons are sharp tipped; made from biocompatible materials, such as stainless steel, tungsten, or PtIr; and have dimensions on the order of tens of microns (Figure 1.1a/c). Surface electrodes and implanted electrodes used to record from large volumes of tissue are typically planar, have dimensions on the order of millimeters, and are made of silver/silver-chloride and PtIr, respectively.

1.1.3 Improving the performance of stimulation and recording electrodes

Neural prostheses have had substantial clinical success during the past two decades. For example, deep brain stimulation (DBS) of the subthalamic nucleus is more effective than the best medical management in treating the motor symptoms of Parkinson's Disease [18], and spinal cord stimulation (SCS) reduces pain (> 50 %) in individuals with chronic lower leg and back pain [19]. Despite these successes and the success of other emerging therapies, electrode design provides an opportunity to improve these therapies.

The median battery life of implantable stimulators used in DBS and SCS is ~ 3 [20] and ~ 4 [21] years, respectively. Because stimulation is typically administered continuously, multiple replacement surgeries are required in typical patients, and these are costly and obligate the patient to incur repeatedly the risks associated with surgery,

including infection [8, 22, 23] and hardware complications [24]. Therefore, stimulation efficiency is one area that can be improved.

Another area that can be improved is stimulation selectivity. Suboptimal electrode placement is a common mode of failure in DBS [20, 24, 25] and SCS [8]. In some cases, lead deviations preclude some or all potential clinical benefits [20, 23-25], and in others, misplacement generates adverse side-effects from stimulation of non-target regions [8, 20]. Small lead misplacements can in some cases be overcome by altering the amplitude, duration, and frequency of the applied electrical waveform [8, 26]; but larger misplacements require an additional surgery to reposition the lead [25].

In addition to performance, the risks associated with implantation and residence of the electrode(s) must be considered. Implantation of an electrode displaces neural tissue, damaging blood vessels, extracellular matrix, and neurons and glia. The tissue responds to this insult and the chronic presence of electrode by altering the environment around the electrode, potentially leading to further loss of neurons [27]. Because the performance of neural prostheses is dependent on the long-term survival of the targeted neural elements, both stimulation and recording electrodes must be designed to mitigate the tissue response.

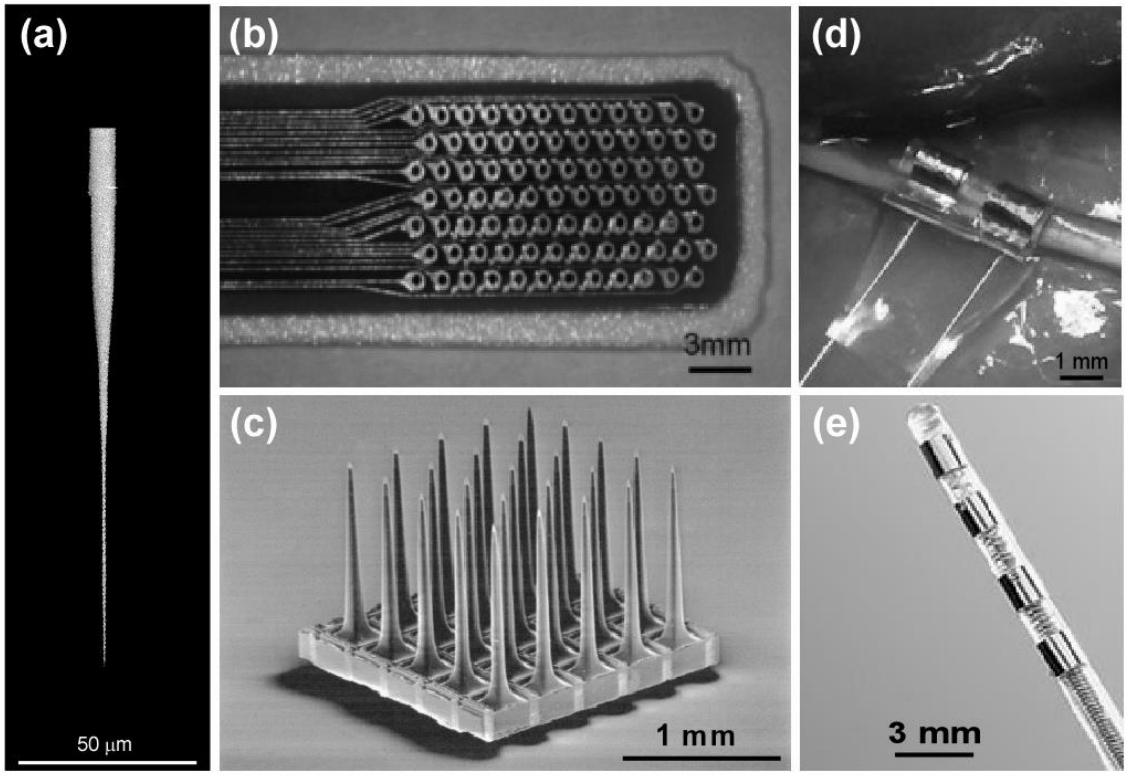

Figure 1.1: Examples of electrodes for neural stimulation and recording.
(a) A carbon fiber-based microelectrode used for recording electrical activity from single neurons (units) in the nervous system (Adapted from Budai, 2010 [28]). (b) An array of platinum electrodes on a flexible polyimide substrate used for retinal stimulation (Adapted from Cicione et al., 2012 [29]). (c) An array of silicon microelectrodes developed at the University of Utah (Adapted from Branner and Normann, 1999 [30]) used for both stimulation and recording. Each electrode is ~ 80 μm wide at its base and tapers to an exposed sharpened tip. (d) A nerve cuff electrode, consisting of two platinum electrodes embedded in an insulating silicone substrate (Adapted from Foldes et al., 2011 [31]), that is used to record the electrical activity of nerves. (e) An array of 4 cylindrical platinum-iridium electrodes embedded within a polyurethane substrate used for Deep Brain Stimulation (Lead Model 3387; Medtronic, Inc., Minneapolis, Minnesota). Similar designs are also used for spinal cord stimulation and cochlear stimulation.

This review describes the fundamental principles of electrode design for neural stimulation and neural recording and how these principles can be used to advance the efficacy of neural prosthetic devices. In the first section, we cover the design of stimulation electrodes and how they can be made more efficient by consuming less

power, more selective by reducing co-activation of non-target elements, and less damaging during stimulation. In the following section, we cover recording electrodes and how they can be designed to be more selective in what neural signals they record, less prone to electrical noise, and less damaging within neural tissue. The review ends with a brief overview of prospective future directions in electrode design. The final version of this review is a chapter in the book, *Implantable Neuroprostheses for Restoring Function* [32].

1.2 Stimulation Electrodes

A stimulation electrode that is effective in activating neural elements satisfies three criterion: it is efficient, selective, and minimizes damage to the neural tissue. Efficient electrodes modulate (i.e., activate, inhibit, or block) the activity of neural elements, such as local neurons or axons, using as little electrical energy as possible. Decreased energy consumption directly extends the lives of non-rechargeable batteries and indirectly extends the lives of rechargeable batteries by decreasing the number of recharge cycles, which in either case, reduces the cost and risks associated with battery replacement surgeries. Selective electrodes are able to target neural elements based on their size, orientation, or type, which reduces the sensitivity of clinical outcomes to (mal) positioning of the electrode. And electrodes that minimize damage to the neural tissue, either from implantation and/or stimulation, will reduce risks associated with stimulation therapies.

1.2.1 Designing more efficient stimulating electrodes

Increasing stimulation efficiency requires decreasing the electrical energy required to modulate the activity of target neural elements. The instantaneous electrical power (P) transferred to the neural tissue is the product of the applied voltage (V) and applied current (I),

$$P = IV \tag{1.1}$$

Electrical energy (E) is the time integral of P,

$$E = \int P dt \tag{1.2}$$

Therefore, E is reduced by decreasing the applied voltage and/or applied current that is used to modulate the activity of the target neural elements. Understanding how this can be accomplished, however, first requires understanding the electrical characteristics of the electrode, tissue, and target neural elements.

1.2.1.1 Circuit representations of the electrode, tissue, and neural elements

The electrode and connecting wires in current electrical stimulation devices are made of metal. Metals conduct electrons, whereas biological tissues conduct ions – such as sodium, potassium and chloride – so an interface exists between the electrode and

tissue, known as the electrode-tissue interface (ETI), where charge changes form as it is transferred between the electrode and tissue. Charge transfer can occur in one of three ways: it can be non-Faradaic (capacitive/indirect), where equal and opposite charges in the electrode and tissue are redistributed via Columbic forces; Faradaic (or direct), where electrons are transferred between the electrode and tissue via electrochemical (i.e., oxidation and reduction) reactions; or a combination of both direct and indirect charge transfer, such as the electrochemical generation of (specific and non-specific) adsorbable species (Figure 1.2a).

Given the above, we can build what is known as the Timmer equivalent circuit representation of an electrode in tissue (Figure 1.2b). Electrons flow freely through the electrode and connecting wires, so they are modeled as a single conductor with an ohmic resistance (R_E). Indirect charge transfer at the ETI is modeled with two parallel-plate capacitors: a double-layer capacitor (C_{dl}) that accounts for charge redistribution and a pseudo capacitor (C_{ps}) in series with a charge transfer resistance (R_{ps}) that accounts for ion adsorption and the electrochemical reactions that give rise to the adsorbed species, respectively. Direct charge transfer is modeled using a series combination of a Faradaic resistance (R_f) that accounts for the transfer of electrons in electrochemical reactions, a Warburg element (Z_W) that accounts for mass transfer (diffusion) limitation in these reactions, and a battery (E^0) that accounts for the electromotive force at equilibrium when no current is applied. Beyond the electrode and ETI, ions flow freely, so the tissue is also modeled as a single conductor with an ohmic resistance known as the access resistance (R_a).

In some electrical stimulation therapies, such as DBS and SCS, charge transfer occurs in a short enough time scale that both diffusion limitations and adsorption are negligible, and the electrical loads presented by the stimulation electrode and connecting wires are small compared to the loads presented by the ETI and tissue. In these cases, R_E, Z_W, C_{ps}, and R_{ps} can be ignored, yielding what is known as the three-element Randles equivalent circuit (Figure 1.2c).

The neural elements targeted in electrical stimulation therapies can also be modeled by a distributed network of electrical circuit elements. Neural elements include local neurons, consisting of a cell body (soma), dendrites, axon, and axon terminal; and the axons of distal neurons that pass by or terminate in the target brain region. Axons and dendrites are much longer than they are wide and azimuthally symmetric about their longitudinal axis, so they are typically modeled as a one dimensional cable of cylindrical membrane compartments (Figure 1.2d). The soma, although spherical, can also be approximated as a series of cylindrical compartments, and the flow of charge through the neuron can be described with a partial differential equation known as the Cable Equation:

$$C_m \frac{dV_{m,n}}{dt} + \frac{(V_{m,n} - V_r)}{R_m} - \frac{\delta^2 V_{m,n}}{R_i} = \frac{\delta^2 \Phi_{m,n}}{R_i} \tag{1.3}$$

R_m and C_m are the membrane resistance and membrane capacitance, respectively, V_m is the membrane potential, V_r is the resting membrane potential, R_i is the intracellular/axoplasmic resistance between compartments, Φ_e is the external potential on

the surface of the membrane, δ is the centered difference operator, and n denotes the index of the compartment.

The Randles circuit and Cable Equation are used in the following sections to determine how one can alter the design of the electrode so that the energy transferred during stimulation is reduced.

1.2.1.2 Decreasing the electrode impedance

The efficiency of a stimulation electrode can be increased by decreasing the electrical load, or impedance, driven by the stimulator (Z_e). Reducing Z_e increases the amount of current injected into the tissue per applied volt, which translates into less voltage being required to supply the critical amount of current (i.e., the threshold current) necessary to generate a distribution of potentials whose magnitude is large enough to evoke a neural response. Recall, Z_e includes the impedances of the connecting wires, electrode, ETI, and tissue (Figure 1.2b); and for typical electrical stimulation therapies, Z_e is dominated by the impedances of the ETI and tissue – namely C_{dl}, R_f, and R_a (Figure 1.2c). Since resistors have an impedance that is proportional to their resistance, and since capacitors have an impedance that is inversely proportional to their capacitance, Z_e can be decreased by increasing C_{dl}, decreasing R_f, and/or decreasing R_a.

C_{dl} can be modeled as a parallel-plate capacitor with a capacitance, $C = \varepsilon_0 \varepsilon_r A_e/d$, where ε_0 is the vacuum permittivity, ε_r is the relative permittivity of the interface, A_e is the 3D (or microscopic) area of overlap between the electrode and tissue, and d is the

thickness of the interface. With this, we see that one way to increase C_{dl} is to roughen the electrode surface at the microscopic level, markedly increasing A_e, while leaving the 2D (geometric) surface area (A) unchanged. – Note, A_e is distinguished from A because the former describes changes in the electrode texture, while the latter describes changes in the electrode dimensions. For example, electrical deposition of dissolved platinum (Pt) onto Pt and titanium (Ti) can increase A_e up to 280 and 410 times, respectively, and vapor deposition of titanium nitride (TiN) onto Pt and Ti can increase A_e up to 1100 and 580 times, respectively [33].

C_{dl} can also be increased by coating the surface of the electrode with a thin dielectric material. Coating the electrode with a dielectric increases the ε_r of the ETI, and making the dielectric as thin as possible minimizes the accompanying increase in d. Since the dielectric prevents direct charge transfer, electrodes that use this approach are known as capacitive electrodes. Tantalum (Ta) and TiN electrodes are two types of capacitive electrodes that have been studied for neural stimulation. At positive (i.e., anodic) stimulation voltages, oxidation of Ta produces Ta pentoxide (TaO_5) with an ε_r of 25, and oxidation of TiN produces the rutile form of Ti dioxide (TiO_2) with an ε_r of 100 [34]. Compared to TaO_5, TiO_2 is more porous and therefore more susceptible to undesirable irreversible reduction-oxidation (redox) reactions, such as the hydrolysis of water [34]. However, compared to TiN electrodes, Ta electrodes have a smaller reversible charge injection capacity, are less amenable to surface roughening, and require relatively high bias voltages (> 4V) between stimulation pulses to maintain the formation of TaO_5. Therefore, TiN electrodes are more extensively used for electrical stimulation [35].

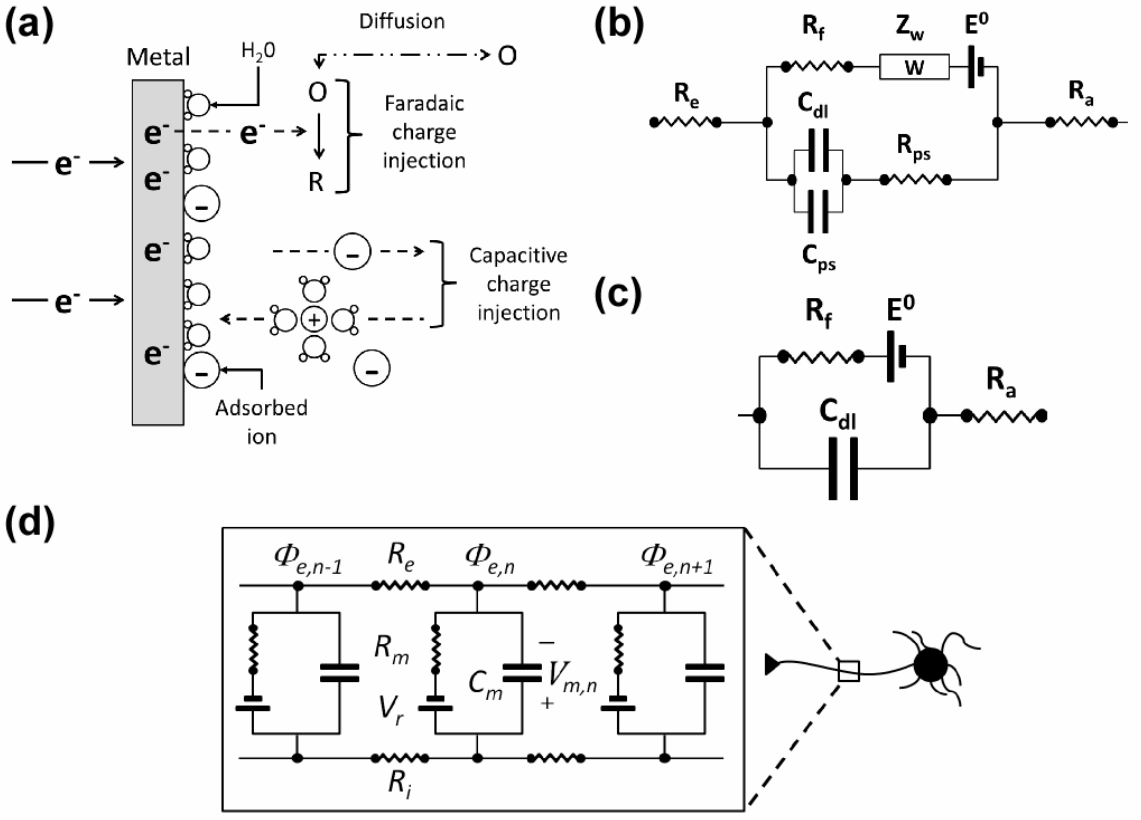

Figure 1.2: Circuit representations of an electrode in tissue and a neural element.
(a) The electrode-tissue interface (ETI) and possible modes of charge injection, including Faradaic charge injection, non-Faradaic/capacitive charge injection, and charge injection via the generation and (specific and non-specific) adsorption of ions. (b) The Timmer equivalent circuit representation of the electrode, ETI, and tissue. R_e is the resistance of the metal electrode, R_f is the Faradaic resistance, Z_w is the Warburg element, C_{dl} is the double-layer capacitance, C_{ps} and R_{ps} are the pseudo capacitance and resistance, respectively, R_a is the access resistance, and E^0 is the standard electrode potential. (c) The Randles equivalent circuit that results when R_e, Z_w, C_{ps}, and R_{ps} are ignored from (b). (d) A lumped circuit representation of a patch of membrane of a neuron. R_m and C_m are the membrane resistance and membrane capacitance, respectively; V_m is the membrane potential; V_r is the resting membrane potential; R_i and R_e are the intracellular/axoplasmic and extracellular resistances, respectively; Φ_e is the external potential; and n denotes the index of the compartment.

The dependence of R_f on the geometry and material properties of the electrode is not obvious. The relationship between the potential drop across R_f, often referred to as the overpotential (η), and the Faradaic current (I_η) through the ETI is nonlinear and generally cannot be expressed in a closed-form solution. Yet, one can still achieve a qualitative understanding of how to alter R_f by examining basic principles. Consider a first-order redox reaction. According to the law of mass action, the current I_η that flows from such a reaction can be expressed as

$$I_\eta = nFA_e k_x C_x \tag{1.4}$$

, where n is the number of electrons transferred, F is the Faraday constant, k_x is the rate constant of the reaction (in s^{-1}), and C_x is the surface concentration of the reacting species (in mol/m^2). For simple reactions, where the external distribution has a negligible effect on the reacting species, collision theory says that k_x has an exponential dependence on η. Implicit differentiation of Equation 1.4 with η as the dependent variable yields an expression for $d\eta/dI_\eta = R_f$ that is inversely proportional to A_e. Therefore, surface roughening techniques that increase A_e are also able to decrease Z_e by decreasing R_f.

Another way to decrease R_f is to apply what is known as a Faradaic electric coating. Fardaic coatings work by introducing a redox couple with a relatively large kinetic facility so that a greater amount of I_η can be generated per change in η. One of the most widely used Faradaic coatings for electrical stimulation is a hydrated film of iridium

(Ir) oxide. Ir oxide can be rapidly and reversibly oxidized or reduced between two oxidative states, Ir^{3+} and Ir^{4+}. Because the reactants remain bound to the electrode surface, Faradaic coatings impart what is referred to as pseudo-capacitance. Pseudo-capacitance is advantageous, because like capacitance, it allows reversible charge injection, which minimizes the probability of damage to the electrode and tissue. For example, Pt electrodes can reversibly inject up to 0.3 mC/cm^2, whereas PtIr electrodes with an Ir oxide coating have the ability to inject up to ± 1 mC/cm^2 and ± 2 mC/cm^2 for cathodic and anodic stimulation, respectively [35].

We discuss the effects of R_a by considering a spherical electrode with a radius of r_a that resides in an infinite conducting medium whose resistivity, ρ, is homogeneous (i.e., the same at all locations) and isotropic (i.e., the same in all directions). In this case, it can be shown that $R_a = \rho/4\pi r_a$. Of course, different geometries would yield different expressions for R_a, but this equation illustrates that R_a is inversely related to the macroscopic dimensions of the electrode. Thus, one way to reduce R_a is by increasing the 2D geometric surface area, A, of an electrode.

In the above example, the current density ($\vec{J}$) on the surface of a spherical electrode is uniform, but the same is not true for electrodes that are inlaid in an insulating substrate (Figure 1.1b, d, and e). In these cases, $\vec{J}$ is largest on the edges (or perimeter) of the electrode where the metal and insulator meet, so R_a can also be reduced by increasing the electrode perimeter [36, 37]. These "edge effects", however, are not as pronounced as the effect of increasing A [38]. For example, quantitative measurements have revealed that doubling the perimeter of an array of cylindrical electrodes decreased

its impedance by ~ 17 %, whereas doubling the area (or coverage) of the cylindrical electrode array decreased its impedance by ~ 30 % [36].

1.2.1.3 Altering the driving force for neural activation

Reducing Z_e is not the only means to increase efficiency. Recall the cable equation (Equation 1.3), whose right-hand side (or forcing function) represents the source driving polarization of the neural membrane during electrical stimulation [39]. Since the source term is proportional to the centered second spatial difference of the extracellular potentials ($\delta^2\Phi$), stimulation efficiency can also be increased or decreased by altering $\delta^2\Phi$. This is known as field shaping.

Consider a point source electrode in an infinite conducting medium with homogeneous and isotropic ρ. The potentials generated by the point source are described by:

$$\Phi(r) = \frac{\rho I_e}{4\pi r} \tag{1.5}$$

, where I_e is the source current, and r is the radial distance from the source. Equation 1.5 is spherically symmetric, so $\delta^2\Phi$ evaluated between any 3 connective points in space (e.g., between 3 adjacent nodes of Ranvier of an axon) is independent of orientation, as long as those 3 points have the same corresponding r_e (Figure 1.3). Therefore, $\delta^2\Phi$ of

electrodes that resemble a point-source, such as spherical electrodes and microelectrodes with an exposed tip, will depend on the applied current and distance but not direction or orientation.

It follows that if an electrode is not spherical, then it will produce an asymmetric potential distribution whose corresponding $\delta^2\Phi$ depends on direction. Consider a finite line source in an infinite medium with a homogeneous and isotropic ρ. The potentials generated by a line source in this case are described by:

$$\Phi(x,y,z) = \frac{\rho\lambda}{4\pi}\ln\left\{\frac{\sqrt{(z-L/2)^2+(x-x_e)^2+(y-y_e)^2}+(z-L/2)}{\sqrt{(z+L/2)^2+(x-x_e)^2+(y-y_e)^2}-(z+L/2)}\right\} \quad (1.6)$$

where λ is the linear current density (in A/m), L is the length of line source, and x_e and y_e are the Cartesian coordinates of the midpoint of the line source with respect to the origin. Perpendicular to the long axis of the line source, the potentials have a shape that is similar to that of a point source, but parallel to its long axis, the potentials are flattened, leading to a marked reduction in $\delta^2\Phi$ (Figure 1.3). By comparing Equation 1.5 when I_e = -1 mA to Equation 1.6 when λ = -1/3 mA/mm and L = 6 mm, we see that the line source, despite applying twice as much current, generates a $\delta^2\Phi$ that is comparable to or less than the $\delta^2\Phi$ of the point source, depending on the orientation (Figure 1.3). Therefore, changes in efficiency that result from field shaping can be similar to or greater than changes in efficiency that result from altering Z_e.

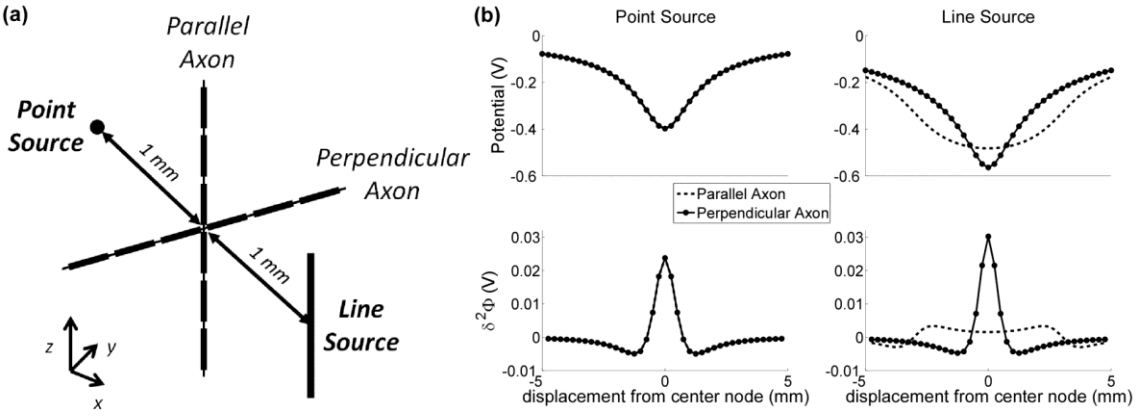

Figure 1.3: The effect of electrode geometry on the source driving neural polarization.
(a) A point source (PS) and a line source (LS) extending in the z-direction are used separately to stimulate two axons in an infinite conducting medium with a homogeneous and isotropic conductivity of 0.2 S/m, equal to that of grey matter [40]. The axons are displaced 1 mm from the PS and 1 mm from the midpoint of the LS, and in both cases, the axons are orientated parallel and perpendicular to the z-axis. (b) The potentials (top) and the centered second difference of the potentials ($\delta^2\Phi$, bottom) generated at the nodes of the two axons when the PS (left) and LS (right) inject 1 mA and 2 mA, respectively.

Field shaping can also be achieved by steering current between two or more electrodes in a multipolar configuration. The most basic multipolar configuration is a bipole, which consists of a source (anode) and a sink (cathode). Let us return to our previous example of a point source in an infinite conducting medium with a homogeneous and isotropic ρ. If we extend this example by adding a point sink, then the potentials generated by the bipolar pair can be expressed as

$$\Phi = \frac{\rho I_e}{4\pi}\left(\frac{1}{r_+} - \frac{1}{r_-}\right) \tag{1.7}$$

, where r_+ and r_- are the distances to the source and the sink, respectively. Equation 1.7 changes sign: the potentials are positive when $r_+ < r_-$, zero when $r_+ = r_-$, and negative when $r_+ > r_-$. Therefore, with a bipole, the magnitude of the difference in potentials between two points, $|\Delta\Phi_n| = |\Phi_n - \Phi_{n+1}|$, is bounded between 0 and $|\Phi_n| + |\Phi_{n+1}|$. To compare, a monopole (Equation 1.5) has a $|\Delta\Phi_n|$ that is bounded between 0 and the maximum of $|\Phi_n|$ and $|\Phi_{n+1}|$, so the $\Delta\Phi$ of a bipole can be greater than the $\Delta\Phi$ of a monopole.

The goal, however, is not to increase $\Delta\Phi_n$ but $\delta^2\Phi_n$. Expanding $\delta^2\Phi_n$ in terms of its backward difference $(\Phi_{n-1} - \Phi_n)$ and its forward difference $(\Phi_{n+1} - \Phi_n)$ yields the following expression: $\delta^2\Phi_n = (\Phi_{n-1} - \Phi_n) - (\Phi_{n+1} - \Phi_n)$. In this form, we see that $\delta^2\Phi_n$ can be increased by using not one but two bipoles, opposite in orientation, that share a common sink. This is referred to as a tripole (Figure 1.4a). The first and second bipole increase the magnitude of $(\Phi_{n-1} - \Phi_n)$ and $(\Phi_{n+1} - \Phi_n)$, respectively, and because the bipoles are in opposite orientations, the two differences are of opposite sign. As a result, a tripole generates a $\delta^2\Phi_n$ that can be as large as $|\Phi_{n-1} - \Phi_n| + |\Phi_{n+1} - \Phi_n|$, which is greater than the maximum possible $\delta^2\Phi_n$ generated by a monopole applying the same amount of current (Figure 1.4b).

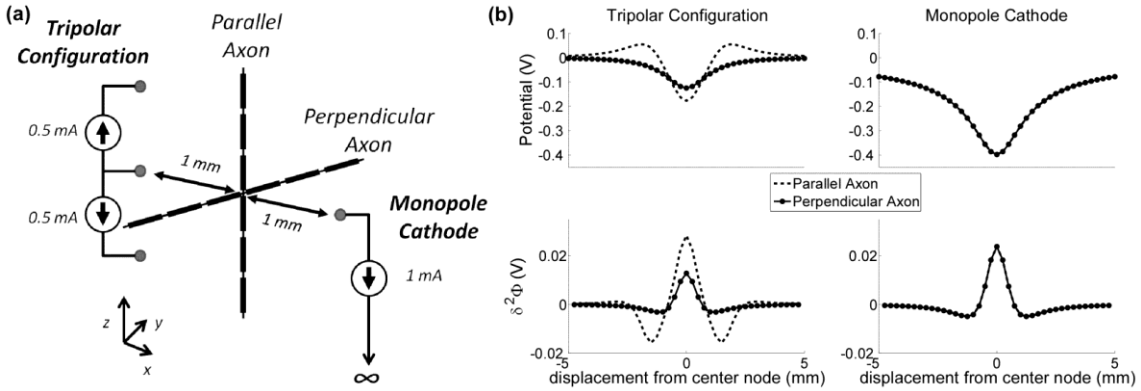

Figure 1.4: Current steering and its effects on the source driving neural polarization.
(a) A point source (PS) and a tripole, which consists of two oppositely oriented bipoles along the z-axis that share a common sink, are used individually to stimulate two axons placed in an infinite conducting medium with a homogeneous and isotropic conductivity of 0.2 S/m, equal to that of grey matter (Gabriel et al., 2009). The axons are displaced 1 mm from the PS and 1 mm from the sink of the tripole. In both cases, the axons are oriented parallel and perpendicular to the z-axis. (b) The potentials (top) and the centered second difference of the potentials ($\delta^2\Phi$, bottom) generated at the nodes of the two axons when the tripole (left) and PS (right) release 1 mA of current.

1.2.2 Designing more selective stimulation electrodes

Efficacy also requires that an electrode be able to activate selectively specific elements of the nervous system. In SCS, it is hypothesized that the therapeutic effect is achieved when axons in the dorsal column (DC) of the spinal cord are activated without co-activation of nearby afferents in the dorsal roots (DR) [41, 42]. In retinal prostheses, the quality of visual perception is thought to depend on the ability to activate nearby retinal ganglion cells (RGCs) without co-activating passing axons of distal RGCs [43, 44]. And DBS clinical studies have shown that lead deviations as small as 2-3 mm can preclude some or all clinical benefits [20, 23-25], and in some cases generate adverse side-effects [20]. Increased selectivity is achieved by activating neural elements based on their orientation, location, size, and/or type.

1.2.2.1 Activation based on orientation

Selective activation of neural elements based on their orientation is achieved by shaping the potential distribution so that $\delta^2\Phi$ in one orientation is larger than $\delta^2\Phi$ in other non-target orientations. One way to accomplish this is by altering electrode geometry. Consider a cylindrical electrode whose axis lies in the z direction. Elongation of the cylinder by increasing its height causes the current density ($\vec{J}$) to become more uniform along its axis. If we assume the electric field ($\vec{E}$) is both static ($\vec{E} = -\nabla\Phi$) and linear ($\vec{J} \cdot \rho = \vec{E}$), which is a reasonable approximation for many electrical stimulation therapies, then as $\vec{J}$ in the z direction becomes more uniform, $\nabla \cdot \vec{J}$ in the z direction approaches 0. This means $\delta^2\Phi$ reduced along the axis of the elongated electrode (Figure 1.3), lowering the source driving polarization of parallel elements so that perpendicular elements are activated first.

Orientation-dependent activation of neural elements can also be achieved using a multipolar configuration, such as a tripole. Recall from section 1.2.1.3, that a tripole consisting of two bipoles in opposite orientations increases $\delta^2\Phi$. Parallel to the displacement vector ($\vec{d}$) that points from the sink to the source, the potentials change sign, but perpendicular to $\vec{d}$, the sign of the potentials does not change. This means the ability of a tripole to alter $\delta^2\Phi$ is maximal and minimal in directions that are parallel and perpendicular to $\vec{d}$, respectively (see Figure 1.4). Therefore, tripoles – and potentially

other multipolar configurations – can activate elements parallel to the electrode at lower stimulation thresholds than elements perpendicular to the electrodes.

Although the performance of tripoles and elongated electrodes has not been extensively tested in a clinical setting, a number of modeling studies have looked at potential application of these geometries. In SCS, tripoles are predicted to perform better than bipoles and monopoles in activating the therapeutic targets, the DC fibers, over the undesirable targets, the DR fibers [45-47]; and in retinal stimulation therapies, elongated arrays of electrodes are expected to have a high degree of selectivity in activating local RGCs over the axons of distal RGCs that pass parallel to the array [43].

1.2.2.2 Activation based on spatial location

The potentials generated by an electrode decrease in magnitude with increasing distance. In general, $\delta^2\Phi$ declines as the magnitude of the potentials declines, so the ability of an electrode to activate elements near its surface selectivity depends on how rapidly the potentials decay. In some cases, for example, when targeting individual fascicles within a nerve, the closest elements can be selectively activated by using the contact(s) closest to the target population [48, 49]. However, in other cases, such as brain stimulation, where the target and non-target population can be in close proximity, other techniques are required.

Multipolar configurations with relatively small inter-electrode spacings can be used to increase the spatial selectivity of an electrode. For example, when the distance to a bipole is much greater than the distance between the source and sink, the potentials

decline proportional to ~ $1/r^2$. To compare, the potentials of a point source decay proportional to 1/r (Equation 1.5), so electrodes pairs that resemble a bipole have better spatial selectivity than a single electrode. Higher order multipoles with small inter-electrode spacings, such as a tripole, have potentials that decay ~ $1/r^3$, so as a general principle, the spatial selectivity of a multipole increases with its order.

Other than SCS, there are very few applications that currently use multipolar configurations. Yet, this may change in the future, as multipolar configurations are being considered for better targeting in DBS, especially in cases where the electrode is sub-optimally placed [50].

1.2.2.3 Activation based on size

In the PNS, the natural recruitment order of motor units (defined as a motor neuron and its innervated muscle fibers) is from smallest to largest. However, in external electrical stimulation, $\delta^2\Phi$ increases with increasing fiber diameter (D), and the recruitment order of motor axons is reversed. The largest motor axons are fast glycolytic, type II fibers, which generate large forces and fatigue easily, so in therapies that aim to restore lost motor function, such as functional electrical stimulation (FES), evoking dexterous movements and sustained activation without fatigue is a challenge [15].

One design for restoring the natural recruitment order is a tripolar electrode in an anode-cathode-anode configuration. A tripole generates a $\delta^2\Phi$ that is maximally positive and thereby depolarizing closest to the cathode (Figure 1.4b), so when a motor axon is

activated, the action potential (AP) initiates in the NoR most proximal to the cathode. At the same time, the flanking anodes (Figure 1.4b) hyperpolarize distal NoRs, and at large enough stimulation amplitudes, the AP can be blocked, starting with the largest D axons. Blocking, however, requires a trapezoidal waveform with a relatively long duration on the order of 1 ms: the leading edge and plateau phases must last long enough to block the propagating AP (~ 350 μs), and the trailing edge phase must decline over a long enough period (~ 600 μs) that anodic block excitation does not occur upon termination of the blocking pulse [51, 52].

Another design for restoring the natural recruitment order is a longitudinal array of five or more electrodes in an alternating source-sink configuration [53, 54]. An alternating array produces a sinusoidal distribution of potentials. Activation of myelinated motor axons depends on $\delta^2\Phi$ between the nodes of the Ranvier (NoR), and the intermodal length (INL) between nodes is linearly proportional to D [55]. Thus, only axons with INL > the center-to-center inter-electrode spacing of the electrode will spatially alias the source term, resulting in a reduced $\delta^2\Phi$ for large D axons. This technique works independent of the pulse width of stimulation, so unlike a tripolar electrode, it can be used for relatively small pulse widths of < 500 μs.

1.2.2.4 Activation of specific neural elements

There is growing evidence in brain stimulation therapies showing that the therapeutic targets are local afferent fibers. High frequency DBS of cerebellar afferents in the Vim is predicted to mask tremor-associated burst activity in essential tremor [56];

high frequency stimulation of cortical afferents in the subthalamic nucleus (STN) reduces parkinsonian symptoms in rats [57]; and tonic stimulation of afferents in the nucleus accumbens reduces depressive symptoms in mice [58]. For that reason, neural prostheses can be made more effective by designing electrodes that selectively activate terminating axons (TA) over other neural elements, such as an axon of passage (AOP) or local neuron (LN).

The source driving membrane polarization at the terminal of TA is not proportional to $\delta^2\Phi$ but rather proportional to $\Delta\Phi$, so electrodes that can markedly increase $\Delta\Phi$ have the ability to selectively target TA. The simplest example of this is a bipole (Figure 1.5a). A bipole has the ability to increase $\Delta\Phi$ (section 1.2.1.3), and the ability to increase $\Delta\Phi$ is maximal in directions that are parallel to $\vec{d}$ (section 1.2.2.1). Hence, a bipolar electrode activates TAs at lower stimulation thresholds than passing axons because it generates a $\Delta\Phi$ parallel to $\vec{d}$ that is greater than the maximum $\delta^2\Phi$ in directions that are parallel and perpendicular to $\vec{d}$ (Figure 1.5b).

Selective activation of TAs over AOPs and LNs is the objective when the electrode is downstream of the target neuron population. However, in cases where the electrode is implanted upstream, where the axons of the therapeutic targets originate, then the objective shifts to activation of LN at lower thresholds than AOP and/or TA. Techniques for selectively activating LNs fall outside the scope of electrode design, but a discussion of these techniques can be found in [44] and [59, 60].

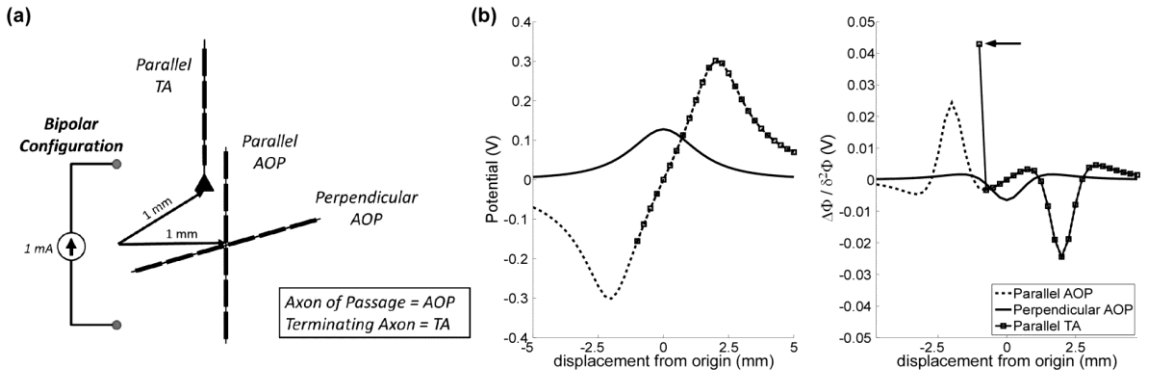

Figure 1.5: Selective activation of terminating axons at lower thresholds than axons of passage.
(a) Two point source electrodes in a bipolar configuration are used to stimulate a parallel terminating axon (TA), a parallel axon of passage (AOP), and a perpendicular AOP in an infinite medium of grey matter (0.2 S/m) (Gabriel et al., 2009). The neural elements are positioned such that the center nodes of the parallel and perpendicular AOP and the terminal of the TA are all 1 mm from the center of the bipolar electrode pair. (b) The potentials (left) and the centered second difference of the potentials ($\delta^2\Phi$, right) at the nodes of the neural elements being stimulated. The arrow indicates the first difference of the potentials ($\Delta\Phi$) at the terminal of the TA.

1.2.3 Designing non-damaging stimulation electrodes

Regardless of how efficient and selective an electrode design is, to be effective it must also minimize damage to the nervous tissue. Damage to the neural tissue can occur passively, due to implantation and residence of the electrode within the tissue, or dynamically, as a result of stimulation. Therefore, designing electrodes that minimize tissue damage requires an understanding of the "passive" and "dynamic" tissue responses.

The passive tissue response includes the inflammatory and immune response to injuries during implantation and the presence of the electrode, as well as cellular responses to mechanical stresses that arise from relative movement of the electrode and tissue. Since this response pertains to both stimulation and recording electrodes, it will be

covered in Appendix A. The dynamic response includes changes or damage to the tissue that can arise from heat generation, electrochemical reactions that occur during charge injection, and/or non-physiological activation of neurons; and because it is a product of passing current through the electrode(s), it pertains only to stimulation electrodes.

In section 1.2.3, we cover the origins of the dynamic tissue response and how stimulation electrodes can be designed to mitigate this response. Polarization refers to any combination of stimulation parameters (amplitude, pulse width, and frequency), but our focus in on the range of parameters typically used for electrical stimulation. This includes amplitudes between 0-10.5 V and 0-6 mA for voltage-regulated stimulation and current-regulated stimulation, respectively, pulse widths between 60-1000 μs, and frequencies between 1-5000 Hz (Table 1.1).

Table 1.1: Stimulation Parameters Approved for Electrical Stimulation Therapies

Therapy		Amplitudes** (V/mA)	Pulse Widths (μs)	Frequencies (Hz)
Central Nervous System	Deep Brain Stimulation [26]	0-10.5 V (1-5 V)*	60-450 (60-210)*	2-185 (130-185)*
	Spinal Cord Stimulation [61]	0-10.5 V	60-1000 (80-500)*	2-1200 (17-750)*
Peripheral Nervous System	Vagal Nerve Stimulation	0-3.5 mA	130-1000	1-30
	Gastric Nerve Stimulation	0.5 mA	330	14
	Vagus Nerve Block	1-6 mA	100	5000

* Stimulation parameters typically used by patients.
** Amplitudes in volts (V) and milliamps (mA) represent voltage-regulated stimulation and current-regulated stimulation, respectively.

1.2.3.1 Mitigating heat generation

The electrode is a source of heat energy when passing current. In retinal prostheses, heat generation is predicted to increase temperatures 0.8 °C at the surface of the implant and 0.16-0.26 °C in the surrounding vitreous cavity [62], and in DBS, temperatures are predicted to increase as much as 1 °C in the surrounding tissue at high stimulation settings (10 V, 185 Hz, 210 μs) [63, 64]. Animal studies looking at the effects of temperature on brain tissue show that some neuronal death (~ 6 %) occurs after 60 min at 40.5 °C and blood-brain barrier breakdown occurs after 60 min at 42 °C [65]. The American Association of Medical Instrumentation recommends that medical implants do not exceed temperature increases of 1-2 °C, but there is still a paucity of data on the long-term effects of small temperature increases on brain tissue.

Heat generation during electrical stimulation can be mitigated by distributing the thermal load. One approach is to increase the dimensions of the electrode. A larger electrode has a smaller power density (watts / unit area), which is proportional to the rate of change in the temperature [66], so temperature increases are reduced, allowing heat loss due to perfusion to better compensate for the heat generated by the electrode. Increasing the electrode dimensions is advantageous because it can be more rapidly translated into clinical use, as it uses existing materials, but disadvantageous because larger electrodes may damage more tissue upon implantation.

A second approach is to increase the thermal conductivity (W/°C) of the insulating substrate holding the electrode(s). Modifying the insulator with a material that

has a relatively high thermal conductivity and low electrical conductivity (e.g., diamond, diamond-like carbon, and alumina ceramics) distributes the thermal load over the electrode shaft, decreasing the power density. For example, the thermal conductivity of the polyurethane insulator used in DBS and SCS (0.026 W/°C) is three orders of magnitude less than the thermal conductivity of the PtIr stimulation electrodes (31 W/°C) [63]. Increasing the thermal conductivity of the insulator 3-5 orders of magnitude reduces temperatures increases by approximately 35 and 72 %, respectively [63].

1.2.3.2 Non-damaging charge transfer

Charge transfer at the ETI can lead to irreversible redox reactions that damage the electrode and tissue. Undesirable reactions include the reduction (electrolysis) of water and the oxidation (corrosion) and reduction (dissolution) of the metal electrode. It is for this reason that electrodes designs with large reversible charge storage capacities (RCSC) are desirable.

Electrodes that transfer charge in a capacitive manner naturally have a large RCSC. For example, TiN electrodes (section 7.2.1.2) have a maximum RCSC of ~ 1 mC/cm^2, which is 1-2 orders of magnitude greater than the RCSC of noble metals, such as Pt and PtIr [35]. Achieving such a large RCSC, however, requires a relatively high bias voltage (> 4V) in the period between stimulation pulses, which reduces stimulation efficiency.

An alternative solution to a capacitor electrode is an electrode that has pseudo-capacitance – that is, the ability to inject charge reversibly via redox reactions. Coated PtIr electrodes (section 7.2.1.2) can inject up to 1 mC/cm^2 and 2 mC/cm^2 for cathodic stimulation and anodic stimulation, respectively [67], so noble metals with Faradaic coatings are strong candidates for safe charge transfer.

In addition to irreversible redox reactions, tissue damage may also arise from stimulation-induced neural excitation, as persistent activation is an unnatural state for most neurons. One proposed mechanism for stimulation-induced neural injury is exitotoxicity. In exitotoxicity, excessive release of the neurotransmitter glutamate leads to persistent activation of ionotropic NMDA receptors on postsynaptic neurons, calcium ions (Ca^{2+}) flow into the cell, and the resultant pathologic levels of Ca^{2+} triggers the death of the neuron – via apoptosis. Because exitotoxicity is only one of a few proposed mechanisms for stimulation-induced neural injury, it still remains unclear what exactly leads to neuron injury. Regardless, the degree of injury is related to the charge density and the charge per phase of stimulation pulse [68], and models have been proposed to help delineate what levels of these factors are damaging to the neural tissue [69]. Thus, the electrode geometry and stimulation parameters should be chosen such that the charge density and charge per phase are non-damaging.

1.3 Outline of Chapters

Chapter 1 described the fundamental principles of electrode design for neural stimulation and how these principles could be used to advance the efficacy of neural

prostheses. This overview is the first section of a book chapter on electrode design for stimulation and recording. The second section covers recording electrodes and how they can be more discriminating in what they record, less prone to electrical noise, and less damaging to the neural tissue. The latter section goes beyond the scope of this work but pertains to electrode design, in general, so it is included in Appendix A.

Chapter 2 analyzes the effects of common simplifications on computational models of DBS. A spatiotemporal model of an implanted DBS electrode in brain tissue was used to address how the choice of discretization parameters, representation of the inactive electrodes and electrode shaft, and representation of the electrode-tissue interface (ETI) affected the calculation of the electric potentials and subsequent stimulation thresholds. The details of the methodology are found in Appendix B. This work delineated the level of detail required in computational models of DBS to make accurate calculations of the neural response to DBS.

Chapter 3 presents an analysis on which geometrical parameter, perimeter or area, has a greater impact on stimulation efficiency. Eight electrode designs with different areas and perimeter were analyzed. Finite element method (FEM) models of the electrode designs were developed to quantify the effect of electrode geometry on the electrical properties of the electrode, and subsequently, to assess the impact of these changes on the electrical potentials and stimulation thresholds. In addition, the electrical properties and stimulation efficiency of our electrode designs were measured in vitro and in vivo, respectively.

Chapter 4 extends upon the work in Chapters 3 by coupling a computational model of a three-electrode array in brain with a genetic algorithm and using the model to search for electrode designs that increase the efficiency and selectivity of DBS. The outcome from Chapters 3 and 4 is a greater understanding of the features of electrode design (i.e., geometry and polarity) that are the most important for the next generation of DBS electrodes.

Chapter 5 presents a study comparing activation of neural elements during intradural and extradural spinal cord stimulation (SCS). Computational models of SCS were developed based on the spinal geometries of five patients receiving SCS for the treatment of chronic low back pain. The models were used to quantify the impact of electrode design on the efficiency and selectivity of SCS, and how the performance of the electrode depends on its placement. Part of this study focuses on the clinical findings and the clinical implications of the model predictions, which does not cover electrode design, and therefore is placed in Appendix C. The outcome of this work is a quantitative understanding of how intradural electrode placement can potentially increase the selectivity and efficiency of SCS, which, in turn, provides predictions that can be tested in future clinical studies assessing the potential therapeutic benefits of intradural SCS.

Chapter 6 summarizes the main findings of this work and discusses the future directions in electrode design for electrical stimulation.

Chapter 2 : A Computational Model of Deep Brain Stimulation –Influences of Interpolation Error and the Electrode-Tissue Interface on Solution Accuracy

2.1 Introduction

Deep brain stimulation (DBS) is an established therapy for treating neurological disorders, where high frequency (typically 100-200 Hz) electrical pulses are delivered to specific regions of the brain. DBS is effective in treating Parkinson's disease and essential tremor [1, 2], and may be a promising therapy for epilepsy and psychiatric disorders [5, 6]. However, the mechanisms by which DBS relieves symptoms are still unknown.

Determining the mechanisms of DBS requires a quantitative understanding of how altering DBS parameters affects the response of neural elements within the central nervous system (e.g., excitation [70], inhibition [70], blocking [71]). Studying the effects of DBS on neural activation using experiments alone is impractical because the parameter space of DBS is vast. For example, tens of thousands of combinations of pulsewidth, frequency, and amplitude are available in implanted pulse generators, such as the Medtronic Soletra Model 7426 (Medtronic Inc, Minneapolis, MN); and there are multiple electrode configurations and anatomical targets [26]. Further, there is a lack of understanding of what neural elements are being affected and whether these effects are local or distributed throughout the targeted neural network. Thus, computational models are important tools to study DBS.

To be useful, computational models must have sufficient detail to predict accurately the electric fields produced by DBS. The most detailed computational models of DBS are patient-specific finite element method (FEM) models: the geometry of brain structures is defined by individual brain images, and the conductivities of each brain region are determined using diffusion-tensor magnetic resonance imaging [72, 73]. Comparisons between patient-specific models and experimental data show that the electrode-tissue interface (ETI) impedance and heterogeneities and anisotropies in tissue conductivity affect the distribution of electric potentials, and these features are important when modeling DBS [72, 73].

In addition, there are a number of approximations typically used when modeling DBS, and in many instances these approximations have not been validated. For example, one common assumption is that convergence of the potentials is a sufficient criterion for ensuring accurate determination of neural activation thresholds [70, 74, 75]. However, determination of activation thresholds requires calculation of the second difference of the potentials, which is subject to interpolation errors that depend on the size and order of the FEM elements [76]. Another common assumption is that the platinum-iridium (PtIr) electrode can be approximated as an ideal polarized electrode with capacitance independent of the applied stimulus [73, 77-79]. However, charge transfer at the ETI is both capacitive and Faradaic [67], and the capacitance of the ETI varies with the applied stimulus [80].

The goal of this study was to determine the impact of several common simplifications on the electrical potentials and neural stimulation thresholds calculated

with numerical models of DBS. We used a spatiotemporal model of a four-contact clinical DBS electrode to address the following questions: (1) How does the accuracy of calculation of the potentials and thresholds depend on FEM mesh parameters? (2) What effects do ignoring the inactive contacts and extending the terminated end of the shaft have on the potentials and thresholds? (3) What effects does simplifying the representation of the ETI with a lumped circuit representation have on the potentials and thresholds? And, (4) what effects does approximating the DBS contact with an ideal polarized electrode with a constant capacitance have on the potentials and thresholds? The results delineate the level of detail required in computational models of the electric fields produced by DBS to make accurate calculations of the neural response to DBS. The final version of this work is published in IEEE Transactions on Biomedical Engineering [81].

2.2 Methods

2.2.1 FEM Model

We constructed an FEM model of the Model 3387 electrode array (Medtronic Inc, Minneapolis, MN) in COMSOL Multiphysics v3.4 (COMSOL Inc., Burlington, MA) that consisted of four annular contacts on an insulating shaft surrounded by homogeneous tissue (Figure 2.1) representing a medium of infinite extent. Cylindrical annular contacts were 1.5 mm in height, 1.27 mm in diameter, 0.15 mm in thickness, spaced 1.5 mm apart, and had a conductivity of 9.5×10^6 S/m. Brain tissue can be approximated as primarily resistive for typical stimulation parameters used in DBS [82], so the permittivity of the

tissue was ignored. Grey matter was modeled as a 60 mm x 60 mm x 60 mm cube with an isotropic conductivity of 0.2 S/m [40], and white matter perpendicular (parallel) to the electrode was modeled as a 120 mm x 40 mm x 40 mm (40 mm x 40 mm x 120 mm) with an anisotropic conductivity of 0.1 S/m and 0.9 S/m transverse and longitudinal to the long axis of the prism, respectively [83].

Monopolar voltage-regulated stimulation was modeled by applying potentials of 1 V and 0 V (Dirichlet boundary conditions) on the surface of the stimulation electrode and outer surface of the tissue volume, respectively. The electrode shaft was assumed to be perfectly insulating and was modeled as a boundary layer with zero normal current density (Neumann boundary condition), except where the Dirichlet conditions were applied. At internal boundaries, the normal current density exiting/entering the surface of the electrodes was set equal to normal current density entering/exiting the adjoining tissue region (continuity).

The FEM model was discretized into a graded mesh of Lagrange tetrahedral elements, where the mesh density was greatest near the electrode surface, using a Delaunay triangulation algorithm. The potential distribution was calculated by solving Laplace's equation (Equation 2.1), where ∇ is the divergence operator, σ is the conductivity and $\vec{J}$ is the current density; and the current was calculated by integrating the current density (Equation 2.2) on the surface of the electrode, where $\vec{E}$ is the electric field.

$$\nabla \cdot \left(\sigma \cdot \nabla \Phi\right) = -\nabla \cdot \vec{J} = 0 \tag{2.1}$$

$$\vec{J} = \sigma \cdot \vec{E} \tag{2.2}$$

A convergence analysis was conducted to assess the effect of mesh parameters, including the number and order of elements, on the accuracy of the potentials and stimulation thresholds. The FEM model was initially solved using a coarse mesh, for elements of a set order, and the mesh was refined (i.e., the elements were split into smaller elements) until no further refinement was possible under the memory constraints (8 GB) of our work station. Error (δ) was defined as the root mean square deviation (RMSD) in the measured quantity (x) ± 1 standard deviation (SD), expressed as a percent relative to x after the mesh was refined:

$$\delta = RMSD\left\{\frac{x^{k+1} - x^{k}}{x^{k+1}}\right\} \pm SD\left\{\frac{x^{k+1} - x^{k}}{x^{k+1}}\right\} \tag{2.3}$$

where k denotes the number of refinements. A δ of 5 % was chosen as the value which all errors should fall below. In addition, we verified that the model was large enough to behave as an infinite medium by doubling the model volume and verifying that the lumped resistance of the model, the potentials, and the stimulation thresholds had a δ of < 5 %.

All subsequent results (except for those in our convergence analyses) were obtained using the maximum number of cubic elements possible: ~ 1.3 million cubic elements using 8 GB of memory. Mesh refinement from ~ 727,000 to ~1.3 million cubic elements and doubling the volume with ~ 1.3 million cubic elements yielded δ in the potentials and stimulation thresholds of < 1 % in the isotropic case and < 2 % in the anisotropic case.

2.2.2 Population model of myelinated axons

The NEURON simulation environment [84] was used to implement cable models of myelinated axons oriented parallel and perpendicular to the electrode axis. Axons were 2.5 μm in diameter, 15 mm in length, and the myelin was assumed to be perfectly insulating. Nodes of Ranvier contained a parallel combination of a nonlinear sodium conductance (1.445 S/cm^2), a linear leakage conductance (0.128 S/cm^2), and a membrane capacitance (2.5 μF/cm2) [85], as these conductances and capacitance are sufficient for predicting activation thresholds [86]. Model parameters reflected a mammalian axon at 37° C [87].

Based on predicted volumes of tissue activated with the Model 3387 for typical DBS parameters, neural elements are expected to be between ~0.9-2.9 mm from the surface of the electrode [72]. To span this range, populations of 100 axons were uniformly distributed in an annulus around the electrode with inner and outer radii of 1 mm and 4 mm, respectively. Uniform distributions of coordinates were randomly picked using a Latin Hypercube Sampling design, and the coordinates were uniformly mapped to

the annular volume in Cartesian coordinates using a coordinate transformation. Analyses were conducted on 3 independent populations of 100 model axons to ensure that the results were not dependent on the particular population. This left a 0.365 mm thick annular region immediately adjacent to the electrode that was intended to represent the space occupied by the glial scar. The scar thickness fell within the range of reported experimental values: 0-1 mm [88, 89], and since we focused on evaluating mesh parameters, electrode geometry, and the ETI, the scar had the same conductivity as the surrounding brain tissue.

For cases when the ETI was approximated as linear (see below), we used the interpolated potentials (between grid points) to stimulate the axon populations with a 100 μs monophasic rectangular pulse. Because of linearity, the potentials at a given stimulus amplitude were calculated by multiplying the 1V solution by a scalar. The stimulation voltage threshold for each fiber was calculated using a bisection algorithm (relative error < 1 %), and we constructed input-output curves of the activated population fraction as a function of the stimulation amplitude.

2.3.3 Simplifying the representation of the electrode

A number of published models have used a simplified model of the 3387 array (Figure 2.1) to study the effects of electrode geometry [37, 90] and the ETI [78] on DBS. The simplified geometry requires (1) ignoring the inactive electrodes (those that do not deliver charge) and replacing them with insulating boundary conditions, and (2)

extending the terminating end of the insulating shaft so that it terminates on the bottom boundary of the tissue box. The simplified model of the 3387 is used in our analyses, so we quantified the effects of these simplifications.

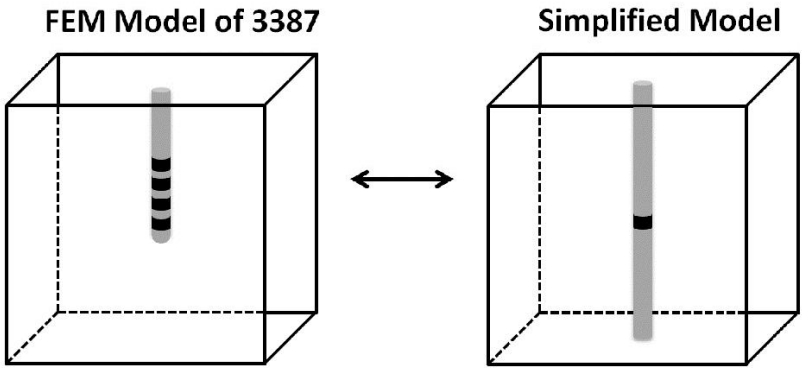

Figure 2.1: A Computational Model of Deep Brain Stimulation
The Model 3387 array was simplified by removing the inactive electrodes and extending the terminated end of the shaft.

2.2.4 Representation of the electrode-tissue interface

A simplified (Figure 2.1) axisymmetric FEM model of the 3387 array was constructed in MATLAB (v2008b, The Mathworks, Natick, MA) to study the filtering effects of a nonlinear ETI. The FEM model was discretized into a graded mesh of 40,000 bi-linear quadrilateral elements, which was enough to ensure that mesh refinement and doubling the volume of the model altered potentials and stimulation thresholds < 1 %.

We modeled the ETI using a thin-layer approximation [91, 92], given by the following Robin boundary condition:

$$-\hat{n}\cdot\vec{J} = r_f^{-1}\{\eta-\Phi_D\}(\eta-\Phi_D) + c_{dl}\{\Phi_D\}\frac{\partial}{\partial t}(\Phi_{stim}-\Phi_D) \tag{2.4}$$

$$\eta = \Phi_{stim} - \Phi_{OC} \tag{2.5}$$

where $\hat{n}$ is the surface unit normal vector, r_f is the distributed Faradaic resistance, c_{dl} is the distributed double-layer capacitance, Φ_{stim} is the applied potential on the electrode surface, Φ_D is the potential at the boundary between the compact and diffuse layers [93], and η is the overpotential, which is the potential difference between Φ_{stim} and the open-circuit (equilibrium) potential (Φ_{oc}). Although Φ_{oc} is non-zero for PtIr electrodes in brain tissue [80], it was ignored (Φ_{oc} = 0 V) to simplify the analysis of the FEM model.

We first conducted a sensitivity analysis to determine if the ETI could be ignored for typical DBS parameters, and subsequently, we determined whether the DBS electrode could be approximated as an ideal polarized electrode (r_f = infinity). Typical DBS parameters include pulsewidths (PWs) between 60-210 μs and amplitudes between 1-5 V [26]. Within this parameter range, r_f varies between 40-290 Ω-cm^2 and c_{dl} varies between 12-47 μF/cm^2 [80]. Therefore, stimulation thresholds of parallel and perpendicular fibers were calculated for PWs between 50-200 μs at each of the four bounds of the ETI parameter space: (r_f, c_{dl}) = (40, 12), (40, 47), (290, 12), and (290, 47).

Next, the FEM model with a constant r_f and c_{dl} (i.e., a linear model) was used to test the assumption that the distributed boundary of the ETI can be approximated with

equivalent lumped circuit values [78]. The time-varying potentials of the axisymmetric FEM model with the ETI (the spatiotemporal model) were compared to the potentials of the FEM model with no ETI (the static model) filtered by a three-element Randles equivalent circuit with a lumped access resistance, R_a, Faradaic resistance, R_f, and double layer capacitance, C_{dl}. R_a was calculated by taking the reciprocal of the current per applied volt in the static FEM model, R_f was calculated by dividing r_f by the electrode area (1.905π mm^2), and C_{dl} was calculated by multiplying c_{dl} by the electrode area.

Finally, we constructed a nonlinear model of the ETI with r_f and c_{dl} that varied with Φ_D. The initial values in the nonlinear case were the values of c_{dl} and r_f in the linear case. The nonlinear form of c_{dl} was taken from the Gouy-Chapman-Stern model, which models the c_{dl} as the series combination of an electrostatic capacitance, the Helmholtz capacitance (c_H), and a diffusive capacitance (c_D) [93].

$$\frac{1}{c_{dl}} = \frac{1}{c_H} + \frac{1}{c_D} \tag{2.6}$$

$$c_D = k_1 \cosh(k_2 \Phi_D) \tag{2.7}$$

$c_H = 45$ μF/cm^2, $k_1 = 31$ μF/cm^2, and $k_2 = 1.2$ V^{-1} in Equation 2.6 and Equation 2.7 were calculated by fitting Equation 2.6 to measured c_{dl} values of the 3387 electrode array in brain tissue [80]. The nonlinear form of r_f was derived by implicitly differentiating the

Bulter-Volmer Equation [93], taking the reciprocal, and adding a constant term to account for the effect of diffusion:

$$r_f(x) = \left\{ J_o \left[\alpha \cdot \beta \cdot \exp\left(-\alpha\beta\eta\right) + \left(1-\alpha\right) \cdot \beta \cdot \exp\left(\left(1-\alpha\right) \cdot \beta \cdot \eta\right) \right] \right\}^{-1} \quad (2.8)$$

J_o = 1 x 10^{-4} A/cm^2 is the exchange current density, α = ½ and β = 37.44 V^{-1} are constants derived from first principles [93], and r_{min} = 40 Ω-cm^2 is the minimum r_f at η = infinity. J_o and r_{min} were calculated by fitting Equation 2.8 to measured r_f values of the 3387 electrode array in brain tissue [80].

Nonlinear systems of equations were linearized using the Newton-Raphson method, and linear systems were solved using the built-in MATLAB solver. Time integration was carried out using the implicit trapezoidal method [76]. The derivation of the governing equations and details of the implementation of the FEM are provided in the Appendix. At each mesh node, the RMSD in the waveforms of potential versus time between the linear and nonlinear cases was compared to determine if the nonlinear impedance of the ETI could be approximated as constant for typical DBS parameters.

2.3 Results

We used FEM models of the Medtronic 3387 electrode, coupled with cable models of myelinated axons, to quantify how commonly used simplifications of

numerical models of DBS affect the calculation of the potentials and stimulation thresholds.

2.3.1 Number and order of FEM mesh elements

We quantified the error (Equation 2.3) in the potentials, the second difference of the potentials ($\delta^2\Phi$) between 3 consecutive nodes, which is proportional to the source driving membrane polarization [39], and stimulation thresholds to determine whether convergence of the potentials is a sufficient criterion for ensuring subsequent small errors in $\delta^2\Phi$ and stimulation thresholds. In an isotropic medium, 320,000 first order (O1), 29,000 second order (O2), and 8,000 third order (O3) were sufficient for ensuring the error in the interpolated potentials was < 5 % but were not sufficient for calculating $\delta^2\Phi$ and stimulation thresholds with an error of < 5 %. With these mesh parameters, the errors in $\delta^2\Phi$ were 41 $\pm$ 16 %, 24 $\pm$ 14 %, and 18 $\pm$ 10 %, respectively; and the errors in the stimulation thresholds were 19 $\pm$ 13 %, 14 $\pm$ 12 %, and 13 $\pm$ 8 %, respectively (Figure 2.2a). At least 320,000 O2 and 98,000 O3 elements were required for calculating $\delta^2\Phi$ with sufficient accuracy that the error in the stimulation thresholds was < 5 % (Figure 2.2a), while no number of O1 elements within the maximum number of elements tested (~ 2.3 million) was sufficient for calculating the stimulation thresholds to within 5 % accuracy.

In an anisotropic medium, 727,000 O1, 72,000 O2, and 22,000 O3 elements were sufficient for calculating the potentials with an error of < 5 % but not sufficient for calculating $\delta^2\Phi$ and the stimulation thresholds with an error of < 5 %. For this number of

elements, the errors in $\delta^2\Phi$ were 236 $\pm$ 79 %, 174 $\pm$ 151 %, and 207 $\pm$ 177 %, respectively; and the errors in the stimulation thresholds were 32 $\pm$ 16 %, 40 $\pm$ 28 %, and 44 $\pm$ 44 %, respectively (Figure 2.2b). 2.3 million O2 and 727,000 O3 elements were sufficient for calculating $\delta^2\Phi$ with enough accuracy that the error in the stimulation thresholds was < 5 % (Figure 2.2b). Therefore, in both the isotropic and anisotropic cases, convergence of the potentials was not sufficient for calculating the stimulation thresholds to the same accuracy.

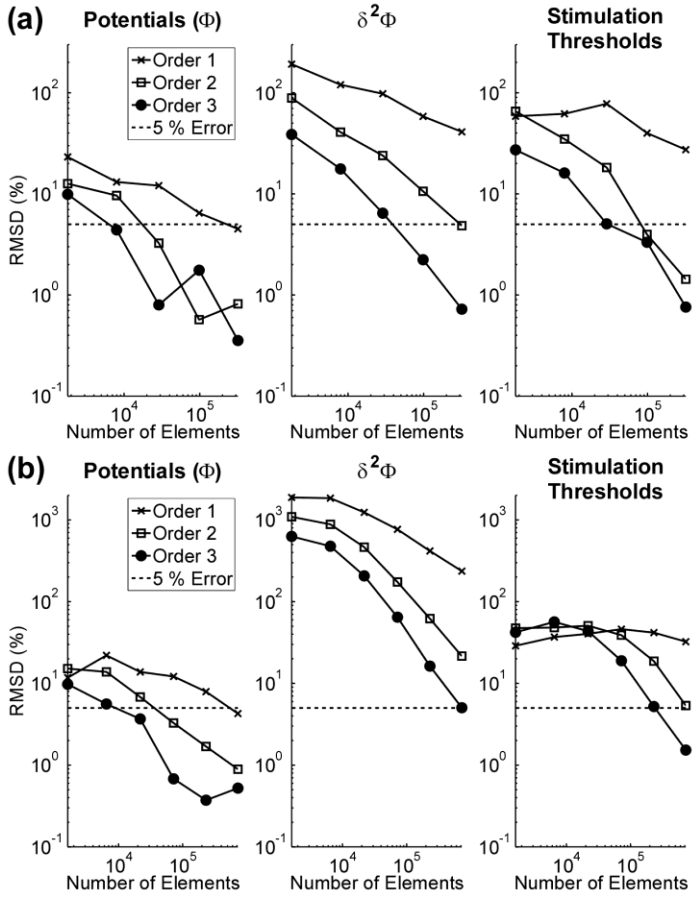

Figure 2.2: The effects of mesh parameters on interpolation error.
Effects of the number and order of finite elements on potentials, $\delta^2\Phi$, and stimulation thresholds in an (a) isotropic and (b) anisotropic media. Note: $\delta^2\Phi$ reflects the second difference of the potentials taken between 3 consecutive nodes of Ranvier in the modeled axon.

2.3.2 Volume of the FEM model

Doubling the volume of the isotropic model (60 x 60 x 60 mm^3) increased R_a by 0.6 %, which corresponded to an RMSD of 3.2 $\pm$ 0.4 %, 3.0 $\pm$ 1.9 %, and 0.4 $\pm$ 0.2 % in Φ, $\delta^2\Phi$, and the stimulation thresholds, respectively. Doubling the volume of the anisotropic model (120 x 40 x 40 mm^3) increased R_a by 0.5 %, which corresponded to an RMSD of 5.3 $\pm$ 0.7 %, 1.9 $\pm$ 2.2 %, and 0.6 $\pm$ 0.5 % in Φ, $\delta^2\Phi$, and the stimulation thresholds, respectively. Thus, the volume was large enough that the errors in R_a and the stimulation thresholds were < 5 %.

2.3.3 Simplifying the representation of the electrode

We quantified the RMSD of the stimulation threshold voltages to determine the effect of removing the inactive electrodes and extending the terminated end of the electrode shaft. Removing the inactive electrode contacts altered cathodic stimulation thresholds by -17 to +2.3 %, with an RMSD of 0.9 ± 2.3 %, and anodic stimulation thresholds by -6.3 to +13 %, with an RMSD of 2.3 ± 3.0 %. Extending the distal end of the shaft altered cathodic stimulation thresholds by -10 to +2.1 %, with an RMSD of 0.6 ± 1.2 %, and anodic stimulation thresholds by -2.9 to + 6.1 %, with an RMSD of 0.9 ± 1.3 %. Applying both simplifications produced cathodic stimulation threshold errors between -17 and + 2.5 %, with an RMSD of 1.5 ± 2.4 %, and anodic stimulation threshold errors between -6.2 and +18 %, with an RMSD of 3.2 ± 4.2 % (Figure 2.3a).

Thus, removing the inactive electrodes had the greatest effect on the stimulation thresholds.

The effect of geometric simplifications of the electrode on thresholds was dependent on the polarity of stimulation as well as the orientation of the axons. Across the 3 populations of 100 fibers, anodic stimulation threshold voltages in 78 (26 %) of the 300 parallel fibers increased > 5 % when using the simplified model of the 3387 array (Figure 2.3a). These 78 parallel fibers were the elements closest (< 1.6 mm) to the electrode surface. Similar to the parallel case, cathodic stimulation thresholds in the 30 closest (10 %) perpendicular fibers increased > 5 % (Figure 2.3a). Inspection of the potentials showed that the inactive electrodes had an effect on the distribution of potentials near the electrode shaft. Parallel to the electrode, the presence of the inactive contacts increased the magnitude of the secondary lobes of $\Delta^2\Phi$ (virtual anodes / cathodes), and perpendicular to the electrode, the presence of the inactive contacts decreased the magnitude of the primary lobe of $\delta^2\Phi$ (Figure 2.3b).

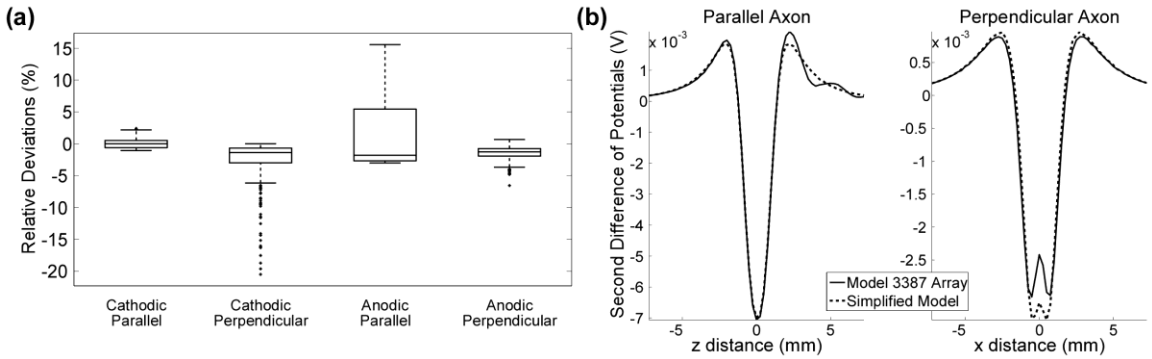

Figure 2.3: Effect of simplifying the representation of the Medtronic 3387 array.
(a) Distributions of relative deviations in the stimulation thresholds between the simplified model and the 3387 electrode array. Outliers (greater than 1.5 times the interquartile range) are denoted by solid dots. (b) The centered second difference of the potentials generated by the 3387 array and the simplified model for representative parallel (left) and perpendicular (right) axons located <1.6 mm from the electrode surface.

Overall, the RMSD of the stimulation thresholds was < 5 % in all cases, except for anodic stimulation of parallel fibers, where the RMSD was > 5 %. Therefore, unless quantifying the activation of parallel neural elements < 1.6 mm from the electrode surface during anodic stimulation, the simplified representation of the 3387 array was sufficient.

2.3.4 Representation of the electrode-tissue interface

We analyzed the dependence of threshold voltages on c_{dl} and r_f to determine if the ETI could be ignored for typical DBS parameters. Ignoring the ETI altered the RMSD of the stimulation thresholds for parallel and perpendicular fibers between 2 and 7 % for a PW = 50 μs, between 4 and 14 % for a PW = 100 μs, and between 7 and 23 % for a PW = 200 μs (Figure 2.4). For each combination of c_{dl} and r_f, further increasing r_f to infinity increased the RMSD of the stimulation thresholds with increasing PW, but the largest

RMSD was 2.1 ± 0.2 % (Figure 2.4). Therefore, for typical DBS parameters, the ETI has a marked effect on the stimulation thresholds, but the ETI can be simplified by setting r_f to infinity (i.e., the DBS electrode could be approximated as an ideal polarized electrode).

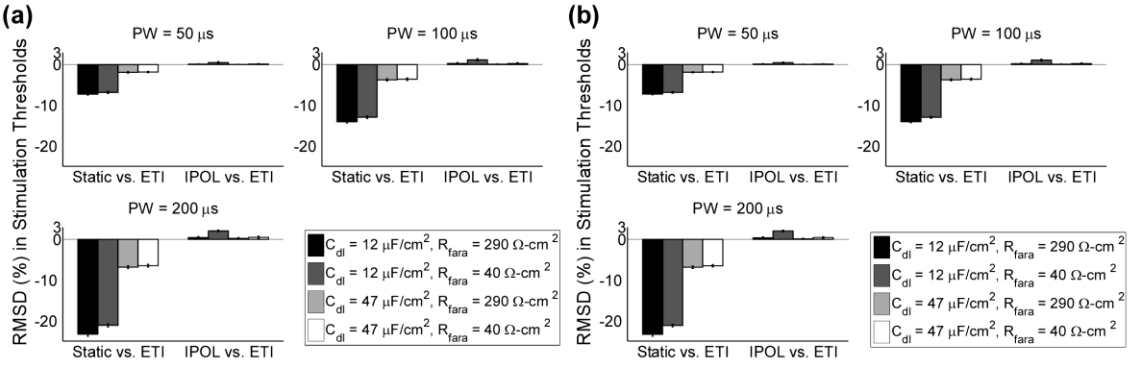

Figure 2.4: The effect of the ETI impedance on the threshold voltages to activate a population of model axons.
(a) The RMSD of the stimulation threshold voltages for a population of parallel fibers at different PWs. Relative errors were calculated for two cases: between the linear and static models with and without the ETI, respectively (Static vs. ETI), and between the linear model with a constant r_f and c_{dl} and a corresponding ideal polarized electrode (IPOL) model with only a constant r_f (IPOL vs. ETI). (b) As in a, but for perpendicular fibers.

At each mesh node, we compared the waveforms of potential versus time between the axisymmetric spatiotemporal FEM model and the static FEM model filtered by a 3-element Randles equivalent circuit of lumped R_a, R_f, and C_{dl}. For PW = 1 ms, the RMSD between the waveforms of the two models at all mesh nodes ranged from 3 - 12 %. The largest errors occurred within 0.1 mm of the electrode surface and declined to a minimum value 0.6 mm from the electrode surface (Figure 2.5). The RMSD at all points within the region where axons were seeded was < 5 %, so the spatiotemporal FEM model can be simplified using the filtered static model.

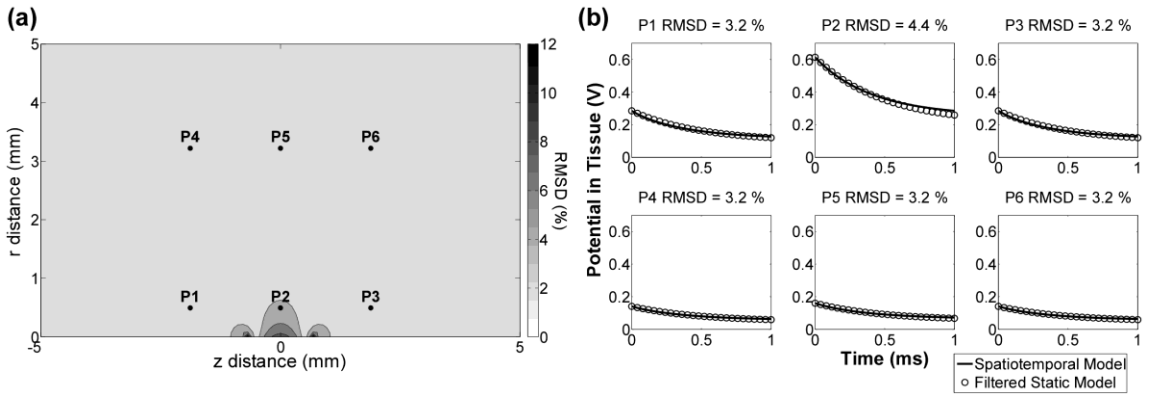

Figure 2.5: The distributed ETI impedance can be approximated by filtering the static potentials with a lumped equivalent circuit.
(a) The RMSD in the waveforms of the potential versus time (0-1 ms) at each node between the spatiotemporal and filtered static models. The electrode contact is centered at z = 0 mm (with respect to the electrode center) and the semi-infinite domain extends in the r direction (with respect to the electrode surface). (b) Tissue potentials vs. time at the six locations shown in a.

The c_{dl} varies as a function of the applied potential for typical stimulation amplitudes [80, 93] but is often approximated as constant. Because the RMSD of the stimulation threshold voltages was < 5 % when r_f changed from 40 Ω-cm to infinity, we approximated the 3387 array as an ideal polarized electrode and compared waveforms of potential versus time at the mesh nodes when c_{dl} was linear and nonlinear (Figure 2.6a). For a PW = 210 μs, the RMSD in the waveforms between the linear and nonlinear models ranged from 0.3-1.2 % (Figure 2.6b), 0.2-0.7 %, and 0.2-0.4 % at stimulus amplitudes of 1 V, 3 V, and 5 V, respectively. In all cases, the largest errors were located near the electrode surface. In addition, at 1 V, 3 V, and 5 V, the RMSD in the waveforms between the two models was < 5 % across all mesh nodes for PWs up to 560 μs, 780 μs, and 1000 μs, respectively. Therefore, for typical stimulation parameters, although the c_{dl}

varies nonlinearly with the applied potential, it varied slowly enough with time that it could be approximated as quasi-static. That is, the nonlinear c_{dl} at a given applied potential can be approximated by evaluating Equation 2.6 at the beginning of each phase of the rectangular stimulation pulse and keeping c_{dl} constant throughout the duration of each phase.

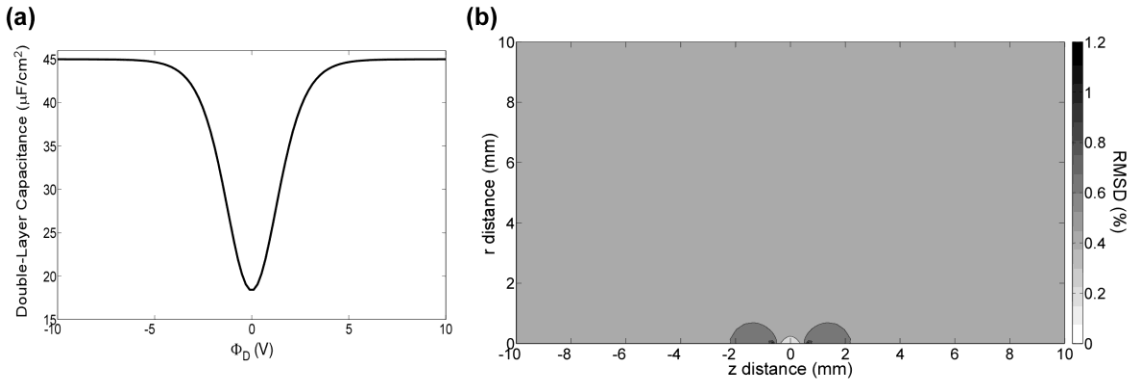

Figure 2.6: The effect of a nonlinear c_{dl} on the potentials.
(a) The relationship between c_{dl} and the potential at the boundary between the compact and diffuse layers (Φ_D) (b) The RMSD in the waveforms of potential versus time (PW = 210 μs) at all mesh nodes between the linear and nonlinear models when the nonlinear c_{dl} changed most drastically (Φ_{stim} = 1 V). The electrode contact is centered at z = 0 mm and the semi-infinite domain extends in the r direction

2.4 Discussion

We quantified the effect of model simplifications on the electrical potentials and excitation thresholds in FEM models of DBS. The results yielded four important conclusions. One, convergence of $\delta^2\Phi$, regardless of the element order, should be used to assess numerical accuracy when coupling numerical volume conductor models with cable-based models of neural elements, and cubic or greater elements should be used to avoid discontinuities in the calculation of $\delta^2\Phi$. Two, simplifying the 3387 array by

ignoring the inactive contacts and extending the terminated end of the shaft has position dependent effects on the potentials and excitation thresholds, and these effects may impact correlations between DBS parameters and clinical outcomes. Three, when the current density in the bulk tissue is approximately uniform, the effect of the ETI impedance can be approximated by filtering the static model of the DBS electrode with lumped parameter electrical equivalent circuit. And four, for typical DBS parameters during voltage-regulated stimulation, the PtIr electrode contact can be approximated as an ideal polarized electrode with a nonlinear double-layer capacitance, and if the applied potential on the electrode surface is constant, the double-layer capacitance at a given applied potential can be treated as quasi-static.

2.4.1 The effect of interpolation on electric potentials and neural activation

A frequently used criterion for assessing the accuracy of solutions in FEM models of DBS is convergence of the potentials. Elements of any order (≥ 1) can be used to interpolate potentials without discontinuities, but unless O3 or greater elements are used, discontinuities arise when calculating $\delta^2\Phi$, which lead to errors in activation thresholds that exceed the errors in the potentials (Figure 2.2, Figure 2.7). This explains why, for example, (much) greater than 30 times as many (O1) O2 elements were required to reach the same accuracy in $\delta^2\Phi$ as the potentials, while only 10 times as many O3 elements were required to reach the same accuracy in $\delta^2\Phi$ (Figure 2.2a). Therefore, O3 or greater elements should be used to avoid discontinuities when calculating $\delta^2\Phi$ in FEM models of

DBS, and convergence of $\delta^2\Phi$ should be used to assess numerical accuracy of the solution.

Using higher order elements comes at the expense of increased computational time, as the computational cost of using an element of order P is proportional to NP^{d+1} [94], where N is the number of elements and d is the number of dimensions. In our 3D model, it took 10 times as many O2 elements as O3 elements to reach the same accuracy in $\delta^2\Phi$. Because solving 10 times as many O2 elements took ~ 50 % longer, O3 elements were more efficient at calculating $\delta^2\Phi$. However, O3 elements are not necessarily the most efficient choice in all cases.

The rate of convergence for increasing element order is exponential in regions where the solution is smooth, so O4 or greater elements could be potentially more efficient far from the electrode [95]. However, in regions where the solution is not smooth, for example, where heterogeneous electrical properties create large gradients in the potentials, [96], increasing element order has only an algebraic rate of convergence and using a greater number of lower order elements is preferred [95]. Large gradients in the potentials are certainly expected in patient-specific models of the brain, which include inhomogeneous and anisotropic tissue electrical properties; therefore, a mixed method [97], where O1-O3 elements are used near to electrode, where the potentials are not smooth, and O4 or greater elements are used far from the electrode, where the potentials are smooth, is expected to be the most computationally efficient choice of mesh parameters.

2.4.2 Simplifying the representation of the electrode

The Medtronic 3387 electrode array is axially symmetric; therefore, when the surrounding tissue is also axially symmetric, a two-dimensional geometry can be used to represent the electrode. In addition, previous studies have proposed simplifying the 3387 array by ignoring the inactive electrode contacts and extending the terminated end of the shaft [37, 77, 78, 90]. Removing the inactive electrodes and extending the terminated end of the shaft had position dependent effects on the potentials (Figure 2.3a), and the effect of the former was more pronounced.

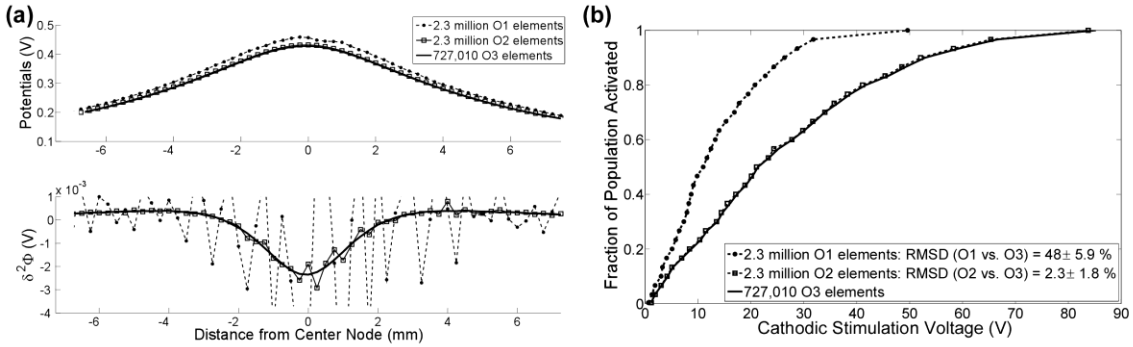

Figure 2.7: Interpolation of the potentials with O1 and O2 elements creates discontinuities in $\delta^2\Phi$ and errors in stimulation thresholds.
(a) The interpolated potentials and corresponding $\delta^2\Phi$ across a representative fiber in an anisotropic media. (b) Input-output curves of the fraction of perpendicular axons activated versus the cathodic stimulation voltage for the mesh parameters in part a. The RMSD of the stimulation thresholds between the case and O3 elements is shown in the legend.

The inhomogeneities created by the highly conductive inactive contacts generated local short circuits adjacent to the tissue that had two effects on the potential. First, the inactive electrodes increased the magnitude of the "virtual cathodes" in $\delta^2\Phi$ by flattening the potential distribution along the electrode shaft, and second, the inactive electrodes decreased the magnitude of the primary cathode in $\delta^2\Phi$ by shunting current longitudinally

along the electrode shaft (Figure 2.3b). In our computational model, these shaping effects extended up to 1.6 mm from the electrode surface. Since the spatial extent of this effect is expected to depend on a number of factors, including the geometry of the electrodes and the electrical properties of the surrounding tissue, and since the closest neural elements activated during DBS are certainly expected to lie within millimeters of the electrode surface [72], the effects of simplifying the electrode geometry should be confirmed before using a simplified model to make correlations between stimulation parameters and clinical outcomes.

2.4.3 Representation of the electrode-tissue interface

Different representations of the ETI have been used in previous studies analyzing the filtering effects of the ETI [78, 92, 98]. Although these studies agree that the effects of the ETI cannot be ignored during typical stimulation parameters, it is important to establish what level of detail is appropriate for modeling the ETI.

One question the results addressed is whether the PtIr electrode can be modeled as an ideal polarized electrode [78]. For typical stimulation parameters, the charge injected per pulse does not exceed the reversible charge injection capacity of PtIr [67, 99], so irreversible charge transfer occurs at a slow rate and can be ignored. However, reversible charge transfer with PtIr can include both capacitive and Faradaic pathways [67]. Our results showed that DBS electrode could be approximated as an ideal polarized electrode during voltage-regulated stimulation (Figure 2.4), but this was not because the Faradaic

current was small compared to the capacitive current, but rather, because the charging of the ETI was insensitive to changes in the Faradaic current.

For example, for any combination of r_f and c_{dl}, increasing r_f from its minimum value to infinity had a much smaller effect than increasing c_{dl} from its minimum to maximum value (Figure 2.4). This can be explained qualitatively by examining the time constant (τ) of an equivalent Randles circuit of the DBS electrode:

$$\tau = \frac{C_{dl} R_a R_f}{R_a + R_f} \tag{2.9}$$

τ is proportional to C_{dl} and the parallel combination of R_a and R_f. Because τ is only proportional to R_f when $R_f << R_a$, and R_f is greater than or equal to R_a for a PtIr electrode in brain tissue [80], τ is more sensitive to changes in C_{dl}. However, one should use caution when approximating the PtIr electrode as an ideal polarized electrode when $R_f << R_a$, or during current-regulated stimulation, because in both cases τ is directly proportional to both C_{dl} and R_f.

We also addressed the nonlinear dependence of r_f and c_{dl} on the electrode potential [80]. For voltage-regulated stimulation, the nonlinear r_f can be ignored and the nonlinear c_{dl}, despite its nonlinear dependence on Φ_D (Figure 2.6a), varies slowly enough in time that for typical stimulation parameters it can be approximated as quasi-static, where the constant value is determined using Equation 2.6. Prior work modeled a nonlinear ETI with an r_f and c_{dl} that varied with both frequency and amplitude, and

assessed how the ETI impedance affects $\vec{J}$ on the electrode surface [92]. Our work builds on this prior work by evaluating the impact of a nonlinear r_f and c_{dl} on activation thresholds for voltage-regulated stimulation and addressing the level of detail required for capturing these effects.

2.4.4 Representing effects of the ETI impedance

In FEM models of electrical stimulation, the ETI can be represented with a distributed boundary condition [91, 92] or with lumped circuit values [78]. Using the product of separate spatial and temporal solutions, where the static model solved the potential distribution in space and the Randles circuit solved the decay of the potentials over time, was indeed accurate. In other words, $\vec{J}$ was approximately spherically uniform in the regions where the axons were seeded, so the rate of decay of $\vec{J}$ in the bulk tissue could be described with a single equivalent time constant. However, heterogeneities in the tissue conductivity, such as cysts filled with cerebral-spinal fluid [100] or encapsulation tissue [77], can alter $\vec{J}$ in the bulk tissue. In cases where $\vec{J}$ is not (spherically or elliptically) uniform, the charging of the ETI cannot be described with a single τ [101], and such cases may require explicit representation of the ETI in time-dependent models.

2.4.5 Model Limitations

Two limitations in this study bear consideration. The first limitation is using a simplified (SW) model of a mammalian nerve fiber with perfectly insulating myelin, rather than a more detailed (MRG) axon model that better replicates the excitability of a mammalian nerve fiber [102]. Although the SW model does not reproduce the depolarizing after-potential and after-hyperpolarization [102], which account for the increased excitability of the axon following an action potential, it does reproduce conduction velocities [85], strength-duration and strength-distance relationships observed in mammalian fibers [103], and is much less computationally demanding than the MRG model.

The SW and MRG models have a single and double cable structure, respectively, but both have source terms (on the right-hand side of the cable equation) that are dependent on $\delta^2\Phi$. To analyze the effect of interpolation error on modeled MRG axons, additional simulation were conducted. 4832 O1, O2, and O3 elements yielded errors in the stimulation thresholds of 45 $\pm$ 23 %, 18 $\pm$ 13 %, and 5 $\pm$ 4 %, respectively. Therefore, the same qualitative trends observed with the SW model are expected to carry over in more detailed models of neural elements.

The second limitation is not accounting for the low conductivity of the glial scar, which has the effect of increasing R_a by as much as 800 Ω and thereby influencing stimulation thresholds [77]. Clinical measurements of DBS electrode impedances typically range from 500-1500 Ω. Our computational model had R_a of 650 Ω and an ETI

impedance that ranged between ~430-4,700 Ω for 10-1000 Hz, so the total impedance of the electrode fell within the range of clinical impedances. Yet, R_a was underestimated, which would have an impact on the charging of the ETI for voltage-regulated stimulation (Equation 2.9). Increasing R_a would increase τ, which would cause the ETI to charge more slowly, so our results should be interpreted as the maximum possible error.

2.5 Conclusion

We quantified how interpolation error, electrode geometry, and the representation of the ETI affected the electric fields produced by DBS. The choices of mesh parameters, the representation of the inactive electrodes, and the nonlinear electrical properties of the ETI all had a marked effect on the calculated potentials and thresholds. Previous studies looking at computational models of DBS have shown that representations of the ETI [78], the glial scar [77], and anisotropies and inhomogeneities in the electrical properties of the brain tissue [72], [73], [100], [104] are critical for accurate predictions of clinical data. Further, previous studies have shown that uncertainty in the electrical properties of brain tissue [105] and their dispersive nature [98] can have an impact on calculated potentials. Our work builds on these previous studies by delineating the mesh parameters and level of detail in the electrode geometry and ETI required to accurately calculate stimulation thresholds.

Computational models are not only useful for understanding the mechanisms of DBS but also for studying the neural origins of biological signals that can be used to provide closed-loop control of DBS [106]. Models of closed-loop DBS require accurate

predictions of the neural elements activated and their subsequent neural response. Interpolation errors and simplifications of the electrode array and ETI can certainly affect predicted stimulation thresholds and also the recorded neural signal. For example, representation of the ETI is important for capturing the (low pass) filtering effects of the ETI on the recorded signal. Therefore, the results have a broader impact on computational models used to study in vivo sensing and control for DBS.

Chapter 3 : Evaluation of High-Perimeter Electrode Designs for Deep Brain Stimulation

3.1 Introduction

Electrical stimulation of the nervous system is an effective therapeutic modality for treating neurological disorders. One of the most successful examples is deep brain stimulation (DBS), where a surgically implanted metal electrode array is used to deliver 100-200 Hz electrical pulses within specific regions of the brain. DBS is effective in treating movement disorders, including Parkinson's disease (PD) and essential tremor [1, 2], and recent clinical studies have shown DBS to be a promising therapy for treating epilepsy and psychiatric disorders [5, 6]. Yet, despite the success of DBS, there are several areas where the therapy can be improved. The objective of the present study was to determine the effect of electrode geometry on the efficiency of stimulation, as this impacts the lifetime of the implanted pulse generators (IPG) used to deliver DBS.

The IPGs used in DBS have an average battery life of 2-5 years [107, 108]. Since the battery life of the IPG is less than the treatment duration, patients using DBS require repeated battery replacement surgeries, which are costly and obligate the patient to incur repeatedly the risks associated with surgery, including infection [22, 23] and misprogramming [24]. Rechargeable IPGs (RPGs) are an alternative to primary cells: they have longer predicted battery lives but are more costly, need to be recharged on a regular basis, and are not well accepted [109]. For example, in a cohort of 35 patients

implanted with an RPG for spinal cord stimulation, 19 patients stated that they would have tolerated a 25 % larger RPG to relieve them of the burden of recharging, while 5 patients stated they would have tolerated a 50 % larger RPG [109]. Therefore, RPGs are not a panacea for limited device lifetimes, and stimulation efficiency needs to be improved.

The source driving polarization of the neural membrane is proportional to the second order (centered) difference of the extracellular potentials ($\delta^2\Phi$) for myelinated axons and the second order spatial derivative of the extracellular potentials (Φ'') for unmyelinated axons and dendrites [39]. Because the magnitude of the extracellular potentials (and thereby $\delta^2\Phi/\Phi''$) is proportional to the applied current, and because the lumped access/series resistance of the electrode (R_a) is inversely proportional to the area of the electrode, stimulation efficiency can be increased by increasing electrode area [77], which reduces R_a.

R_a can also be decreased by increasing the perimeter of the electrode. An electrode inlaid in an insulating substrate generates a current density on its surface that is minimal at the electrode center and maximal at the edges (or perimeter) where the conductor and insulator meet. This phenomenon, referred to as "field fringing" or "edge effects", occurs because charges on the edges, those which are not completely surrounded by neighboring charges, have the greatest access to the tissue. Therefore, in addition to an increased electrode area, an increased electrode perimeter may also increase stimulation efficiency [36, 37, 75].

The goal of this study was to determine which geometrical parameter, perimeter or area, more effectively increased stimulation efficiency. We modeled and tested eight prototype electrode designs with different areas and perimeters. First, we developed finite element method (FEM) models of the electrode designs to quantify the corresponding potential distribution, current density, and R_a of each design. Next, the FEM models were coupled with cable models of passing axons to quantify stimulation efficiency. Finally, we quantified in vitro the electrical properties of our electrode designs and measured in vivo the stimulation efficiency following acute implantation in anesthetized cats. The outcome of this effort is a fundamental understanding of the features of electrode geometry that are the most important for designing the next generation of DBS electrodes. The final version of this work is published in the Journal of Neural Engineering [38].

3.2 Methods

3.2.1 Fabrication of electrode designs

Eight prototype electrode designs were fabricated by sputter depositing a chrome adhesion layer followed by a gold metal layer onto a planar polyimide substrate (Figure 3.1a). Planar substrates were wrapped around and bound to a steel cylindrical shaft to form cylindrical electrodes for stimulation in vivo.

Two different high-perimeter electrode designs were used to test the hypothesis that increased electrode perimeter from segmentation and/or increased edge curvature could decrease R_a. On one array, we tested a set of serpentine-edge or Serp (S) designs,

consisting of two Serp electrodes, S1 and S2, and two banded electrodes, S3 and S4, which served as respective controls. The effect of perimeter was assessed by comparing S2 vs. S4 and S1 vs. S3; and we assessed whether the effect of area or perimeter was greater by comparing S1 vs. S2, S1 vs. S4, S2 vs. S3, and S3 vs. S4. Area was only reduced by factor of 1/3 to maintain the same edge-to-edge effective length between designs with different areas and the same type of edge (flat or serpentine), and increases in perimeter were capped at 300 % for a given area because increases greater than this could potentially generate charge densities per phase that are damaging to the electrode and neural tissue [75].

On another array, we tested a set square-edge or Rook (R) designs, consisting of three Rook designs (R1, R2, and R3) and a banded electrode (R4) that served as a control. We were interested in rook electrodes because of their sharp edges, or areas of curvature approaching infinity, that could potentially enhance the "edge effect" while keeping the average charge density per phase within a range that has been deemed potentially non-damaging [69]. The effect of perimeter was assessed by comparing R1 vs. R4, and we assessed whether the effect of area or perimeter was greater by comparing R1 vs. R2, R1 vs. R3, R2 vs. R4, and R3 vs. R4. R2 and R3, which had an equal area and perimeter, were compared to assess the importance of the edge-to-edge electrode length.

(a)

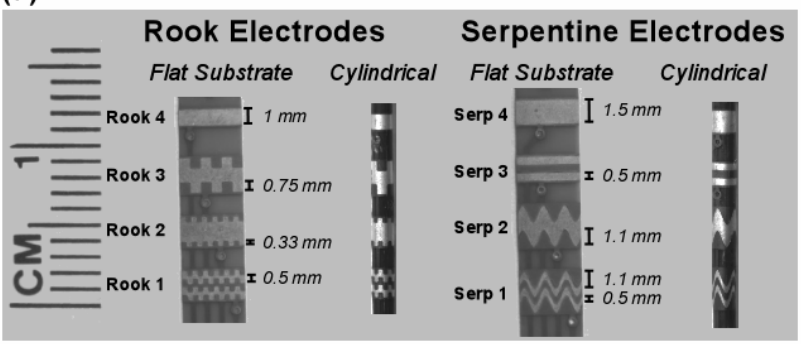

(b)

Electrode	Area (mm^2) $A = 1.905\pi$	Perimeter (mm) $P = 2.540\pi$
Rook 1	(2/3)·A	4·P
Rook 2	A	2·P
Rook 3	A	2·P
Rook 4	(2/3)·A	P
Serp 1	(2/3)·A	6·P
Serp 2	A	3·P
Serp 3	(2/3)·A	2·P
Serp 4	**A**	**P**

Figure 3.1: High-perimeter electrode designs for increasing the power efficiency of electrical stimulation.
(a) Photomicrograph of the prototype electrode designs. (b) The area and perimeter of each electrode design as a fraction of the electrode dimensions of Serp 4, the lead presently used in DBS for Parkinson's disease. The area (A) and perimeter (P) of Serp 4 are in units of π.

3.2.2 Computational model of deep brain stimulation

We implemented a computational model of deep brain stimulation (DBS) consisting of a three dimensional FEM model of each prototype electrode within a volume conductor representing the tissue medium and cable-based models of passing myelinated axons [110]. The FEM model, implemented in COMSOL Mutiphysics v3.4, included a single DBS electrode contact on an insulating shaft surrounded by brain tissue [81]. Each electrode had a radius of 0.635 mm and longitudinal dimensions shown in Figure 3.1a. The volume conductor was large enough (60 mm x 60 mm x 60 mm cube) that doubling its volume resulted in a less than 5 % change in both the calculated potentials (Φ) and $\delta^2\Phi$. The electrical conductivity of the volume (0.2 S/m, [40] was homogeneous, isotropic and purely resistive [82]. The volume was discretized using ~ 0.5 million 3rd order Lagrangian elements, because interpolation of $\delta^2\Phi$ without discontinuities requires third order or greater elements [81]. The mesh density was fine

enough such that additional mesh refinement (i.e., subdivision of the elements) altered Φ and $\delta^2\Phi$ by less than 1 % and 2 %, respectively.

A normal current density of 0 A/mm^2 (i.e., a Neumann boundary condition) was imposed on the electrode shaft to model a perfect insulator, and fixed potentials of 1 V and 0 V (i.e., Dirichlet boundary conditions) were imposed on the electrode surface and outer boundary, respectively, to model monopolar stimulation. (Note, we do not distinguish between current-regulated stimulation and voltage regulated stimulation in the static case, when no interface is present, because the applied voltage and applied current are constant.) The electric potentials were calculated by solving Laplace's equation (Equation 2.1), and the applied current was calculated by integrating the current density (Equation 2.2) over the surface of the electrode. Changes in Φ and $\delta^2\Phi$ in the FEM model from mesh refinement and volume doubling resulted in < 1 % change in the calculated stimulation thresholds.

R_a was calculated by dividing the applied voltage by the resulting current. In an infinite medium, R_a can be broken into two parts: the distributed resistance of the modeled domain and the lumped resistance between an equipotential surface and infinity [91]. All electrodes produced equipotential surfaces that were approximately spherical well within the bounds of the modeled domain, so a point-source electrode was used to approximate the lumped resistance of the tissue medium. The distributed resistance of all electrode designs was > 80 times the lumped resistance between the outermost boundary and infinity (an error of < 2 %), so the distributed resistance calculated with the FEM model served as a suitable approximation for the true R_a.

Cable models of myelinated axons were implemented in the NEURON v7.1 simulation environment [84]. Each axon was 2.5 μm in diameter, 15 mm in length, and oriented either parallel or perpendicular to the electrode axis. The neural membrane at each node of Ranvier contained the parallel combination of a nonlinear sodium conductance (1.445 S/cm^2), a linear leakage conductance (0.128 S/cm^2), and the membrane capacitance (2.5 $\mu F/cm^2$), as these conductances [85] are sufficient for predicting activation thresholds [86]. The myelin between nodes of Ranvier was assumed to be perfectly insulating.

The FEM and cable models were coupled to analyze the power efficiency of each electrode design. Populations were represented by 100 model axons uniformly distributed in an annulus around the electrode. Based on predicted volumes of tissue activated with the Model 3387 for typical DBS parameters, neural elements are expected to lie between ~0.9 and 2.9 mm from the surface of the electrode [72]. To span this range, population of axons were uniformly distributed in an annulus around the electrode with an inner and outer radius of 1 and 4 mm, respectively. Polar coordinates (r, θ) were picked using a Latin hypercube sampling, and r and θ were mapped to x and y using a coordinate mapping that maintained a uniform distribution in Cartesian coordinates.

The extracellular potentials at the nodes of Ranvier of the myelinated axons were determined via cubic interpolation from the potentials at the FEM grid points, and the interpolated potentials were used in NEURON to stimulate the population of passing axons with a 500 μs monophasic rectangular pulse. Because the conductivity was linear,

the potentials at a specific stimulation voltage were calculated by multiplying the 1V solution by a scalar. The threshold stimulation voltage to activate each model axon was calculated using a bisection algorithm (relative error < 1 %), and electrical power was calculated as the product of the stimulation threshold voltage and the corresponding current. Input-output (activation) curves of power versus the fraction of axons activated were used to assess power efficiency.

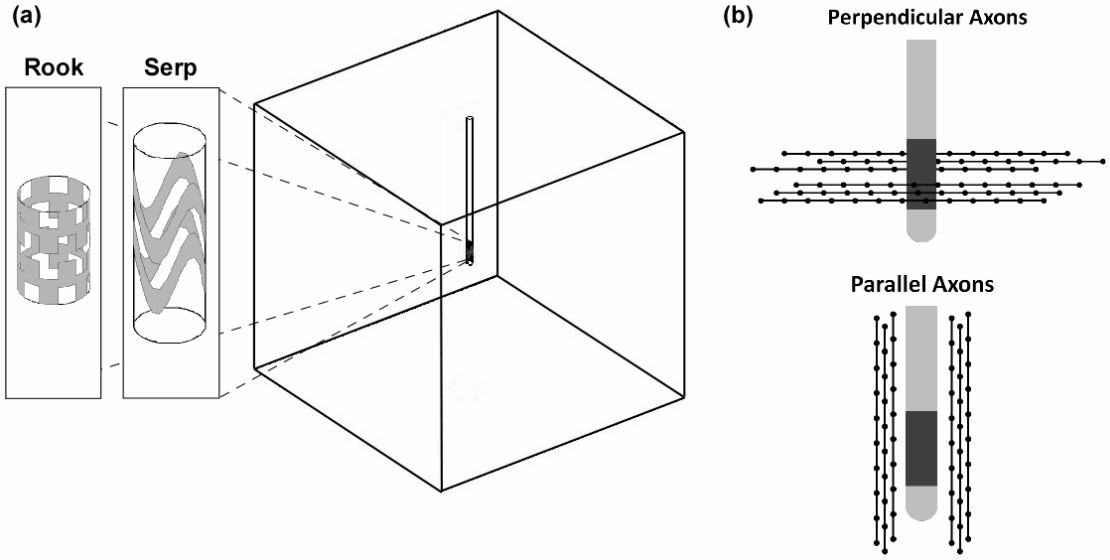

Figure 3.2: The FEM electrode model and the surrounding neuronal elements.
(a) The electrode and shaft were positioned such that the center of the electrode was at the origin of a conducting cube (60 mm x 60 mm x 60 mm), and the axis of the shaft was oriented in the z direction. (b) Examples of randomly positioned passing axons distributed either perpendicular or parallel to the electrode surface.

3.2.3 In vitro measurements

Measurements of voltage transients during applied current pulses and electrochemical impedance spectroscopy were conducted in vitro using the three-

electrode technique in a single-compartment electrochemical cell. We used a large-area (4 cm^2) platinum wire mesh as the counter electrode (CE), a silver/silver chloride (Ag/AgCl) electrode (Model RE-5B, BAS Inc., West Lafayette, IN, USA) as the reference electrode (RE), and the electrode design being tested was the working electrode (WE). All measurements were made at 37˚C using an electrolyte model of interstitial fluid (2 mM Na_2HPO_4-$7H_20$, 0.5 mM NaH_2PO_4-H_20, 28 mM $NaHCO_3$, 7.5 mM $KHCO_3$, 110 mM NaCl, 0.5 mM $MgSO_4$, 0.5 mM MgCl, 0.5 mM $CaCl_2$) that was bubbled with a mixture of gas (5% O_2, 6% CO_2, and 89% N_2) to maintain a pH of 7.4 [111]. Before each experiment, metal electrodes were cleaned in a 2 M solution of sulfuric acid (H_2SO_4) for 30 minutes, sonicated in 70% ethanol for 30 minutes, and rinsed in deionized water [112-114].

Voltage transients were generated by delivering 1 ms symmetric biphasic rectangular current pulses between the WE and CE at three amplitudes: 0.1 mA, 0.5 mA, and 1 mA. Measurements were repeated three times at each current level. The voltage transients were measured between the WE and RE using an isolated differential amplifier (100 MΩ input impedance, Model SR560, Stanford Research Systems, Sunnyvale, CA, USA) and recorded in MATLAB using the Data Acquisition (DAQ) Toolbox at a sampling rate of 40 kHz.

Electrochemical impedance spectroscopy was conducted using an electrochemical interface and frequency response analyzer (ECI Model 1287 and FRA Model 1252, Solartron Analytical, Hampshire, UK). The FRA applied a (10 mV) sinusoidal voltage superposed with a 0.3V DC bias voltage, and the ECI measured the resultant current

between the WE and RE. The frequency of the applied sinusoidal voltage was varied between 1 Hz and 10 kHz.

3.2.3.1 Calculating Randles circuit values from voltage transients

The voltage (V_{cr}) across a three-element Randles equivalent circuit in response to a current pulse is described by Equation 3.1: where, I_{cr} is the applied current, V_0 is the initial voltage at t = 0, R_f is the Faradaic (charge-transfer) resistance, C_{dl} is the double-layer capacitance, R_a is the access (or series) resistance of the electrolyte/tissue, PW is the pulse width of the current pulse, and τ_{cr} is the time constant (Equation 3.2). In general, R_f and C_{dl} vary nonlinearly with the electrode potential, and R_f is not symmetric about the open-circuit potential. Therefore, R_a, R_f, and C_{dl} were determined by using nonlinear regression to fit Equation 3.1 to each phase of the recorded response: the first phase, $0 \leq t < PW$; the second phase, $PW \leq t < 2PW$; and the terminal phase, $t \geq 2PW$.

$$V_{cr}(t) = e^{-t/\tau}(V_o - I_{cr}\left(R_a + R_f\right) + I_{cr}\left(R_a + R_f\right) \tag{3.1}$$

$$\tau_{cr} = R_f C_{dl} \tag{3.2}$$

3.2.4 In vivo power efficiency analysis

Acute in vivo experiments were conducted in anesthetized cats using a protocol approved by the Institutional Animal Care and Use Committee of Duke University.

Anesthesia was induced with ketamine HCL (Ketaset 35 mg/kg IM, supplemented as required at 15 mg/kg during surgical preparation) and maintained with alpha-chloralose (65 mg/kg IV, supplemented at 15 mg/kg). A 1 cm diameter craniotomy was made, the dura was reflected, exposing the cortex, and electrodes were implanted unilaterally in a vertical orientation (z direction) using stereotactic neurosurgical technique. We targeted the posterior internal capsule, which contains corticobulbar axons tracts projecting from the face region of the motor cortex [115], and is located 7 mm anterior, 10.5 mm lateral and 10 mm above the interaural line [83, 116].

An analog isolated stimulator (ASI Model 2220, A-M Systems, Carlsborg, WA) was used to deliver stimulation between each prototype electrode and a subcutaneous 23 gauge needle at 0.5 Hz across a range of stimulus amplitudes between 0 and 5 mA. Stimulus waveforms were current-regulated, symmetric pulses with a cathodic (500 μs) primary phase followed by a symmetric anodic (500 μs) phase. The pulses were controlled with a high-speed digital-to-analog converter using the MATLAB Data Acquisition toolbox (Mathworks).

We measured the in vivo stimulation efficiency of each design by activating the posterior IC and recording evoked electromyographic (EMG) responses in the contralateral jaw muscles. Low-noise voltage preamplifiers (Model SR560, Stanford Research Systems, Sunnyvale, CA, USA) were used to record the applied current by measuring the voltage across a 100 Ω series resistor and the applied voltage by measuring the voltage across the stimulating electrode and a Ag/AgCl reference electrode (Model

RE-4, BAS Inc., West Lafayette, IN, USA). Power efficiency was quantified by fitting the Hill equation (Equation 3.3) to the integral of the rectified EMG response as a function of the peak power, where f is a fraction of the maximum response, P is the stimulation power, P_{50} is the power needed to evoke a half maximal response, and n is the Hill-fitting coefficient. The fitted expression was used to calculate the P_{50} for each electrode.

$$f = \frac{P^n}{P_{50}^n + P^n} \tag{3.3}$$

3.2.5 Sensitivity Analyses

Evoking an EMG response in the contralateral jaw muscles required a current-regulated waveform with a 500 μs cathodic phase followed by a 500 μs anodic phase, so to be consistent, we used the same waveforms in our modeling and in vitro analysis. However, in DBS, typical pulse widths are between 60-210 μs [26], and waveforms can be either voltage-regulated or current-regulated. To address the effects of a smaller PW and the choice of a voltage-regulated waveform on the model results, we modeled the filtering effects of the ETI and conducted subsequent simulations at PWs of 100 μs and 500 μs.

We approximated the filtering effects of the ETI using the static model (i.e., with no ETI) to solve for the potential distribution in space and the Randles circuit to solve for the decay of potentials over time [81]. For each electrode, R_a was set to the static model value, and the C_{dl} and R_f were set to the average values measured in vitro. The effects of the ETI on efficiency were quantified by determining the relative change in power efficiencies, compared to the static case, across the six combinations of Rook designs and the six combinations of Serp designs.

3.2.6 Statistical Analysis of Data

Data are presented as the mean ± standard error across five experiments, and all statistical tests were performed at a 95 % confidence level (i.e., $\alpha < 0.05$). Circuit element values from the model fitting were first analyzed with a repeated measures analysis of variance (ANOVA) to test the (null) hypothesis that all values came from the same distribution. A repeated measures approach was necessary because multiple electrode designs were tested per experiment. If the null hypothesis was rejected, post-hoc comparisons were made using a protected Fisher's least significant difference test.

Equation 3.3 was fit to the experimental data used to construct input-output curves of power vs. the integral of the rectified EMG, and a repeated measures ANOVA was conducted on the P_{50} values to assess if the effect of electrode design was significant ($\alpha < 0.05$). If the effect of lead design was significant, post hoc t-tests were run to compare the relative power performance of the tested electrode designs versus the control.

3.3 Results

We coupled potentials calculated with FEM models of eight prototype electrode designs with varying areas and perimeters to cable models of passing axons to quantify the effect of electrode geometry on DBS stimulation efficiency. Next, we conducted in vitro pulse transient analysis and quantified the electrical properties of the prototype electrodes by fitting the measured response to a three-element Randles equivalent circuit. Finally, we measured in vivo the stimulation efficiency of select designs following acute implantation in the posterior internal capsule of anesthetized cats.

3.3.1 Model-based analysis of high-perimeter electrode designs

3.3.1.1 Effects of electrode geometry on access resistance

The FEM models were used to calculate R_a of each electrode design (Table 1). Increasing the perimeter of an electrode with a fixed area decreased R_a, but altering the surface area of the electrode had a greater effect on R_a than altering its perimeter. For example, the perimeter of R1 was 400 % greater than the perimeter of R4, and as a result, the R_a of the former was 10 % less than the R_a of the latter (Table 1). Yet, all electrodes with smaller surface areas (R1, R4, S1, and S3) had larger R_a than electrodes with large areas (R2, R3, S2, and S4).

Table 3.1: The theoretical access resistance (R_a) of the electrode designs

Electrode	Area (mm^2) $A = 1.905\pi$	Perimeter (mm) $P = 2.540\pi$	Access Resistance (Ω)	Relative ΔR_a[b] (%)
Rook 1	2A/3	4P	672	-10
Rook 2	A	2P	598	-19
Rook 3	A	2P	573	-23
Rook 4[a]	**2A/3**	**P**	**742**	**0**
Serp 1	2A/3	6P	637	5
Serp 2	A	3P	569	-6
Serp 3	2A/3	2P	686	13
Serp 4[a]	**A**	**P**	**608**	**0**

[a] Bolded are the respective controls for the rook and serpentine electrodes
[b] Relative change in R_a versus respective control

3.3.1.2 Effects of electrode geometry on the power efficiency of stimulation

In electrode pairs where the former electrode had an equal area and greater perimeter than the latter (e.g., S1 vs. S3, S2 vs. S4, and R1 vs. R4), less power was required to activate axons oriented perpendicular to the electrode axis and (approximately) the 50 furthest axons oriented parallel to the electrode axis, but more

power was required to activate the 50 closest axons oriented parallel to the electrode axis. Similar results were obtained in electrode pairs where the former had a greater area and perimeter than the latter (e.g., S2 vs. S3 and R3 vs. R4). Further, in the electrode pair where the former and latter had an equal area and perimeter, but different maximum edge-to-edge length (i.e., R2 vs. R3); relative power efficiency also depended on the distance and orientation of the axons. These relationships are summarized in Figure 3.3.

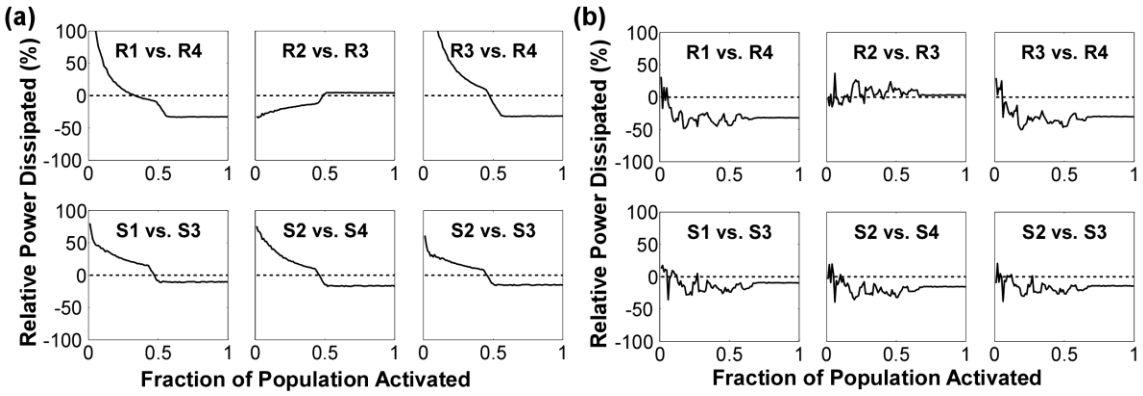

Figure 3.3: The relative power efficiency between six pairs of Rook and Serp designs.
(a) The relative percent power consumed when stimulating parallel model axons versus the fraction of the population activated. Positive values indicate more power consumption and less efficiency, while negative values indicate the opposite. (b) The same format as in (a), except for perpendicular model axons.

3.3.1.3 Shape of potential distribution impacts stimulation efficiency

We examined $\delta^2\Phi$ to quantify the dependence of stimulation efficiency on the orientation of the axons. In electrode pairs with equal areas (e.g., R1 vs. R4, R3 vs. R2, S1 vs. S3, and S2 vs. S4), the maximum $\delta^2\Phi$ parallel to the electrode axis was smaller in the former electrodes, which had the greater maximum edge-to-edge length or effective height (h_{eff}) (Figure 3.4). In these same electrode pairs, the maximum $\delta^2\Phi$ perpendicular

to the electrode axis was larger in the electrodes with the greater h_{eff}. The dependence of $\delta^2\Phi$ on h_{eff}, however, was only observed in approximately the 50 closest axons, which were ~ 2 mm from the electrode surface. At distances greater than 2 mm, the magnitude of $\delta^2\Phi$ was greatest for electrodes with the smallest R_a. Therefore, close to the electrode, electrode geometry had an orientation-dependent effect on the shape of $\delta^2\Phi$ that markedly influenced stimulation efficiency; and further away, efficiency was better predicted by R_a.

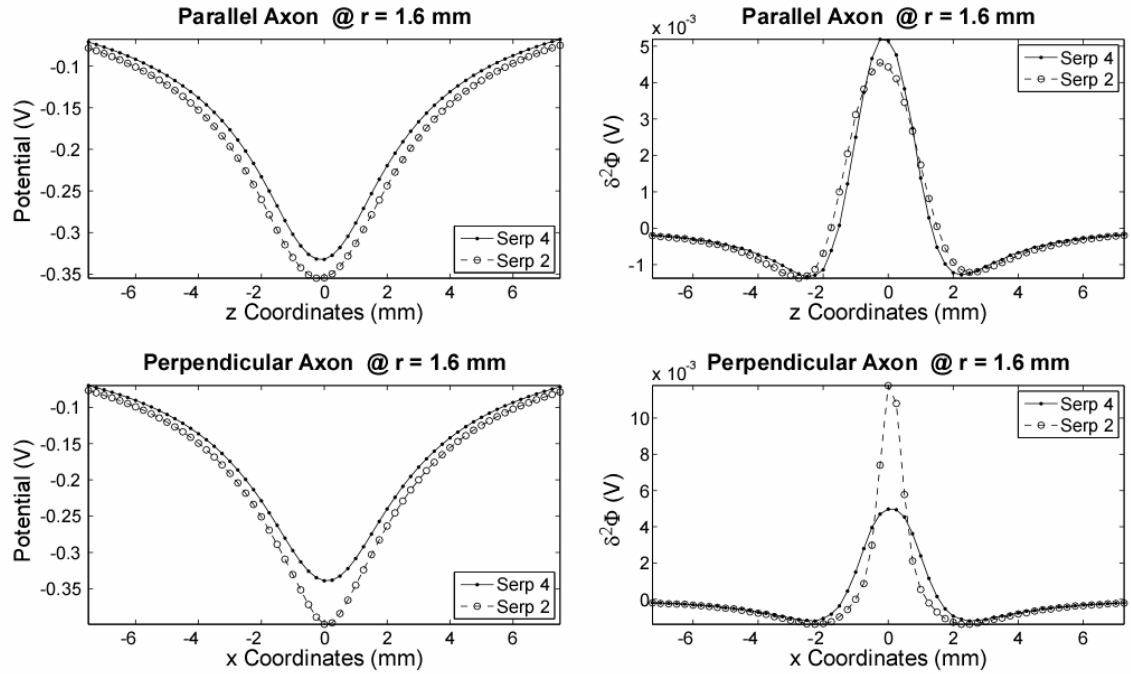

Figure 3.4: An example of the effect of electrode geometry on the shape of the potentials and their centered second difference ($\delta^2\Phi$) at an applied stimulus voltage of -1 V.
Top figures, the potentials (left) and their respective $\delta^2\Phi$ (right) generated by S2 (open circles) and S4 (solid dots) at the nodes of a parallel axon 1.6 mm away from the electrode. Bottom figures, the potentials (left) and their respective $\delta^2\Phi$ (right) generated by S2 (open circles) and S4 (solid dots) at the nodes of a perpendicular axon 1.6 mm away from the electrode.

3.3.2 Electrical properties of high-perimeter electrode designs measured in vitro

3.3.2.1 Three-element Randles circuit is an appropriate model

Electrochemical impedance spectroscopy was used to characterize the electrical properties of prototype electrodes in vitro. The measured impedance consisted of an electrode-electrolyte impedance, including a Faradaic resistance in parallel with a double-layer capacitance, and an access (electrolyte) resistance (Figure 3.5a). The real and imaginary components of the total impedance formed a partial semicircle for frequencies between 100 Hz and 10 kHz (Figure 3.5b), which was well fit with a Randles circuit [93]. Below 100 Hz, the impedance diverged from a semicircle (Figure 3.5b), indicating diffusion limited transport of electrochemical species [93]. Since greater than 96% of the power in a standard DBS pulse (500 μs or less) is contained in the frequency band above 100 Hz [82], the Randles circuit is an appropriate model.

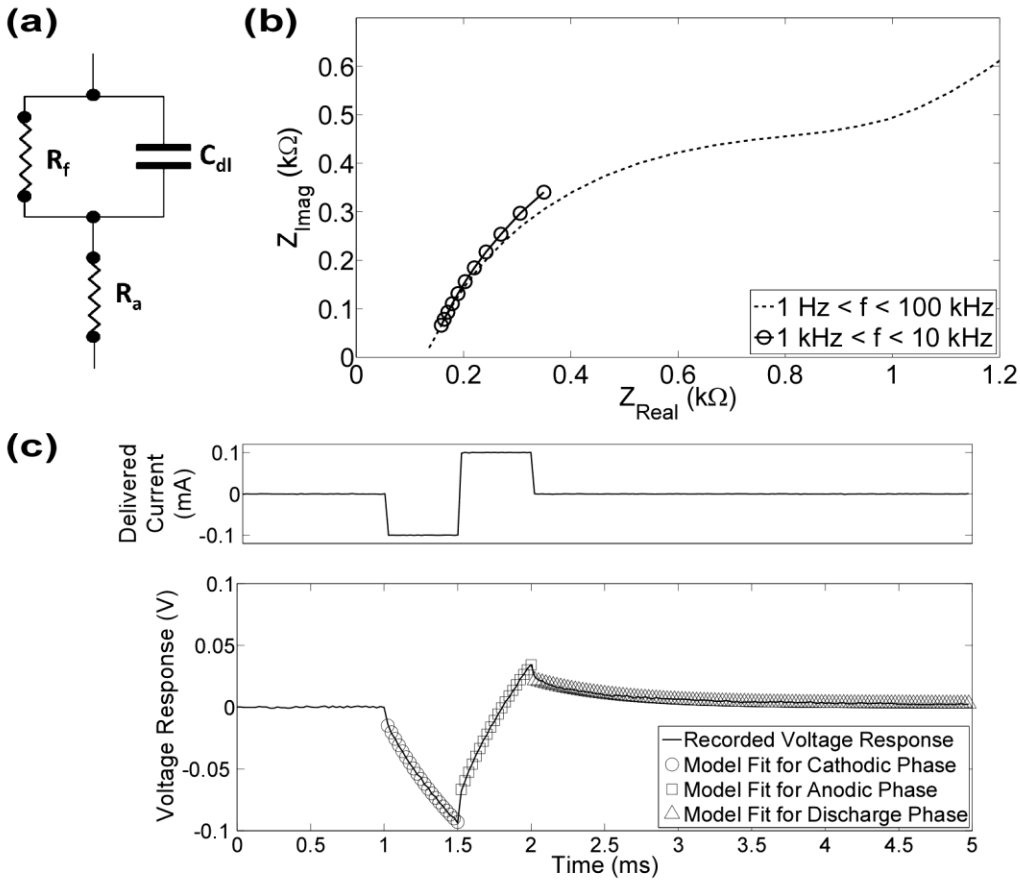

Figure 3.5: In vitro measurements characterizing the electrical properties of the prototype electrodes.
(a) The Randles circuit included the parallel combination of a Faradaic resistance and double-layer capacitance in series with an access (electrolyte or tissue) resistance. (b) In vitro impedance spectrums of serpentine electrode 4 (S4) calculated for frequencies between 1 kHz and 10 kHz (solid line + open circles), and 1 Hz and 100 kHz (dashed line). (c) Example of a voltage transient (bottom) in response to a current regulated biphasic square pulse (top). The analytical expression for a Randles circuit voltage transient was fit to each of the three phases of the voltage transient.

3.3.2.2 Randles circuit values of electrode designs

The equivalent circuit parameters (R_a, R_f, C_{dl}) for each electrode design were determined by fitting Equation 3.1 to each phase of the voltage transients measured in vitro (Figure 3.5c), and a repeated-measures ANOVA ($\alpha < 0.05$) was performed on the circuit parameters of the first phase to assess the effect of electrode geometry on the

circuit values (Figure 3.6). For both serpentine and rook electrodes, there was a significant effect of electrode geometry that depended on the current amplitude, and this effect was present for all circuit parameters. Post-hoc t tests were performed to compare the values of the circuit elements between the individual electrodes.

Across all current amplitudes, electrodes with larger surface areas (R2, R3, S2, and S4) had significantly smaller R_a and larger C_{dl} than electrodes with smaller surface areas (R1, R4, S1, and S3), except at 1 mA, where C_{dl} of R1 and R3, and S3 and S4 were not significantly different. For rook electrodes, R_f was insensitive to changes in electrode area over the range of values tested, but for serpentine electrode, R_f depended on the surface area of the electrode. Unlike area, the effect of perimeter was not as consistent. As predicted by the FEM models, in electrodes pairs with equal area and unequal perimeter (e.g., R1 vs. R4 and S2 vs. S4), the electrodes with a greater perimeter had a significantly smaller R_a. However, unlike the models' predictions, R2 and R3, which had the same area and perimeter, did not have significantly different R_a; and between S1 and S3, S1, despite having a larger perimeter, had a significantly greater R_a. In most cases, R_f and C_{dl} of electrodes with equal area but different perimeter were not significantly different.

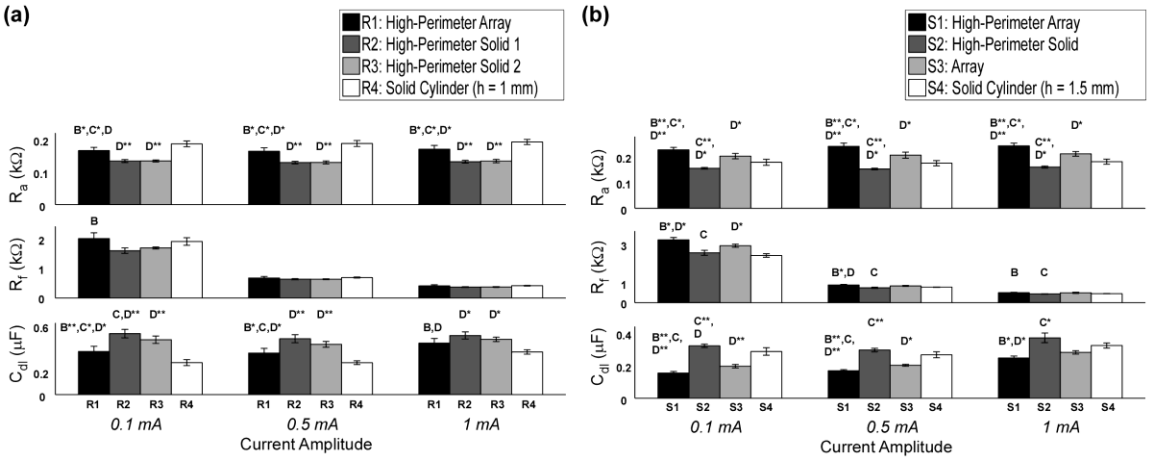

Figure 3.6: The electrical properties of the electrode-tissue interface measured in vivo. Randles circuit element values (R_a, R_f, and C_{dl}) calculated from model fitting to voltage transients recorded in vitro for (a) Rook and (b) Serpentine electrode designs. B, C, and D denote a statistical difference ($\alpha < 0.05$) with electrode numbers 2, 3, and 4, respectively. No asterisk denotes a p value of $0.01 \leq p < 0.05$; one asterisk denotes $p < 0.01$; and two asterisks denote $p < 0.001$.

3.3.3 Power efficiency of electrode designs measured in vivo

Since altering electrode area has a greater effect than altering electrode perimeter, we only tested two sets of electrode pairs with different areas in vivo: R3 vs. R4 and S3 vs. S4. Input-output curves of power dissipated versus the integral of the rectified EMG were constructed for the four electrodes (Figure 3.7), and the efficiency of stimulation was quantified by calculating the peak power required to evoke a half-maximal response, P_{50}. R3 consumed significantly (8 ± 3 %, p = 0.029) less power than R4, and S3 consumed significantly (21 ± 5 %, p = 0.009) more power than S4.

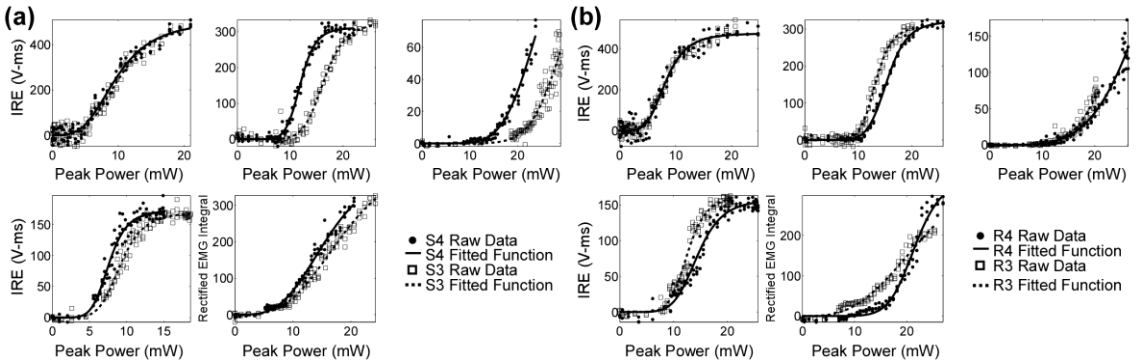

Figure 3.7: Input-output curves of peak power to stimulate the posterior internal capsule vs. the integral of the rectified EMG (IRE) of the contralateral jaw muscle.
Raw data and fitted sigmoid functions from 5 separate experiments comparing the efficiency of (a) S3 to S4 and (b) R3 to R4. S3 consumed more power than S4 in eliciting a half-maximal response, while R3 consumed less power than R4.

3.3.4 Impact of electrode tissue interface on model predictions

For current-regulated waveforms with PWs of 100 μs and 500 μs, the relative efficiencies of the 12 electrode pairs differed by 0.0021-3.9 % and 0.013-4.8 %, respectively, compared to the static case. In 11 of the 12 of the electrode pairs, electrodes that were more (less) efficient in the static case remained more (less) efficient when the filtering effect of the ETI was added.

During voltage-regulated stimulation, the effects of the ETI were more pronounced. With PWs of 100 μs and 500 μs, the relative efficiencies of the 12 electrodes pairs in the ETI case differed by 0.092-3.4 % and 0.029-25 %, respectively, compared to the static case. The large changes observed with a PW of 500 μs had the effect of reversing the trends predicted by the static model in 7 of the 12 electrode pairs. Therefore, electrodes that were more (less) efficient in the static case were less (more) efficient in the ETI case.

3.4 Discussion

The goal of this study was to determine how changes in electrode area and perimeter affected the efficiency of stimulation. The results yielded three important conclusions for designing more power efficient stimulation electrodes. First, the electrode access resistance can be reduced by increasing electrode area and/or perimeter, but the effect of increasing perimeter is not as pronounced as increasing area. Second, efficiency is dependent on the distribution of potentials in the tissue, so electrode (access or dynamic) resistance alone cannot be used to predict accurately the stimulation efficiency. And third, because the electrode-tissue interface (ETI) impedance is of the same order of magnitude as the access resistance and dependent on electrode geometry, the ETI impedance has a marked effect on stimulation efficiency.

3.4.1 Decreasing the access resistance of an electrode

Our modeling results demonstrate that R_a can be decreased by increasing the electrode area and/or perimeter. Increasing area by 50 % decreased R_a by as much as 23 %, while increasing perimeter by 400 % decreased R_a by only ~10 %. Therefore, increasing area had a much more prominent effect in decreasing R_a than increasing perimeter. These predictions were confirmed in vitro (Figure 3.6), with the exception of one case, S1 versus S3. S1 had a perimeter three times that of S3, and the model predicted that R_a of S1 would be less than R_a of S3. However, the in vitro measurements showed the opposite result (Figure 3.6b). Inspection of S1 under a microscope revealed that the surface of S1 was corroded (oxidized) at the tips of the serpentine edges, where

the current density is highest [75]. A reduction in the surface area of S1 not only explained the unexpected result, but it also showed that high-perimeter designs with high-curvature edges (e.g., S1 and S2) may be more prone to electrochemical reactions that damage the electrode surface.

3.4.2 The effects of altering electrode geometry on the efficiency of neural stimulation

Increasing the perimeter of a cylindrical electrode with a fixed area and radius requires increasing its maximum edge-to-edge length, or h_{eff}. A cylindrical electrode whose height (h) is greater than its diameter (d) generates a potential distribution that is more uniform parallel to its axis than perpendicular to its axis, which reduces $\delta^2\Phi$ parallel to the electrode axis, so a long electrode (h or h_{eff} > d), despite having a smaller R_a, is expected to be less efficient than a short electrode in stimulating neural elements oriented parallel to the electrode axis.

Increasing h also brings the electrode surface closer to neural elements that are displaced longitudinally along the insulating shaft. The stimulation threshold for activating a neural element is inversely related to its distance from the electrode, so longer electrodes, because of their increased proximity to the targeted perpendicular elements, are expected to be more efficient than shorter electrodes in stimulation of perpendicular neural elements. This explains why the high-perimeter designs (e.g., R3 and S2), compared to banded designs with greater R_a (e.g., R4 and S3), were less

efficient in activating the closest axons oriented parallel to the electrode (Figure 3.3a) but more efficient in activating the closest axons oriented perpendicular to the electrode (Figure 3.3b). The orientation-dependent effects of electrode geometry on $\delta^2\Phi$ diminished with distance, so the efficiency of stimulating the furthest axons was best explained by a reduction in R_a.

3.4.3 The impact of the electrode tissue interface on the efficiency of neural stimulation

The area and perimeter of the electrode affected not only R_a but also C_{dl} (Figure 3.6). Because C_{dl} affects the rate at which the ETI charges, and because the extent to which the ETI charges depends both on the choice of PW and whether the waveform is voltage-regulated or current-regulated, sensitivity analyses were conducted to assess the impact of the ETI on our results. The model predictions were still valid for current-regulated waveforms with PWs of 100 μs and 500 μs, as well as voltage-regulated waveforms with a PW of 100 μs; but when using voltage-regulated waveforms with a PW of 500 μs, the presence of the ETI altered the model predictions in 7 of the 12 electrode pairs.

As the ETI charges during current-regulated stimulation, the applied current is kept constant by increasing the applied voltage over time (Equation 3.1). Because the applied current is constant, the magnitude of the potentials in the tissue is also constant, preserving any effects of electrode geometry on $\delta^2\Phi$ (Figure 3.4). Thus, during current-regulated stimulation, differences in the relative power efficiency between two electrodes

over time arise from differences between their applied voltages. Recall from Equations 3.1 and 3.2, the applied voltage increases at a rate that is inversely proportional to both C_{dl} and R_f. Indeed, altering the area and perimeter had a significant effect on altering C_{dl} (Figure 3.6), which led to differences in the applied voltage over time between electrodes with different C_{dl} (e.g., S1 vs. S2). However, for $t \leq 500$ μs, the differences in the applied voltage over time were small enough that relative power efficiencies between electrode pairs with different C_{dl} changed by < 5 %.

During voltage-regulated stimulation, the applied voltage is held constant, and as the ETI charges, the applied current decreases over time. Equations 3.4 and 2.9 describe the applied current (I_{vr}) in an equivalent Randles circuit in response to a constant applied voltage (V_o).

$$I_{vr} = \frac{V_o}{R_a + R_f}\left(\frac{R_f}{R_a}\exp\left(\frac{-t}{\tau_{vr}}\right)+1\right) \tag{3.4}$$

$$\tau_{vr} = \frac{C_{dl}R_f R_a}{R_a + R_f} \tag{3.5}$$

Increasing the area and/or perimeter of the electrode increases C_{dl} and reduces R_a (Figure 3.6), which have competing effects in altering τ_{vr} (Equation 2.9). Because R_a and R_f are typically on the same order of magnitude in brain tissue [80], τ_{vr} is more sensitive to changes in C_{dl} than R_a and R_f, and the overall effect of increasing area and/or perimeter is

an increase in τ_{vr}. Therefore, between a pair of electrodes with different τ_{vr}, the power efficiency of the electrode with the larger τ_{vr} will increase over time with respective to the power efficiency of the electrode with the smaller τ_{vr} because the magnitude of the potentials generated by the former decay less rapidly over time than the potentials generated by the latter.

The difference in the rate of decay of I_{vr} between electrodes with different C_{dl} explains why in seven electrode pairs (i.e., R3 vs. R1, R3 vs. R2, R3 vs. R4, S2 vs. S1, S1 vs. S3, S2 vs. S3, and S2 vs. S4), where the former has a larger C_{dl} and longer h_{eff} than the latter, the relative efficiency between the two was dependent on PW. Consider, for example, S2 and S4. S2 had a greater C_{dl} than S4, so as the ETI charged, I_{vr} of S2 declined more slowly over time than I_{vr} of S4. At t = 100 μs, the difference in I_{vr} between S2 and S4 was not large enough to impact markedly the effect of electrode geometry on $\delta^2\Phi$ (Figure 3.4), so like the static case, S2 was less efficient than S4 in activating axons parallel to the electrode. However, at t = 500 μs, I_{vr} of S4 had declined far enough below I_{vr} of S2 that unlike the static case, S2 was more efficient than S4 in activating parallel axons.

3.4.4 Limitations

The methodology in this study made use of a linear representation of the ETI to study the effects of electrode geometry on R_f and C_{dl}. Because R_f and C_{dl} vary nonlinearly with the applied potential, simplification of the ETI requires consideration. The nonlinear dependence of R_f and C_{dl} on the applied potentials is described by The

Butler-Volmer and Gouy-Chapman-Stern models, respectively [93]. For typical stimulation parameters used in DBS, R_f and C_{dl} vary slowly enough in time that they can be approximated as constant during each phase of the pulse [80, 81]. In other words, one can approximate the nonlinear ETI using a piecewise linear representation, where R_f and C_{dl} during each phase are chosen by evaluating their respective nonlinear expressions at the beginning of each phase.

A piecewise linear model of an equivalent Randles circuit was indeed accurate in describing the filtering effects of the nonlinear ETI both in vitro (Figure 3.5c) and in vivo (data not shown). However, it is not always valid to use an equivalent circuit model to describe the effects of the ETI, as this assumes the current density ($\vec{J}$) is uniform throughout the conducting volume. Not only is $\vec{J}$ highly non-uniform on the electrode surface, but the non-uniformity of $\vec{J}$ depends on electrode geometry [37]. Further, heterogeneities in the tissue conductivity, such as cerebral-spinal fluid filled spaces [100] and encapsulation tissue [77], can alter $\vec{J}$ in the bulk tissue. In cases where $\vec{J}$ is highly non-uniform, the charging of the ETI cannot be described with a single τ [101]. Thus, future studies looking at the impact of the ETI on the stimulation efficiency of electrodes should consider explicit representation of the ETI.

3.4.5 Designing the next generation of deep brain stimulation electrodes

The future objective is to design electrode geometries that are optimal for stimulating white or grey matter regions of the brain so that electrodes used in DBS are better suited to their intended anatomical target. For example, tracts of myelinated axons

within white matter regions are the primary targets in treating psychiatric disorders, such as obsessive-compulsive disorder and depression [6, 117]; and axon afferents within select brain nuclei of grey matter regions are the primary targets for treating movement disorders, including essential tremor [118] and Parkinson's disease [57]. Our results highlight three important considerations for designing future DBS electrodes.

(1) Area has a greater effect than perimeter on altering the electrical properties of the electrode and thereby impacting stimulation efficiency. Previous studies have proposed increasing efficiency by using electrode arrays to increase perimeter [36, 37] or by changing the dimensions of the cylindrical electrode contact to increase area [90]. Since our modeling and experimental results support the latter, we recommend increasing efficiency by altering the height and/or diameter of the cylindrical electrode.

(2) Stimulation efficiency depends not only on the (access and dynamic) resistance of the electrode but also on the shape of the potential distribution. High-perimeter designs, which had a greater effective height than a corresponding banded electrode with equal area, were more efficient at activating neural elements perpendicular to the electrode but less efficient at activating elements parallel to the electrode, despite decreases in R_a. Therefore, in therapies like DBS for the treatment of obsessive-compulsive disorder, where the target thalamocortical fibers connecting the mediodorsal thalamus to the prefrontal cortex [119] are perpendicular to the implanted electrode shaft, performance can be increased by increasing the height of the cylindrical electrodes.

(3) Electrode geometry has a marked impact on the filtering effects of the ETI. Pulse widths commonly used in DBS are between 60 – 210 μs [26]. Within this time

window, the filtering effects of the ETI have a marked impact on the applied waveform [80], as well as the stimulation thresholds [78], so we recommend that model-based design of stimulation electrodes consider the filtering effects of the ETI.

3.5 Conclusion

We theoretically and experimentally assessed the power efficiency of eight prototype electrode designs with varying areas and perimeters. The results of this analysis yielded three important conclusions. First, the electrode access resistance can be reduced by increasing electrode area and/or perimeter, but the effect of increasing perimeter is not as pronounced as increasing area. Second, efficiency is dependent on the distribution of potentials in the tissue, so electrode (access or dynamic) resistance alone cannot be used to predict accurately the stimulation efficiency. And third, because the impedance of the ETI is of the same order of magnitude as the access resistance and dependent on electrode geometry, it has a marked effect on stimulation efficiency. These results advance understanding of the features of electrode geometry that are important for designing the next generation of efficient DBS electrodes.

Chapter 4 : Design and In Vivo Evaluation of Optimal Deep Brain Stimulation Electrodes

4.1 Introduction

Deep brain stimulation (DBS) is an established therapy for neurological disorders, wherein 100-200 Hz electrical pulses are delivered to specific regions of the brain. DBS is effective in treating movement disorders, including Parkinson's disease and essential tremor [1, 2], and it shows promise for treating epilepsy and psychiatric disorders [5, 6]. Despite the clinical success of DBS, several aspects of the therapy require further development, particularly the efficiency of stimulation.

Implanted pulse generators (IPG) used for DBS have battery lifetimes of 3-5 years [107]. Because the battery life of the IPG is much less than the required duration of treatment, patients receiving DBS require repeated IPG replacement surgeries that obligate them to incur repeatedly the risks associated with surgery, including infection [22, 23] and misprogramming [24]. IPGs with rechargeable batteries (RPGs) are an alternative to primary cells: they have longer predicted lifetimes but are more costly, need to be recharged on a regular basis, and are not well accepted [109]. Since RPGs are not a panacea for limited device lifetimes, efficiency needs to be improved. Stimulation efficiency may be improved by modifying the stimulation waveform [120-122], the material properties of the electrode [35, 67], and/or the geometry of the electrode [37, 38].

Altering the properties of the electrode can increase stimulation efficiency by decreasing the load or impedance of the electrode (Z_e), which, in general, consists of the impedance of the electrode-tissue interface (ETI), including the parallel combination of the double-layer capacitance (C_{dl}) and Faradaic resistance (R_f), in series with the lumped or access resistance of the tissue (R_a). Because an electrode with a smaller Z_e releases more current per volt, a smaller applied voltage is required to generate a current in the tissue that is large enough to activate the target neural elements. Techniques to reduce Z_e include surface roughening [33], electrode coatings [35], or increasing the area and/or perimeter of the electrode [37, 38, 123].

The selectivity of DBS, i.e., the ability to activate target neural elements over non-target elements, also requires improvement, as suboptimal lead placement is a common failure mode [20, 24, 25]. Lead deviations of 2-3 mm can preclude some or all potential clinical benefits [20, 23-25], and in some cases, generate side-effects by stimulation of non-target regions [20]. For example, high frequency DBS of cerebellar afferents in the ventral intermediate nucleus of thalamus masks tremor-associated burst activity in essential tremor [56], but activation of these target elements is limited by activation of non-target projection neurons in the ventral caudal nucleus of thalamus, which can induce uncomfortable paresthesias [50]. Small lead misplacements can sometimes be overcome by reprogramming the stimulation parameters [26], but larger misplacements require an additional surgery to reposition the lead [25].

Altering electrode geometry can improve stimulation selectivity. For example, co-varying the height and radius of the current Model 3387/3389 clinical electrode was

predicted to alter the volume of tissue activated (VTA) for a given set of stimulation parameters [90]. In addition, high density arrays of electrodes show promise in increasing stimulation selectivity: small contacts can be used individually to target small volumes of tissue [124, 125] or combined in multipolar configurations to shape the VTA [50].

The goal of this study was to design electrodes that increase the efficiency and selectivity of DBS. We coupled a finite element method (FEM) model of a cylindrical electrode array in brain tissue with cable models of neural elements and engineering optimization to design electrode configurations (i.e., geometries and polarities) that increased the efficiency and selectivity of DBS. Subsequently, prototype electrodes were tested in vivo. Electrodes with greater stimulation efficiency will increase the lifetime of battery-powered IPGs and increase the recharge intervals of RPGs, and electrodes with greater stimulation selectivity may reduce the sensitivity of clinical outcomes to malpositioning of the electrode and thereby reduce side effects. Preliminary results of this study were presented in a conference paper [126].

4.2 Methods

4.2.1 Computational model of DBS

We constructed an FEM model in COMSOL Multiphysics v3.4 (COMSOL Inc., Burlington, MA) consisting of a three-contact cylindrical electrode array surrounded by a cubic (60 mm x 60 mm x 60 mm) volume of brain tissue (0.2 S/m, [40]) (Figure 4.1a). A 0.5 mm thick layer of tissue immediately surrounding the electrode represented the glial

scar (0.1 S/m [127]), and the electrical conductivities of the encapsulation and brain tissue were homogeneous, isotropic and purely resistive [82].

A normal current density of 0 A/mm^2 (i.e., a Neumann boundary condition) was imposed on the electrode shaft to model a perfect insulator. Fixed potentials of X V (i.e., Dirichlet boundary conditions), where - 10 < X < 10, were imposed individually on the three contacts, and 0 V was imposed on the outer tissue boundary. The electric potentials were calculated by solving Laplace's Equation (Equation 2.1), and the injected current was calculated by integrating the current density over the surface of the electrode (Equation 2.2).

We used the NEURON simulation environment (v7.1) [84] to implement cable models of neural elements, including myelinated axons of passage (AOP) [102], terminating axons (TA), and local neurons (LN) [70]. AOP, TA, and the axons of the LN were 2.5 μm in diameter and 40 mm in length. Populations consisted of 100 elements with axons oriented parallel (z direction) and perpendicular (x direction) to the electrode shaft (Figure 4.1b). Based on defined reference points – which were the middle node of Ranvier, the axon terminal, and the center of the soma for AOP, TA, and LN, respectively – the two halves of the population were uniformly distributed in two rectangular prisms displaced by ± 1.135 mm on either side of the z = 0 plane (Figure 4.1b). Displacement of the rectangular prisms ensured that no neural elements intersected the electrode or encapsulation tissue, and the dimensions of the rectangular prisms were chosen such that elements were distributed < ρ_{seed} from the origin, where ρ_{seed} was 2.5, 5, or 10 mm.

The source driving polarization of the neural membrane is proportional to the spatial centered second difference of the potentials, $\delta^2\Phi$ [39], so the potentials were calculated using ~ 1 million 3rd order Lagrangian elements, as this prevented large discontinuities when calculating $\delta^2\Phi$ [81]. Refinement of the FEM mesh (i.e., splitting elements into smaller elements) from ~320,000 to 1 million cubic elements resulted in changes of < 1 % in the mean absolute relative difference of both the interpolated potentials and corresponding stimulation thresholds of coupled neural elements.

The interpolated potentials were used in NEURON to stimulate the neural elements with a 100 μs monophasic rectangular pulse. Since the conductivities were linear, the potentials at a specific stimulation voltage were calculated by multiplying the 1V solutions by a scalar, and the threshold stimulation voltage to activate each model axon was calculated using a bisection algorithm (relative error < 1 %).

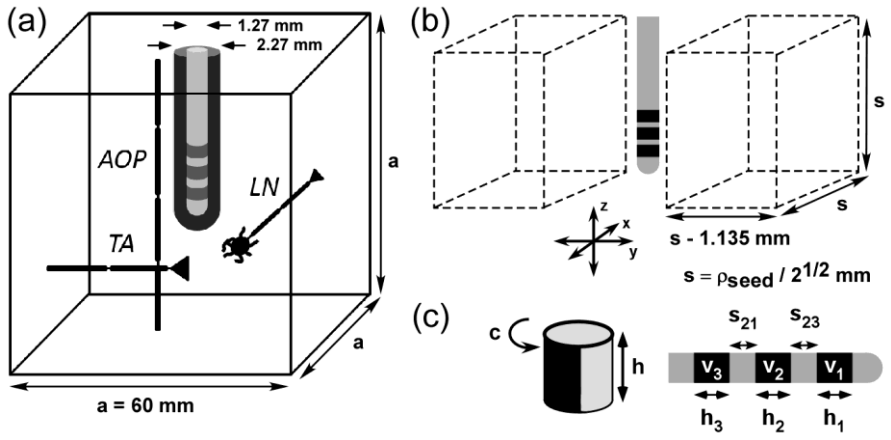

Figure 4.1: A computational model for design and analysis of deep brain stimulation (DBS) electrodes.
(a) An FEM model of an electrode array surrounded by encapsulation tissue (0.1 S/m) and brain tissue (0.2 S/m) was coupled to cable models of neural elements: AOP = axons of passage, TA = terminating axons, and LN = local neurons. (b) Neural elements were distributed in two rectangular prisms that were displaced on either side of the x-z plane. (c) The three-electrode array (right) was parameterized using eight variables: 3 electrode heights (h_1, h_2, and h_3), 2 interelectrode spacings (s_{21} and s_{23}), and 3 applied potentials (v_1, v_2, and v_3). In monopolar stimulation (left), electrodes 1 and 3 were modeled as insulating boundaries, and electrode 2 was parameterized by its height, h, and normalized circumference, c.

4.2.2 Design of optimally efficient and selective electrodes

The computational model of DBS was used with engineering optimization to design electrode geometries that could either efficiently activate AOP, TA, and LN; selectively activate parallel AOP over perpendicular AOP; or selectively activate parallel TA over AOP. The three-electrode array was parameterized using eight variables: three electrode heights (h_1, h_2, and h_3), three applied potentials (v_1, v_2, and v_3), two inter-electrode spacings (s_{21} and s_{23}) (Figure 1c). In cases where a single electrode was more efficient or selective than stimulation with three independent electrodes (e.g., when s_{21} and $s_{23} << h_1$, h_2, and h_3), electrodes 1 and 3 were removed by treating them as insulating boundaries, and electrode 2 was parameterized by its height (h) and normalized

circumference (c) (Figure 1c). We limited ourselves to the following parameter space: s_{21}, s_{23}, h_1, h_2, $h_3 \geq 0.1$ mm and $-10 < v_1, v_2, v_3 < +10$.

For each electrode configuration (i.e., geometry and polarity), we calculated the electric potentials and subsequently, the cost functions quantifying efficiency or selectivity. The cost function for stimulation efficiency was the average power required to activate 50 % of the population of neural elements (P_{50}):

$$P_{50} = PW^{-1} \int_0^{PW} \frac{V^2(t)}{R_a} dt \tag{4.1}$$

, where V (t) is the applied voltage and PW is the duration of the rectangular pulse. Selectivity was quantified by constructing a curve, p(x), of the proportion of a population of neural elements activated versus selected proportions of a population of other neural elements and minimizing or maximizing the (normalized) area under the curve:

$$AUC = 100^{-1} \int_0^{100} p(x)dx. \tag{4.2}$$

We used a Genetic Algorithm (GA) (MATLAB v2008b, Global Optimization Toolbox) to search the parameter space and optimize the cost function. The initial geometry was selected randomly within the bounds of the parameter space. Each generation consisted of 20 solutions: the 2 fittest solutions and 18 progeny, which were generated by mating (i.e., randomly swapping parameters between) nine random pairs of parent vectors. Mating was conducted by creating a random binary vector (of 0s and 1s) for each vector pair and exchanging the elements of the parent vectors where the

elements of the corresponding binary vectors were equal to 1. Mutations were introduced by adding random numbers to each element of the progeny vector. The random numbers for each element were generated from a Gaussian distribution with a mean of zero and a standard deviation equal to the difference in the parameter between the first two generations. The standard deviation of the Gaussian distribution for each parameter decreased linearly so that it reached zero at the maximum number of generations. The GA terminated when the average change in the cost function was < 0.1 % over 100 iterations, or after 150 iterations.

Optimizations were repeated ten times on three independent populations of 100 neural elements to ensure that the results were not the result of a specific population, and a post hoc brute force search was conducted on a subset of the parameter space surrounding the best GA solution to determine whether a more optimal solution existed. The selectivity and efficiency of the optimal electrode designs were compared against the Model 3387 electrode used clinically, which has a height 1.5 mm and radius of 0.635 mm.

The sensitivity of the efficient electrode designs to changes in model parameters was assessed by calculating the ratio of P_{50} of the optimal design to P_{50} of the Model 3387, termed the relative power usage (RPU), and quantifying how RPU changed in four cases: when the geometrical parameters were altered, encapsulation tissue was replaced with brain tissue, the diameter of target axons was increased, and the ETI impedance was included. For the ETI analysis, the electrical properties of the ETI were set to the minimum C_{dl} and R_f, and maximum C_{dl} and R_f values measured in vivo (see Section

3.3.1). The sensitivity of the selective electrode designs to changes in model parameters was assessed by quantifying how Equation 4.2 changed when the axons were rotated about the y axis in the xz plane. The rotation angle for each fiber was randomly sampled from a normal distribution with mean = 0 ° and standard deviation = 7.5 °.

4.2.3 Measurements of stimulation efficiency and selectivity in vivo

Two sets of prototype electrodes were fabricated to test the model-based designs (Figure 2). Prototypes were fabricated by sputter depositing a chrome adhesion layer followed by a gold metal layer onto a planar polyimide substrate, and planar substrates were wrapped around and bound to a steel shaft to form cylindrical electrode arrays. The set of electrode designs for measuring efficiency in vivo consisted of a long cylinder (LC) with a height of 6 mm and radius of 0.635 mm; a long hemi-cylinder (LHC) electrode with a height of 6 mm and radius of 0.635 mm; and an electrode with the dimensions of a Model 3387 contact. Selectivity was measured in vivo using an array of five electrodes. Each electrode had a height of 1 mm and a radius of 0.635 mm, and the inter-electrode spacing was 0.2 mm.

Acute in vivo experiments were conducted in anesthetized cats using a protocol approved by the Institutional Animal Care and Use Committee at Duke University. Anesthesia was induced with ketamine HCL (Ketaset 35 mg/kg IM, supplemented as required at 15 mg/kg during surgical preparation) and maintained with alpha chloralose (65 mg/kg IV, supplemented at 15 mg/kg). In one set of experiments, the planar electrode designs were oriented parallel or perpendicular to the cat sciatic nerve (Figure 3a), and an

isolated stimulator was used to deliver a 0.5 Hz train of voltage-regulated, asymmetric pulses with a short 100 μs cathodic phase followed by a long 900 μs anodic phase.

In a second set of experiments, brain surgery was performed under 1 % isoflurane anesthesia, and the electrode was implanted parallel or perpendicular to axons in the posterior limb of the internal capsule [115] (Figure 4.3b) – located 7 mm anterior, 10.5 mm lateral, and 10 mm above the interaural line [83, 116]. In these experiments, stimulus trains consisted of 30 voltage-regulated rectangular pulses with a short 300 μs cathodic phase followed by a long 700 μs anodic phase delivered at 350 Hz. The electrical properties (i.e., R_a, R_f, and C_{dl}) of the prototype electrodes were determined by using nonlinear regression to fit a three-element Randles equivalent circuit to the current transient (Equations 3.4 and 3.5) recorded during voltage-regulated stimulation (Figure 4.3c).

The outcome measures in the sciatic nerve and brain experiments were the voltage (V_{50}) and average power (P_{50}) required to evoke a half maximal electromyographic response (EMG) in the ipsilateral peroneus muscles or contralateral extensor digitorum muscles, respectively. EMGs were measured differentially between two 29-gauge multi-stranded stainless steel wires (Cooner Wire, Chatsworth, CA) implanted in the muscle (Figure 4.3c). EMGs were AC coupled, amplified by a gain of between 100 and 500, and bandpass filtered with lower and upper cutoff frequencies of 3 Hz and 3 kHz, respectively (SR560); and the EMG was rectified and integrated to quantify the average magnitude of the signal over time. The applied voltage was measured from the output of the isolated stimulator, the applied current was measured from the voltage drop across a

25 Ω resistor in series with the active electrode using an isolated, low noise amplifier (SR560, Stanford Research, Sunnyvale, CA), and the product of these two signals (Figure 4.3c) was used to calculate the average electrical power transferred over time. Data were sampled and stored using the MATLAB Data Acquisition toolbox (Mathworks, Natick, MA).

The location of implanted electrodes was determined from post mortem histology. Animals were perfused with 10 % formalin (~ 4 % formaldehyde). The brain was removed and immersed in a 10 % formalin (~ 4 % formaldehyde) solution for two days, immersed in a 30 % sucrose solution for one week, and frozen in optimal cutting temperature (OCT) medium at −80 °C. 30 μm thick brain slices were stained using 0.1 % cresyl violet, and electrode placement was determined by overlaying images of the stained tissue with a brain slice of the target region from a cat brain atlas (www.brainmuseum.org).

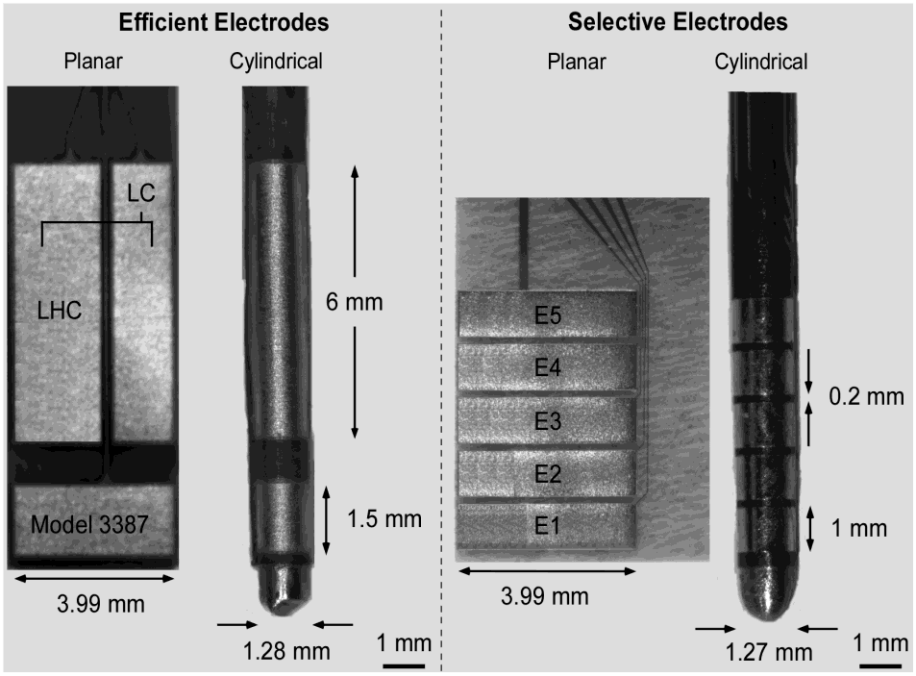

Figure 4.2: Prototype electrodes for experimental measurement of stimulation efficiency and selectivity.
Photomicrographs of two sets of planar and cylindrical electrode designs for measuring the efficiency (left) and selectivity (right) of electrical stimulation in vivo. LHC = long hemicylinder, LC = long cylinder, and E = electrode.

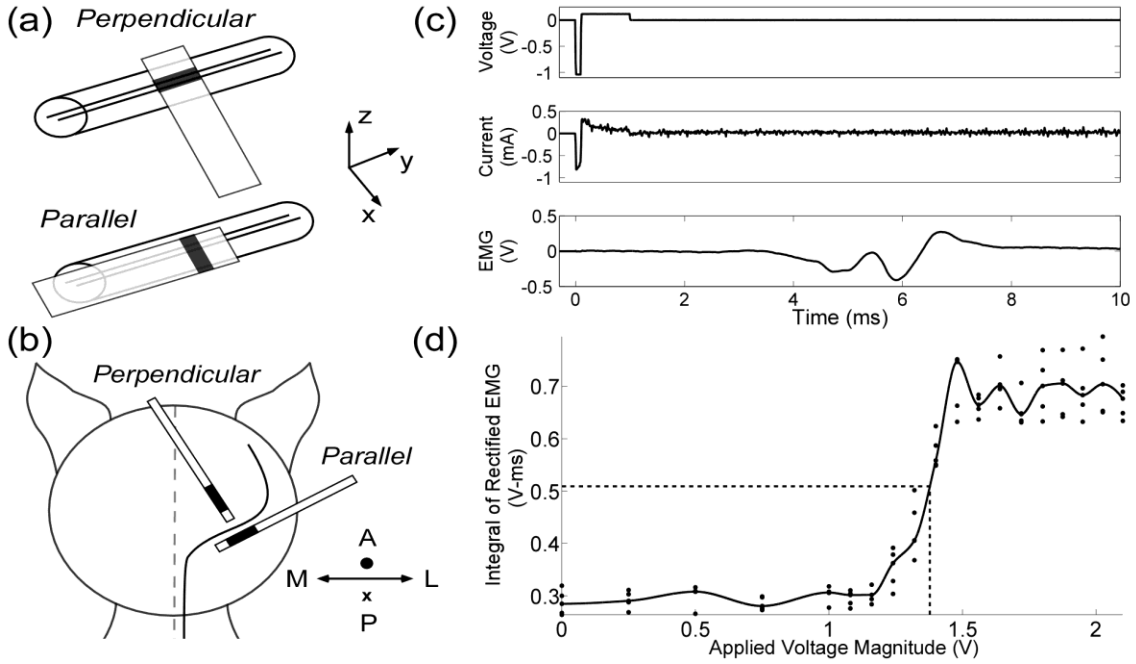

Figure 4.3: Measuring the efficiency and selectivity of prototype electrodes in vivo.
(a) Planar electrode designs (see Figure 2) were oriented parallel or perpendicular to the sciatic nerve. (b) Cylindrical electrode designs were implanted parallel or perpendicular to corticospinal axons in the posterior limb of the internal capsule. (c) The applied voltage, applied current, and evoked electromyographic (EMG) responses were recorded during stimulation. (d) The EMG was rectified and integrated, and a fitted spline was used to calculate the voltage (and average power) required to evoke a half maximal response.

4.2.4 Statistical analysis

We used a spline fitted to the EMG data to calculate V_{50}/P_{50} (Figure 3d). The dependent variable in our statistical analysis was the natural logarithm of the ratio of V_{50}/P_{50} of one electrode in one orientation to the V_{50}/P_{50} of a second (same) electrode in the same (second) orientation. Three statistical tests were conducted. First, for a given orientation and electrode design, a Lilliefors test was conducted on the distributions of $\ln(V_{50}/P_{50})$ across experiments to test the null hypothesis that $\ln(V_{50}/P_{50})$ was normally distributed. Second, if there was not enough evidence to reject the null hypothesis of the

Lilliefors test across all designs and orientations, a repeated measures analysis of variance (ANOVA) was conducted to test the hypothesis that $\ln(V_{50}/P_{50})$ across all electrodes in both orientations came from the same normal distribution. Finally, if the null hypothesis of the ANOVA was rejected, post hoc paired comparisons were made using a protected Fisher's least significant difference test. Data are presented as the mean ± standard error, and all statistical tests were conducted at a 95 % confidence level ($\alpha < 0.05$).

4.3 Results

We used a computational model of DBS and engineering optimization to design electrodes intended to increase the efficiency and selectivity of DBS. The efficiency and selectivity of the prototype electrodes were subsequently measured in vivo.

4.3.1 Computational analysis of optimally efficient electrode designs

Optimizations of the eight design parameters were conducted to determine what three-electrode configurations (i.e., geometries and polarities) minimized stimulation power (Equation 4.1) when stimulating parallel or perpendicular neural elements (AOP, TA, and LN). Optimal solutions yielded parameters sets where s_{21} and s_{23} were much smaller than h_1, h_2, and h_3; and s_{21} and s_{23} were > h_1 and h_3, and v_1 and v_3 were close to 0 V. Since these optimal solutions resembled monopolar stimulation with a single electrode, electrodes 1 and 3 were replaced with insulation, and electrode 2 was optimized with parameters c and h.

Long cylindrical electrodes were more efficient at stimulating neural elements with axons oriented parallel to the electrode shaft (Figure 4a). For example, for seeding distances (p_{seed}) of 2.5 mm, 5 mm, and 10 mm, long electrodes with h between 3.5 and 10 mm and c between 0.5 and 0.8 consumed 44-80 % less power than the Model 3387 in activating populations of perpendicular AOP, TA, and LN, respectively. In contrast, short cylindrical electrodes were more efficient for stimulating parallel neural elements. The geometry of the 3387 electrode was close to optimal for stimulating parallel AOP and TA, and altering h and c decreased power consumption by only 14 % when stimulating parallel LN (Figure 4a).

Four additional analyses were conducted to assess how sensitive the efficiency of the optimal monopolar electrode geometries were to changes in the model parameters. Since the solutions were qualitatively similar across the different neural elements, analyses were conducted only for stimulation of AOP. Increasing c from its optimal value to 1 decreased the RPU of the optimal designs by up to 2 % when stimulating parallel AOP and up to 25 % when stimulating perpendicular AOP. Increasing the conductivity of the encapsulation tissue from 0.1 S/m to 0.2 S/m (that of the brain tissue) altered the RPU of optimal designs by between −8 % and 4 %. Increasing the diameter of the AOP from 2.5 μm to 5, 7.5, 10, 12.5, or 15 μm altered the RPU of optimal designs by between −22 % and 9 %. When the ETI impedance was included in the electrode model, the RPU of the optimal designs changed by between −19 % and 6 %. These changes in RPU were comparatively small, and short and long cylindrical electrodes remained the optimal solutions for stimulating parallel and perpendicular AOP, respectively.

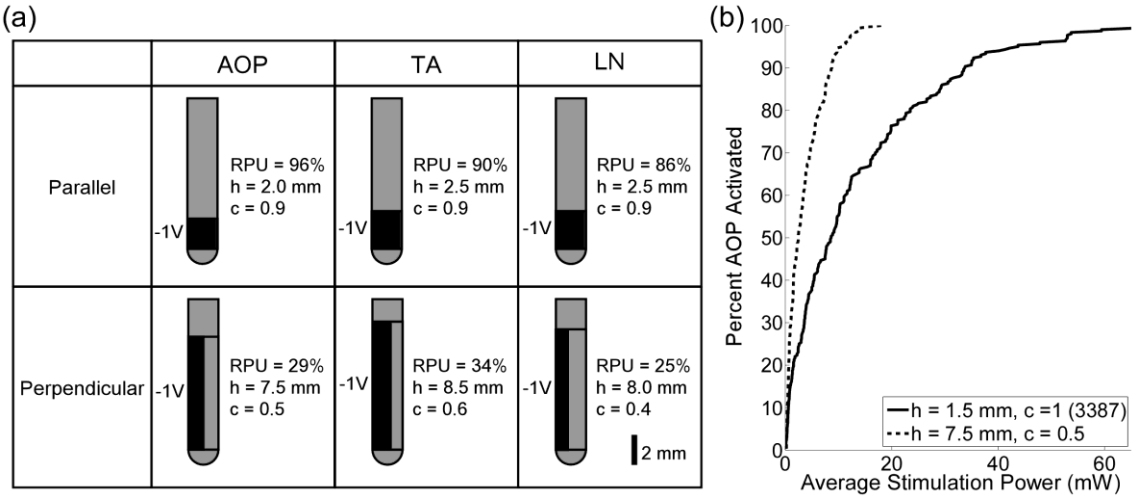

Figure 4.4: Optimal monopolar electrode geometries for efficiently activating neural elements ≤ 5 mm from the origin.
(a) Optimal geometries and corresponding relative power usage (RPU) when stimulating a population of AOP (column 1), TA (column 2), and LN (column 3) oriented either parallel (row 1) or perpendicular (row 2) to the electrode shaft. AOP = axons of passage, TA = terminating axons, and LN = local neurons. The relative power usage (RPU) is the ratio of the average stimulation power required to activate 50 % (P_{50}) of the neural elements with the optimal design to P_{50} of the Model 3387. (b) Input-output curves of average stimulation power versus percentage of perpendicular AOP activated for the solution in row 2, column 1 of (a) and the Model 3387.

4.3.2 Computational analysis of optimally selective electrode designs

4.3.2.1 Selectivity based on orientation

Optimizations of the eight design parameters were conducted to determine electrode configurations that maximized selectivity of parallel AOP over perpendicular AOP and vice versa. An asymmetric bipolar configuration was the optimal solution for selectively activating parallel AOP over perpendicular AOP (Figure 5a). When neural elements were placed up to 2.5 mm, 5 mm, and 10 mm from the origin, asymmetric

bipolar configurations activated 50 % of target parallel AOP while limiting activation of non-target perpendicular AOP to 0 %, 5 %, and 29 %, respectively, whereas the 3387 activated almost 50 % of the non-target elements (Figure 5).

The optimal configuration for selectively activating perpendicular AOP over parallel AOP was an array of cathodes. When neural elements were placed up to 2.5 mm, 5 mm, and 10 mm from the origin, an array of cathodes activated 50 % of target perpendicular AOP while limiting activation of non-target parallel AOP to 0 %, 4 %, and 5 %, respectively, whereas cathodic monopolar stimulation with the 3387 activated more than 50% of the non-target elements (Figure 5).

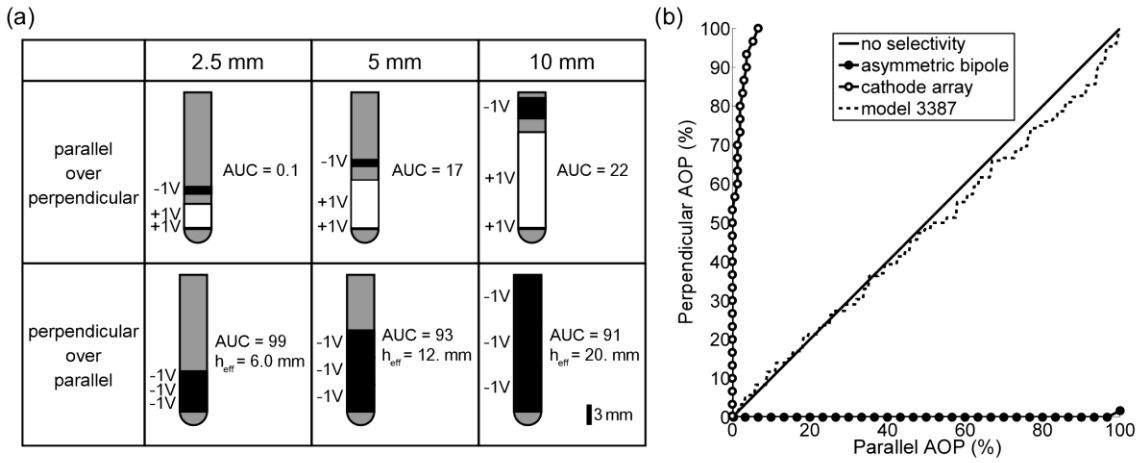

Figure 4.5: Optimal three-electrode configurations for selectively activating axons of passage (AOP) based on their orientation.
(a) Optimal electrode configurations and corresponding AUC (see Equation 4.2) when stimulating parallel AOP over perpendicular AOP (row 1) and perpendicular AOP over parallel AOP (row 2). Elements were placed ≤ 2.5 mm (column 1), 5 mm (column 2), and 10 mm (column 3) from the origin. h_{eff} is the effective or edge-to-edge length of the three-contact array. (b) Curves of the percent of perpendicular AOP activated versus select percentages of parallel AOP when AOP were placed ≤ 2.5 mm from the origin.

An additional analysis was conducted to assess how sensitive the performances (Equation 4.2) of the optimal tripolar electrode geometries were to changes in the axon orientation. Randomly rotating the parallel and perpendicular axons (by as much as -23 ° to 27 °) about the y axis in the xz plane changed AUC of the asymmetric bipoles by between 0.4 and 5.9 and AUC of the cathode arrays by between -2.4 and 1.0.

4.3.2.2 Selectivity based on type of neural element

Optimizations of the eight design parameters were conducted to identify electrode configurations that maximized selectivity of parallel TA over parallel and perpendicular AOP. An anode distal to the target population was the optimal solution for selectively activating TA over AOP. When neural elements were placed up to 2.5 mm, 5 mm, and 10 mm from the origin, distal anodes activated 50 % of target parallel TA while limiting activation of non-target parallel AOP to 1 %, 9 %, and 14 %, respectively; whereas monopolar anodic stimulation with the 3387 activated 64 %, 43 %, and 100 % of non-target elements, respectively (Figure 6). Selectivity was greatest when distal anodes were used to activate parallel TA over perpendicular AOP (Figure 6a).

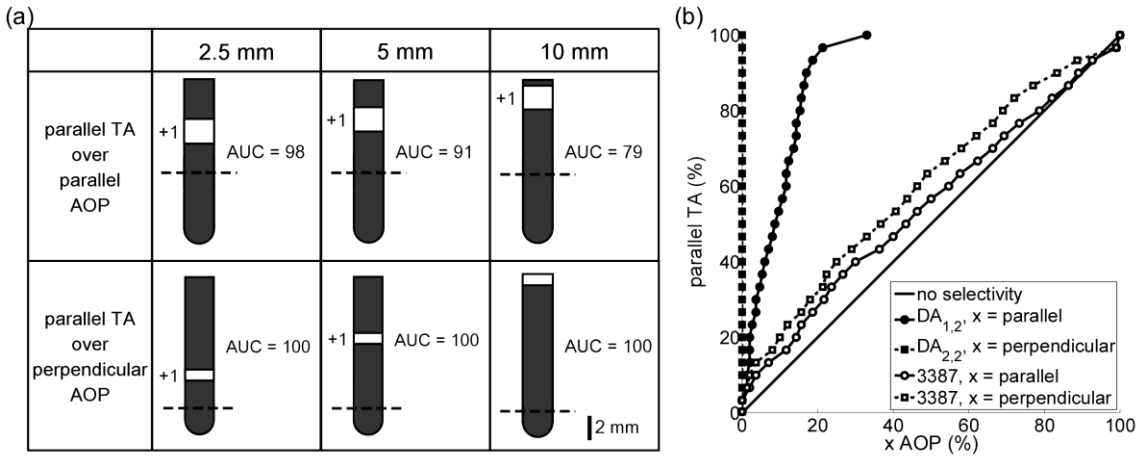

Figure 4.6: Optimal electrode configurations for selectively activating terminating axons (TA) over axons of passage (AOP).
(a) Optimal electrode configurations and corresponding AUC (see Equation 4.2) when stimulating parallel TA over parallel AOP (row 1) and parallel TA over perpendicular AOP (row 2) when neural elements were placed ≤ 2.5 mm (column 1), 5 mm (column 2), and 10 mm (column 3) from the origin. The dashed line denotes z = 0. (b) The percentage of parallel TA versus selected percentages of parallel or perpendicular AOP for the distal anodes in row 1, column 2 ($DA_{1, 2}$) and row 2, column 2 ($DA_{2, 2}$) in part a, and the 3387 electrode centered at the origin in an anodic configuration.

An additional analysis was conducted to assess how sensitive the performances of the distal anodes were to changes in the axon orientation. Randomly rotating the parallel and perpendicular neural elements about the y axis in the xz plane decreased AUC of the distal anodes by between 43 and 51 when targeting parallel TA over parallel AOP and by between 0.1 and 0.3 when targeting parallel TA over perpendicular AOP.

4.3.3. Measuring stimulation efficiency and selectivity in vivo

4.3.3.1 Efficient prototype electrodes

The electrical properties (i.e., R_a, R_f, and C_{dl}) of LHC, LC, and Model 3387 electrodes were determined by fitting Equation 3.4 to the current transient recorded during voltage-regulated stimulation (Figure 3c). The relationship between R_a and the electrode geometry observed in vivo was predicted by the computational model (Figure 7a). R_f values were between 21 and 3.9 x 10^3 kΩ, corresponding to a range of specific Faradaic resistances (i.e., r_f) between 1.3 and 490 kΩ-cm^2; and the range of C_{dl} values was between 0.64 and 6.9 μF, corresponding to specific double-layer capacitances (i.e., c_{dl}) between 6.8 and 41 μF/cm^2.

We quantified the stimulation efficiency of each prototype electrode with respective to the Model 3387 by calculating its RPU. Parallel to the sciatic nerve (n = 7), LHC and LC were less efficient than the 3387, as their RPU was significantly greater than 1, which agreed with the computational model (Figure 7c); but when oriented perpendicular to the sciatic nerve, LHC and LC performed on par with the 3387 (Figure 7d). This unexpected result was attributed to differences in the distributions of neural elements between the model and cat sciatic nerve. Perpendicular axons in the model were located above the electrode, along the shaft, and below the tip of the shaft, whereas target fascicles in the experiments were only proximal to the electrode. To emulate better the distributions of perpendicular axons in the computational model, we displaced the stimulating electrode ± 3 mm from the long axis of the sciatic nerve (Figure 7b). When

oriented perpendicular to the nerve and displaced by ± 3 mm, the RPU of LHC and LC were significantly < 1, indicating that they were more efficient than the 3387 (Figure 7d). This dependence of stimulation efficiency on displacement was also observed in the model (Figure 7c).

In brain stimulation experiments (n = 10), LHC performed on par with the 3387 when oriented both parallel and perpendicular to axons in the posterior IC, whereas LC was more efficient than the 3387 when oriented perpendicular to the target axons and displaced ± 3 mm from their long axis (Figure 7e). Post-mortem histology confirmed that the electrode tracts passed through the posterior IC in all experiments (Figure 7f).

4.3.3.2 Selective prototype electrodes

We used a five-electrode array (Figure 2) to measure the selectivity of four electrode configurations (Figure 8a): a guarded cathode, which is a cathode surrounded by two anodes; asymmetric bipole (Figure 5a); a single electrode or monopole in a cathodic configuration; and array of cathodes (Figure 5a). The guarded cathode was tested because its selectivity was similar to that of the asymmetric bipole when neural elements were placed up to 2.5 mm from the origin (results not shown), and we tested the monopolar configuration because it was expected to have no orientation-dependent selectivity (Figure 5b). We confirmed that the relationship between R_a and the electrode configuration predicted by the computational model was observed in vivo (Figure 8c).

The selectivity of the four configurations was quantified using the ratio of V_{50} in the parallel orientation to V_{50} in the perpendicular orientation. In the sciatic nerve

experiments (n = 5), the V_{50} ratio of the guarded cathode and the asymmetric bipole were significantly less when oriented parallel to the axon, the V_{50} ratio of the monopolar configuration did not differ significantly between the two orientations, and the V_{50} ratio of an array of cathodes was greater when oriented parallel to the axons (Figure 8e). The selectivity of all four configurations depended on their displacement from the long axis of the nerve. Similar results were observed in a brain experiments (n = 5), with the exception of the array of cathodes, which had significantly smaller V_{50} ratio when oriented parallel to the axon (Figure 8f). The selectivity for each configuration measured in vivo compared well with the predictions from the model-based analysis (Figure 8d).

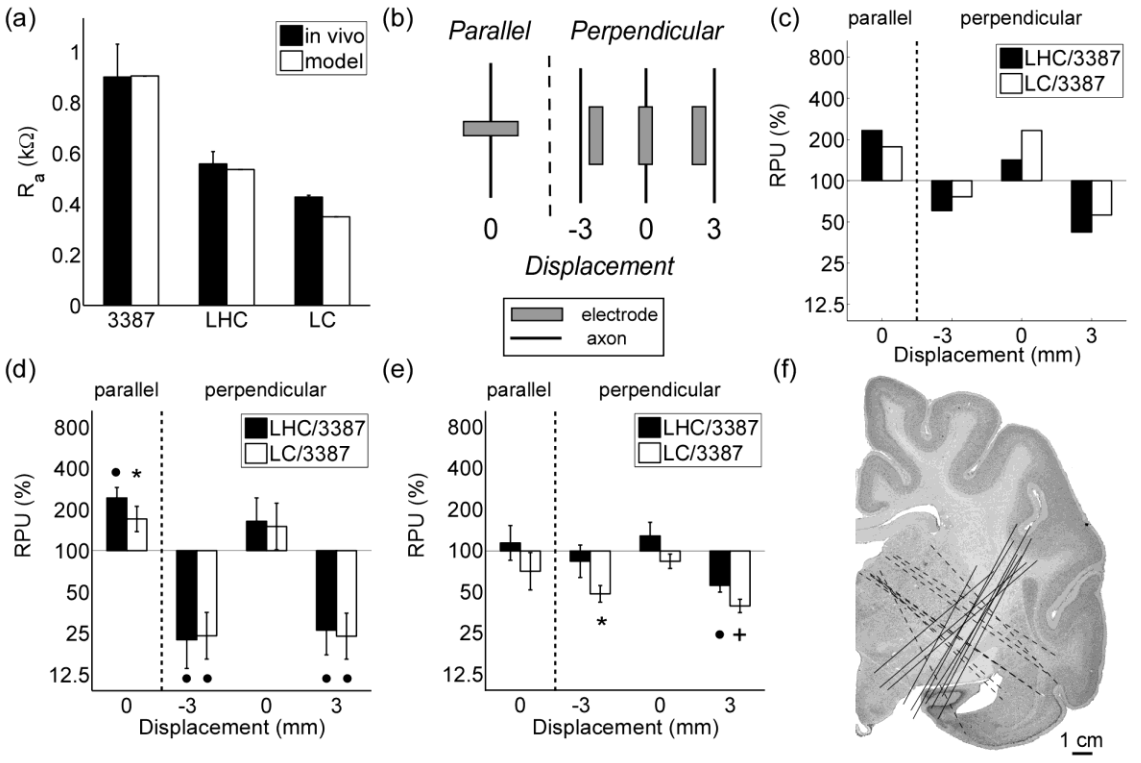

Figure 4.7: Measuring the stimulation efficiency of optimized electrode designs in vivo.
(a) The access resistance (R_a) of the prototype electrodes measured in vivo compared to R_a of the electrodes calculated from the computational model. LC = long cylinder and LHC = long hemicylinder. (b) Electrodes were oriented either parallel or perpendicular to target axons. In the perpendicular orientation, electrodes were displaced ± 3 mm from the long axis of the axon bundle. The bar graphs show the relative power usage (RPU) when activating 50 % of AOPs in (c) the computational model and the RPU when evoking a half maximal EMG response in (d) the sciatic nerve (n = 7) and (e) brain (n = 10) stimulation experiments. A repeated-measures ANOVA revealed a significant effect of electrode geometry on the relative P_{50} that depended on the orientation and distance of the electrode in parts d ($p = 0.0105$) and e ($p = 0.0242$), and post hoc comparisons were made using a Fisher's least significant difference (FLSD) test. An asterisk, bullet, and plus sign denote a p value of < 0.05, < 0.01, and < 0.001, respectively, in the FLSD test. (f) Locations of electrode tracks in the brain stimulation experiments.

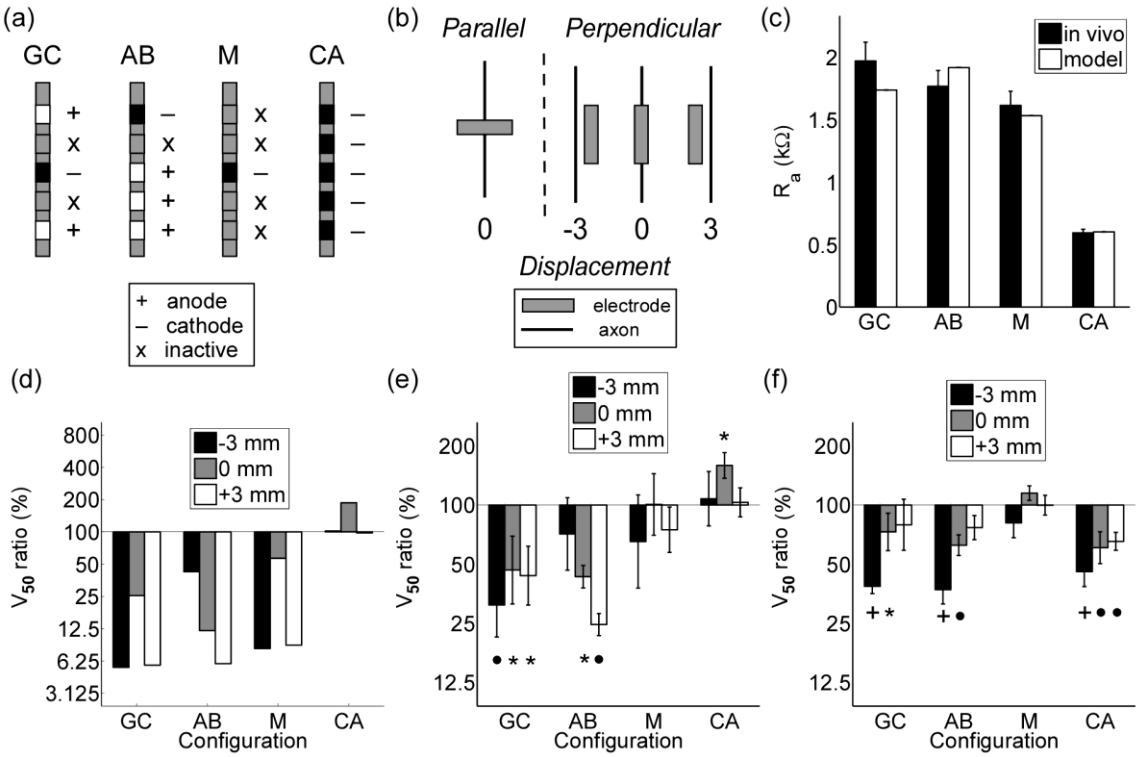

Figure 4.8: Measuring the stimulation selectivity of optimal electrode designs in vivo.
(a) Four electrode configurations were tested: GC = guarded cathode, AB = asymmetric bipole, M = monopole, and CA = an array of cathodes. (b) Electrode configurations were oriented parallel or perpendicular to target axons. Electrodes in the perpendicular orientation were displaced ± 3 mm from the long axis of the axons. (c) The access resistance (R_a) of the electrode configurations measured in vivo compared to R_a calculated from the model. (d) The voltage required to activate 50 % of modeled AOP (V_{50}) in the parallel orientation to V_{50} in the perpendicular orientation. In (e) the sciatic nerve (n = 5) and (f) brain (n = 5) stimulation experiments, V_{50} denotes the voltage required to evoke a half maximal EMG. A repeated-measures ANOVA revealed a significant effect of electrode configuration on the V_{50} ratio that depended on the orientation and distance of the electrode in parts e ($p = 0.0280$) and f ($p = 0.0288$). Post hoc comparisons were made using a Fisher's least significant difference (FLSD) test. An asterisk, bullet, and plus sign denote a p value of < 0.05, < 0.01, and < 0.001, respectively, in the FLSD test.

4.4 Discussion

We combined computational models of electric potentials and neurons and engineering optimization to design novel electrode configurations for efficient and selective DBS, and in vivo measurements of EMG responses evoked by either peripheral

nerve or brain stimulation to quantify the performance of prototype electrodes. Electrode geometry and polarity had profound effects on the efficiency and selectivity of stimulation, which depended on the orientation and type of the neural elements, and the optimal designs exhibited significant improvements in efficiency and selectivity compared to the conventional clinical electrode design, the Model 3387.

4.4.1 Principles for electrode design

The efficiency of an electrode can be increased by decreasing the electrode impedance (Z_e). The increases in efficiency of some, but not all, of the efficient designs could be explained by decreases in Z_e, but changes in Z_e could not explain why certain electrode configurations were more selective than others. Therefore, we analyzed the potentials and the second difference of the potentials ($\delta^2\Phi$) generated by the optimal designs to understand the origin of the results and how they might be translated into principles for electrode design.

Long cylindrical electrodes with a radius (r) < h were optimal for efficient stimulation of perpendicular neural elements (Figure 4a). Increasing h increased electrode area, thereby reducing R_a, decreasing R_f, and increasing C_{dl}; so the efficiency of longer electrodes could be explained, in part, by a decrease in Z_e. However, longer electrodes were not optimal for efficient stimulation of parallel neural elements, so their efficiency was also due to another factor, the proximity to the neural elements. Increasing h brings the electrode surface closer to excitable regions (e.g., nodes of Ranvier or the axon hillock) of perpendicular neural elements distributed along the insulated region of the

shaft. Since the magnitude of the potentials is greatest near the electrode surface, the stimulation thresholds of these distal elements were decreased.

Increasing h also decreases the gradient of the potentials along the electrode shaft, which translates to a decrease in $\delta^2\Phi$ (Figure 9a). This explains why LC and LHC, despite having a smaller R_a, were less efficient than the 3387 in activating parallel AOP and why longer electrodes, or similarly an array of cathodes with small interelectrode spacing, were selective in activating perpendicular AOP over parallel AOP (Figure 5a). The selectivity of long cylindrical electrodes has been studied in a computational model of electrical stimulation of the retina [43], and a longer electrode, the Model 3391, is currently being used by Medtronic to stimulate the anterior internal capsule in DBS for the treatment of obsessive compulsive disorder.

The results also revealed that multipolar configurations were optimal for selectively activating neural elements based on their orientation: the asymmetric bipole and the guarded cathode were optimal when AOP were placed up to 2.5 mm from the origin, with the former outperforming the latter, and the asymmetric bipoles was optimal when AOP were placed up to 5 and 10 mm from the origin (Figure 5a). This can be explained by considering how $\delta^2\Phi = (\Phi_{n+1} - 2\Phi_n + \Phi_{n-1})$ depends on orientation, where n denotes the n^{th} node of Ranvier. Parallel to the electrode shaft, the potentials change sign (Figures 9b and 9c), so $\delta^2\Phi$ can be as large as $|\Phi_{n+1} + 2\Phi_n + \Phi_{n-1}|$, where | | denotes the absolute value. However, perpendicular to the electrode shaft, the potentials are either positive, negative, or zero. Since the potentials perpendicular to the electrode do not change sign (Figures 9b and 9c), $\delta^2\Phi$ is only as large as $2|\Phi_n|$. Bipolar and tripolar

electrode configurations are currently used in spinal cord stimulation for the treatment of chronic pain [46, 128-130] and may hold promise for increasing spatial targeting of the therapeutic elements in DBS for essential tremor [50].

A single electrode in an anode configuration distal to the target population was optimal for selective activation of TA over AOP (Figure 6a). The selectivity of the distal anode can be explained in two parts. First, the excitability of TA is different from AOP [131] because the force driving polarization at the axon terminal is proportional to the first difference of the potentials ($\Delta\Phi$) [132]. For example, when an anode is centered at the origin, $\Delta\Phi$ in the z direction is positive when $z > 0$, zero when $z = 0$, and negative when $z < 0$. Therefore, half the terminals of a population of parallel TA (in the z direction) are depolarized, while the other half are hyperpolarized. Displacing the anode by z_e in the positive z direction such that z_e is greater than the z displacements of the terminals causes all terminals to be depolarized. Because $|\Delta\Phi|$, in general, is greater than $|\delta^2\Phi|$, TA are activated at lower stimulation thresholds.

$\Delta\Phi$ is symmetric, and a cathode displaced by z_e in the negative direction can also reduce the stimulation thresholds of TA. The second reason the distal anode was optimal for activating TA over AOP is that an anode depolarizes AOP less than a cathode, as the maximum $\delta^2\Phi$ of the former is markedly less than that of the latter. In other words, DA strongly depolarizes the terminals of TA, reducing their stimulation thresholds, while also minimizing depolarization of AOP (Figure 9d). Although the performance of DA for selective stimulation of TA over AOP has not been measured in vivo, anodes, in general,

have been studied for selective microstimulation of LN over AOP [59, 60, 133] and selective stimulation of local retinal ganglion cells over passing axons of distal retinal ganglion cells [44].

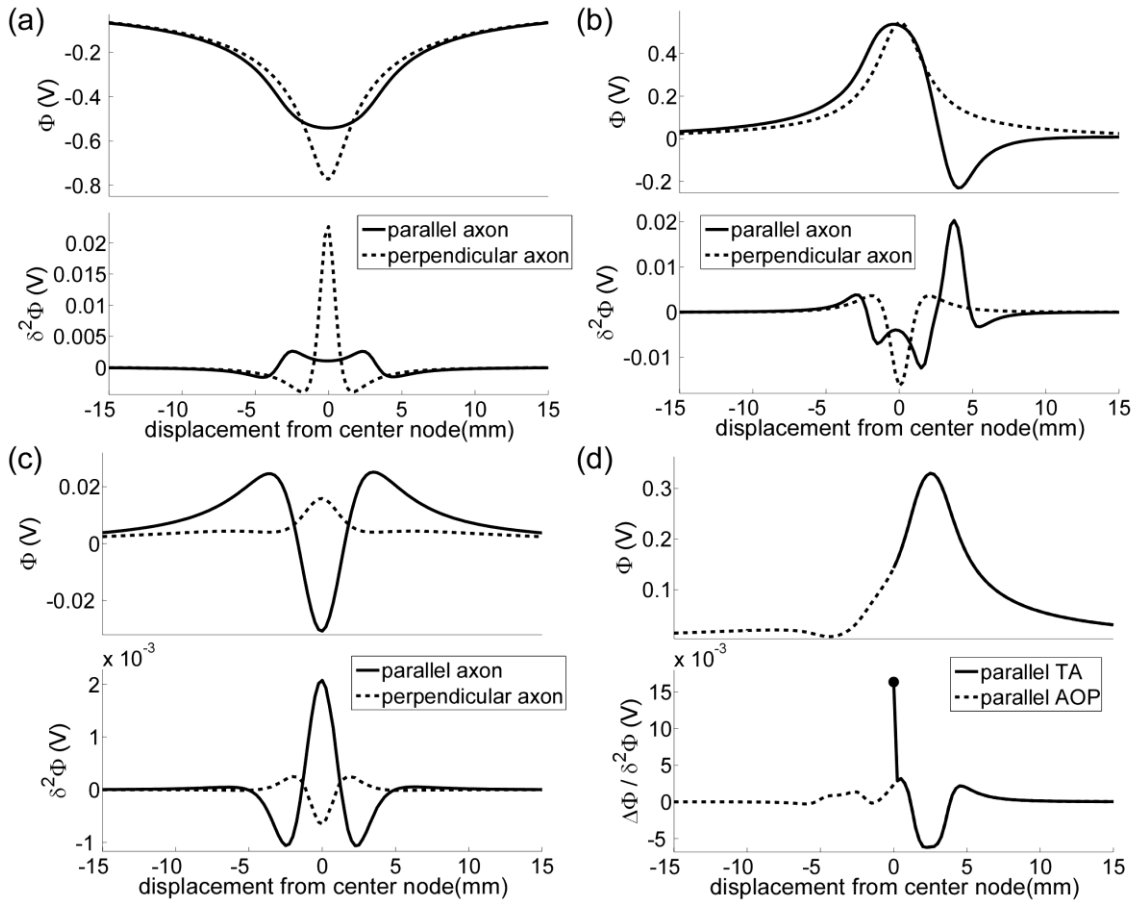

Figure 4.9: The effect of electrode geometry and polarity on the force driving polarization of the neural membrane.
Shown are the potentials and second difference of the potentials ($\delta^2\Phi$) generated by (a) a long cylindrical electrode (Figure 4.4a), (b) an asymmetric bipole (Figure 4.5a), (c) a guarded cathode (Figure 4.8a), and (d) a distal anode (Figure 4.6a) across the nodes of Ranvier of an axon of passage (AOP). The filled circle in d denotes the first difference of the potentials ($\Delta\Phi$) at the terminal of a terminating axon (TA).

4.4.2 Differences between computational and in vivo results

Our computational model of DBS indicated that LC and LHC electrodes (i.e., r < h) are optimal for efficient stimulation of perpendicular neural elements, whereas shorter electrodes, with geometries similar to the Model 3387, are optimal for efficient stimulation of parallel neural elements (Figure 4a). The results of the sciatic nerve experiments supported these predictions (Figure 7d), but in the brain experiments, there were differences with the model results (Figure 7e). The LHC – rather than being more efficient – was less efficient than LC. Because LHC is not axially symmetric, we conducted additional simulations to assess how its performance varied with axial rotations (Figure 10). Rotating LHC about its axis markedly reduced its efficiency, so the difference between model and experiment could be explained by suboptimal alignment of LHC with the target axons.

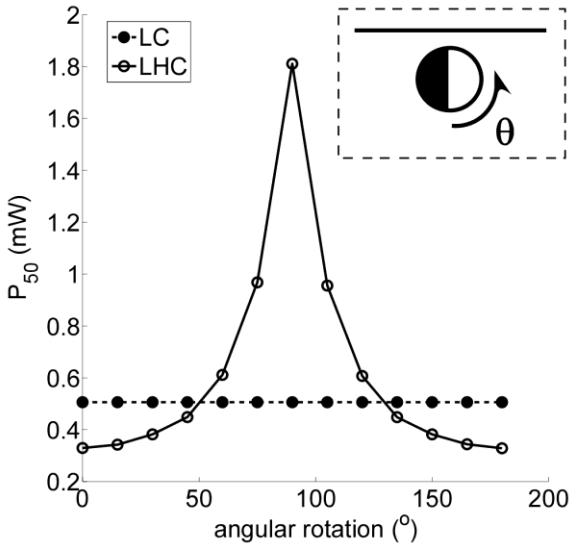

Figure 4.10: The stimulation efficiency of the long cylinder (LC) and long hemicylinder (LHC) at different rotations about their axes.
P_{50} is the average power consumed when activating 50 % of a modeled axon population oriented perpendicular to the electrode shaft. Inset: cross-section of LHC at an angular rotation (θ) of 0° with respect to a target axon (solid line) and the direction of rotation.

Another difference between the predicted and observed results was that the efficiency of the LC and the 3387 were not significantly different when oriented parallel to the target brain axons (Figure 7e). Recall, long electrodes, despite a smaller Z_e than the 3387, were expected to be less efficient because increasing h decreased $\delta^2\Phi$ parallel to the electrode axis (Figure 9), thereby increasing stimulation thresholds. Indeed, the computational model was able to reproduce the relationship between R_a and electrode geometry (Figure 7a) and addressed the impact of the ETI impedance of the predicted efficiency. However, the model did not account for the heterogeneous and anisotropic electrical properties of the tissue. For example, white matter is ~9 times more conductive parallel to the axons than perpendicular to the axons [83], and spaces filled with cerebral spinal fluid are ~10 times more conductive than grey matter [100]. These electrical

properties alter that shape of the potential distribution and resulting excitation thresholds [73].

The results of the experiments to measure selectivity were consistent with many of the model predictions (Figures 5 and 8e). In the sciatic nerve experiments, the asymmetric bipolar and guarded cathode were selective in activating parallel AOP over perpendicular AOP, indicated by lower stimulation thresholds in the former case; the monopolar configuration showed no selectivity based on orientation; and the array of cathodes was selective in activating perpendicular AOP over parallel AOP. Similar results were observed in brain experiments, except for the array of cathodes, which was selective in activating parallel AOP over perpendicular AOP (Figure 8f). We predicted that this unexpected result could be explained by the geometry of the targeted corticospinal axons, which are not straight, like the axons in the sciatic nerve.

Many corticospinal (CS) axons in the IC originate from the motor cortex [134]. In cats, CS axons travel from rostral to caudal, and as they pass through the IC, they course medially to form the cerebral peduncle – and in turn, the pyramidal tracts [116]. Our electrode designs were implanted in the posterior IC, caudal to the optic chiasm and rostral to the cerebral peduncle. Therefore, we predicted there would be bends in CS axons rostral and caudal to the target region. We used anatomical images from a cat atlas [116] and spline fits to approximate a population of CS axons that followed the trajectory described above (Figure 11a), and additional simulations were conducted to assess the impact of axon geometry on selectivity. With straight axons, arrays of cathodes consisting of 4 or 5 electrodes had larger stimulation thresholds than a monopolar

configuration when oriented parallel to the modeled AOP, whereas with curved CS axons, all thresholds with the arrays of cathodes were less than the monopolar threshold (Figure 11c).

Similar results were observed in two additional experiments, where arrays of cathodes consisting of 2-5 electrodes were used to stimulate the sciatic nerve and posterior IC, respectively. In both experiments, a cathode array with 2 electrodes had a smaller V_{50} than the monopole when oriented parallel to the target axons. This was expected since the former has a smaller Z_e than the latter. Z_e continues to decrease with increasing number of electrodes, but so does $\delta^2\Phi$ parallel to CA (Figure 9a). If the reduction in $\delta^2\Phi$ is large enough, V_{50} will increase, rather than decrease, as the number of electrodes in the cathode array increases. This effect was observed when stimulating the sciatic nerve, where axons are straight, but not when stimulating axons with bends in the posterior IC (Figure 11d). Therefore, the geometry of the axon is a crucial parameter to consider in future studies, as electrode-geometry dependent selectivity was dependent on the axon geometry.

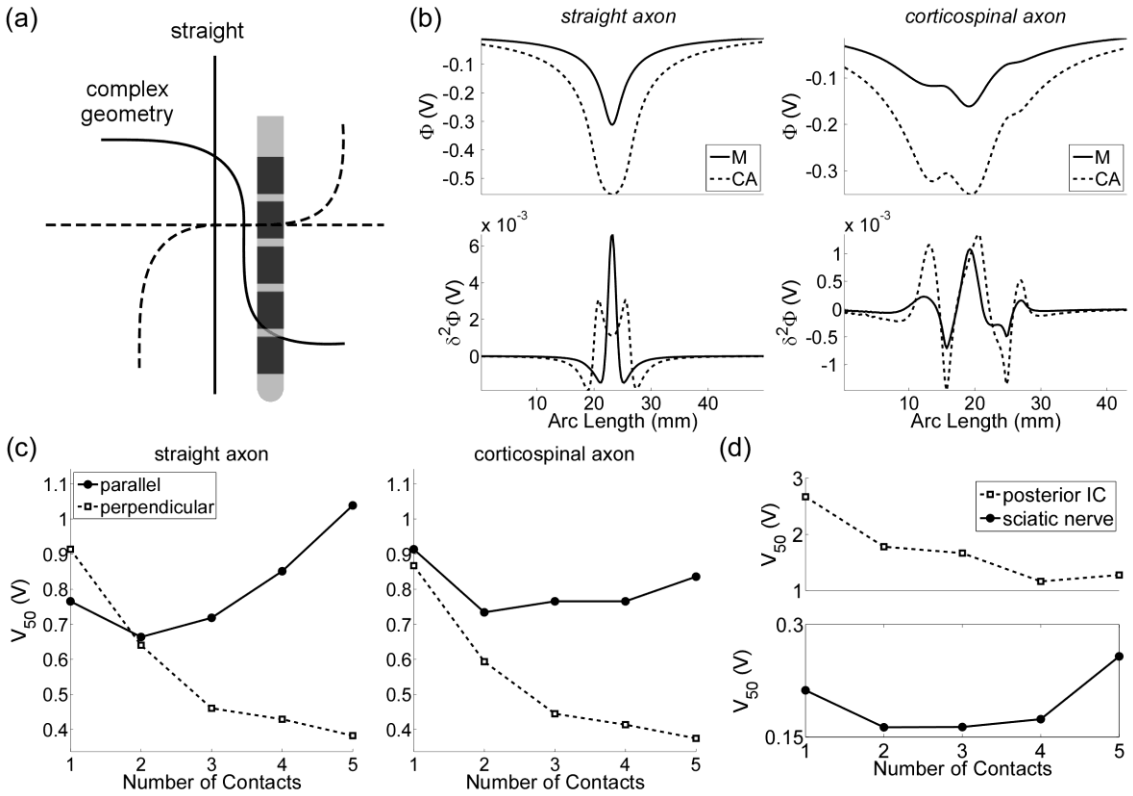

Figure 4.11: The effect of axon geometry on stimulation thresholds.
(a) A straight axon and corticospinal axon with bends oriented parallel (solid line) and perpendicular (dashed line) to a five-electrode array. (b) The potentials (top) and the second difference of the potentials ($\delta^2\Phi$, bottom) when either one (M) or five contacts (CA) in a cathodic configuration was used to stimulate the target axons. (c) The voltage required to activate 50 % of a population of modeled straight and corticopsinal axons (V_{50}) when the array was oriented parallel or perpendicular to the axons. (d) The voltage required to evoke a half maximal EMG (V_{50}) when the array was oriented parallel to the posterior internal capsule (IC, top) and sciatic nerve (bottom).

4.4.3 Limitations

One limitation of this study was the choice of animal model for testing the electrode designs. Targets in DBS for movement disorders, including the subthalamic nucleus and the ventral intermediate nucleus of thalamus, span a length scale of 1-10 mm in humans [50, 135], and the neural volumes activated at therapeutic stimulation levels are predicted to span similar length scales [72]. In contrast, the cat sciatic nerve [136] and

the posterior IC [83] span a length scale of 1-3 mm, but in these tissues, EMG activity in a single muscle group can be evoked by activating a small population of axons that occupy a length scale of < 1 mm. To emulate the presence of perpendicular axons distal to the electrode (i.e., along the shaft insulation and below the shaft tip), we displaced the electrodes ± 3 mm when oriented perpendicular to the target axons. While many of the qualitative trends observed experimentally could be reproduced with the model (Figures 7c and 8d), experiments in larger animals may provide more accurate evaluation of optimal electrode designs.

As described above, the simplified FEM model did not account for heterogeneity or anisotropy of brain tissues. However, our model reproduced the dependence of R_a on the electrode configuration (Figures 7a and 8c) and had two advantages: (1) model solution times were less than thirty minutes, allowing us to study a very large parameter space of possible electrode designs; and (2) the effects of electrode geometry and polarity on the potentials could be studied in isolation from other variables, such as heterogeneities in the conducting volume, that can also affect the potentials [100]. The simplified model, however, did not reproduce all of the experimental findings. It is possible that these discrepancies between the model and experiments may be due to anisotropy and heterogeneity in the conductivity of brain tissue and/or the geometry of the target neural elements (Figure 11), and future computational models should account for these features when designing electrodes for specific DBS applications [72, 73, 137].

4.5 Conclusion

Model-based engineering optimization was used to design electrodes that increased the efficiency and selectivity of DBS. Electrodes with heights greater than the 3887 electrode were the most power efficient for stimulating neural elements oriented perpendicular to the long axis of the electrode, and electrodes with geometries similar to the 3387 electrode were the most power efficient for stimulating parallel neural elements. Bipolar and tripolar electrode configurations were optimal for activating parallel axons over perpendicular axons; an array of cathodes with short interelectrode spacing, or equivalently, an elongated cylindrical electrode, was optimal for activating perpendicular axons over parallel axons; and an anode displaced from the center of the target region was optimal for selectively activating terminating axons over passing axons. The performance of these designs could not be explained solely by differences in their electrical properties, suggesting that field-shaping effects from changing electrode geometry and polarity can be on par with or greater than the effects of decreasing electrode impedance.

Chapter 5 : Evaluation of Stimulation Efficiency and Selectivity in a Computational Model of Spinal Cord Stimulation

5.1 Introduction

Chronic pain is a prevalent and clinically challenging condition for which there are often not adequate treatments. For example, chronic low back pain has a lifetime prevalence between 11-84 % [138], is the most common cause of lost time due to disability [139], and imposes an annual economic burden of ~$20-$120 billion [140]. Standard treatments for chronic pain, such as physical rehabilitation, pharmaceuticals (e.g., opioids), and surgery work for some individuals; but for others who do not receive satisfactory pain relief from standard treatments, alternative approaches are required.

Spinal cord stimulation (SCS) is an alternative or adjunct therapy for treating chronic pain [21], where an implanted pulse generator delivers electrical pulses to an electrode array placed in the epidural/extradural space. SCS is FDA approved for treating chronic low back and limb pain, including complex regional pains syndromes I and II and failed-back surgery syndrome [19], and it is currently being investigated for other chronic pain conditions, including ischemic limb pain, angina, and pain from peripheral neuropathy [8, 141]. SCS is based on the gate-control theory of pain [142], which postulates that activation of cutaneous (Aβ) nerve fiber collaterals in the posterior/dorsal column (DC) of the spinal cord synaptically inhibits projection neurons in the dorsal

horn, which transmit pain-related information to the brain [143]. Although the gate-control theory is still an incomplete model of pain processing in the spinal cord [144-147], it predicts well the analgesic effects of SCS [148, 149]. Activation of Aβ fibers elicits paresthesia in the corresponding dermatome, and it is generally accepted that SCS requires the evoked paresthesia to overlap the painful area [150].

Despite substantial clinical success [8, 19], SCS is still prone to failures: the three most common being lead breakage, lead migration, and the inability to activate the target DC fibers [8, 151]. Currently, there are two electrode designs used in SCS: a percutaneous (PERC) design, consisting of 4-8 annular electrodes distributed along a flexible cylindrical shaft, which is inserted with a hypodermic needle; and a laminectomy/paddle design (LAM) implanted during a surgical laminectomy, consisting of a grid of 4-20 rectangular electrodes on a flexible planar substrate. PERC designs are less invasive but more prone to lead migration than LAM designs [151], while LAM designs, although more invasive and prone to fracture [151], are, in practice, more energy efficient and evoke fewer side effects than PERC designs [129, 152, 153].

Activation of DC fibers in the dermatomes associated with pain is often limited by the onset of discomfort. Since discomfort is associated with activation of nearby Aβ fibers in the dorsal roots (DR) [41, 42], successful SCS is thought to depend on activation of DC fibers without activation of DR fibers, which we term selectivity. Selectivity can be improved using longitudinal (rostral-caudal) and transverse (medial-lateral) bipolar and tripolar electrode configurations [46, 47, 130, 154], mitigating the sensitivity to malposition or migration of the electrode array. However, there is a limit to selectivity

with extradural placement due to the large distance between the electrodes and the neural elements, and the high conductivity of the intervening cerebrospinal fluid.

The shunting effects of the CSF can be surmounted by placing the electrodes below the dura mater and adjacent to the dorsal aspect of the spinal cord [155, 156]. Directing less current through the CSF and more through the spinal cord results in a potential distribution with isopotential contours more closely spaced on the side of the electrode facing the spinal cord. As a result, there is a greater difference in the magnitude of the potentials between the DC and DR fiber populations. DR fibers, however, are more excitable than DC fibers of the same diameter because of their curved geometry and entry into the white matter from the CSF, where the tissue conductivity changes drastically [42]. Therefore, if increasing the proximity of the electrode to the spinal cord does not substantially increase the excitability of DR fibers over DC fibers, subdural/intradural SCS may have substantially greater selectivity than extradural SCS.

Intradural electrode placement was used when SCS devices were first implanted in humans. Because intradural electrodes are more prone to movement than extradural electrodes, and because the first electrodes had a limited number of contacts, adjustments following implantation were difficult [157]. Moreover, multi-level laminectomies and large dural openings introduced additional risks, including exposure to general anesthesia, cerebral spinal fluid (CSF) leaks, and increased postoperative pain and tissue scarring [158]. For these reasons, intradural SCS was abandoned. However, with the advent of new techniques [159] and electrode designs [155] for addressing movement of the spinal cord and electrode, the possibility of intradural SCS is being revisited.

The goal of this study was to develop a computational model of SCS. We compared the stimulation thresholds predicted by the model to stimulation thresholds measured intra-operatively and used the model to compare the performances of extradural and intradural SCS. The outcome is a quantitative understanding of how intradural electrode placement can potentially increase the selectivity and efficiency of SCS, which, in turn, provides predictions that can be tested in future clinical studies assessing the potential therapeutic benefits of intradural SCS. The final version of this work is published in PLOS ONE [160].

5.2 Methods

5.2.1 Volume conductor model of the spinal cord and SCS electrode

The finite element method (FEM) was used to construct a volume conductor model of the spinal cord and an implanted three-contact percutaneous electrode array in COMSOL Multiphysics v3.4 (COMSOL Inc., Burlington, MA) (Figure 5.1). Three electrodes were chosen to enable monopolar (−), bipolar (+ −), and tripolar (+ − +) configurations. The model spine consisted of 12 vertebrae, thoracic level 3 (T3) to lumbar level 2 (L2), spaced by disks, and a dural sac and spinal cord that traversed the spinal canal. The model spine was placed within a rectangular prism of homogeneous soft tissue that was large enough (100 mm x 100 mm x 300 mm) to behave as an infinite conducting medium (Figure 5.1). Spinal dimensions were consistent with those of an adult human lower thoracic/upper lumbar spine [161-164]. All tissues were modeled as purely resistive [82, 165], with electrical conductivities from published data (Table 1).

A Delaunay triangulation algorithm was used to discretize the FEM model into a graded mesh of Lagrange tetrahedral cubic elements, where the mesh density was greatest near the electrode surfaces, spinal cord, and dura mater. The shaft of the array was assumed to be perfectly insulating and was modeled as a boundary layer with zero normal current density (i.e., Neumann boundary condition). Monopolar stimulation was modeled by applying potentials of 1 V and 0 V (i.e., Dirichlet boundary conditions) on the surface of the stimulation electrode and outer surface of the tissue volume, respectively. Bipolar and tripolar configurations were modeled by applying potentials of +1 V and −1 V and +1 V, −1 V, and +1 V to either 2 or 3 consecutive contacts, respectively. In the bipolar and tripolar cases, the cathode served as the return, and the outer tissue boundary was assumed to be perfectly insulating. The electric potentials (Φ) generated in the tissue by the electrode array were calculated by solving Laplace's equation (Equation 2.1); the applied current was calculated by integrating the current density (Equation 2.2) on the surface of electrodes with positive applied potentials (i.e., anodes); and, the lumped resistance of the tissue, also known as the series or access resistance (R_a), was calculated by dividing the voltage between the anode and cathode by the applied current.

Table 5.1: Electrical conductivity of tissues represented in volume conductor model of spinal cord stimulation

Tissue	Conductivity (S/m)	Reference
White matter, longitudinal	0.60	[165]
White matter, transverse	0.083	
Grey matter	0.23	[159]
Cerebrospinal fluid	1.8	[166]
Dura mater	0.030	[167]
Extradural space[a]	0.20	[168]
Vertebral bone	0.02	[169]
Intervertebral disc	0.65	[170]
Muscle [b]	0.20	[171]

[a] The lumped conductivity of the extradural space was assumed to be similar to that of muscle.

[b] Tissue surrounding spine.

5.2.2 Population model of dorsal column and dorsal root axons

We used the NEURON (v7.1) simulation environment to implement cable models of dorsal column (DC) and dorsal root (DR) fibers, and to calculate their response to modeled SCS. Two different non-linear cable models of axons with Hodgkin-Huxley-type ion channels were used: a mammalian axon model with perfectly insulating myelin [85], the SW model, which was used in previous computational models of SCS [41, 42, 46, 47, 130, 153, 154, 167, 172-174]; and a more detailed model of a myelinated mammalian axon, the MRG model [102], which takes into account the structure and electrical properties of the myelin.

Because the myelin in the SW model is assumed to be perfectly insulating, only the nodes of Ranvier (NoR) and internodal resistance were modeled. The membrane at each NoR contained a parallel combination of a nonlinear sodium conductance, a linear

leakage conductance, and a membrane capacitance [85]. In the MRG model, each NoR contained fast and persistent sodium conductances, a slow potassium conductance, a linear leakage conductance, and a membrane capacitance; and the membrane underneath the myelin contained a linear leakage conductance and a membrane capacitance [102].

The dorsomedial white matter of the spinal cord (i.e., between the dorsal boundary of the spinal cord and the grey matter) was split into 11 dermatomes based on the mediolateral segmental lamination of DC fibers [175, 176]. A total of 200 DC fibers were bilaterally distributed – 10 fibers within each of the 10 most medial dermatomes on either side of the transverse midline (Figure 5.2c) – representing collaterals that originated from distal, caudal DR fibers, which were not modeled. An additional 200 DC fibers were bilaterally distributed in the lateral-most dermatome, and these fibers were attached to the proximal end of 200 corresponding DR fibers. DR fibers descended from the dorsal aspect of the spinal cord in a ventrolateral direction (i.e., via the rootlets) and exited the spine through the intervertebral foramina [42] (Figure 5.2d).

The diameters of myelinated fibers in the dorsomedial white matter range between 1-15 μm [177]. Although the vast majority (> 60 %) of the fibers have diameters between 1-7 μm [178], prior computational modeling studies have shown that fibers as large as 12 μm are activated within the therapeutic range of in SCS [41]. We considered nine separate populations of 200 DC fibers with diameters of 3, 6, 9, 12 and 15 μm; and nine separate populations of 200 DR fibers with the same diameters.

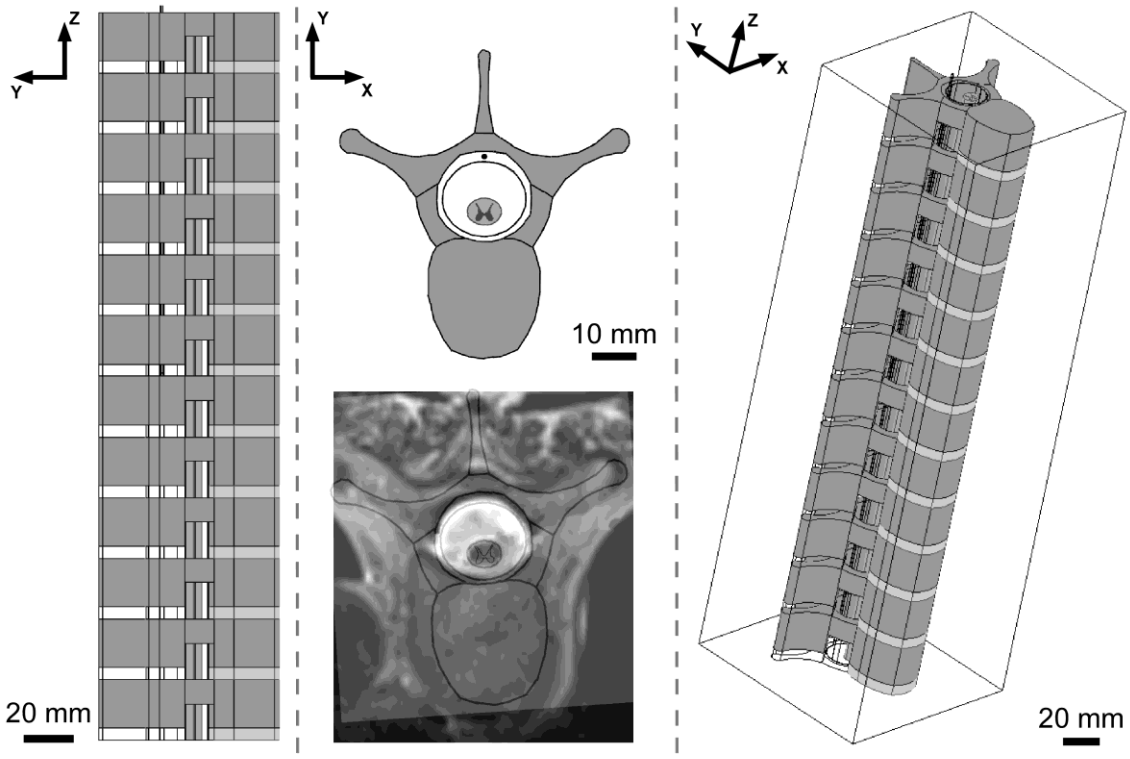

Figure 5.1: Finite element model of the spine and spinal cord.
Sagittal (left), transverse (middle-top), and 3D (right) views of the modeled spine, which consists of 12 vertebrae spaced by disks and a dural sac and spinal cord that traversed the spinal canal. The transverse section of the modeled spine is overlaid with a transverse magnetic resonance image of the spine of Patient 2 (middle-bottom).

Potentials were calculated using the maximum possible number of cubic elements (~ 1.34 million) with 8 GB of memory. Refinement of the FEM mesh (i.e., splitting elements into smaller elements) from ~ 635,000 to 1.34 million cubic elements resulted in errors of < 1 % in the potentials and corresponding stimulation thresholds of the modeled fibers, where error was defined as the mean absolute relative difference between the refined solution and the solution prior to refinement. Similarly, doubling the tissue volume yielded errors of < 2 % and < 1 % in the potentials and stimulation thresholds of the modeled fibers, respectively.

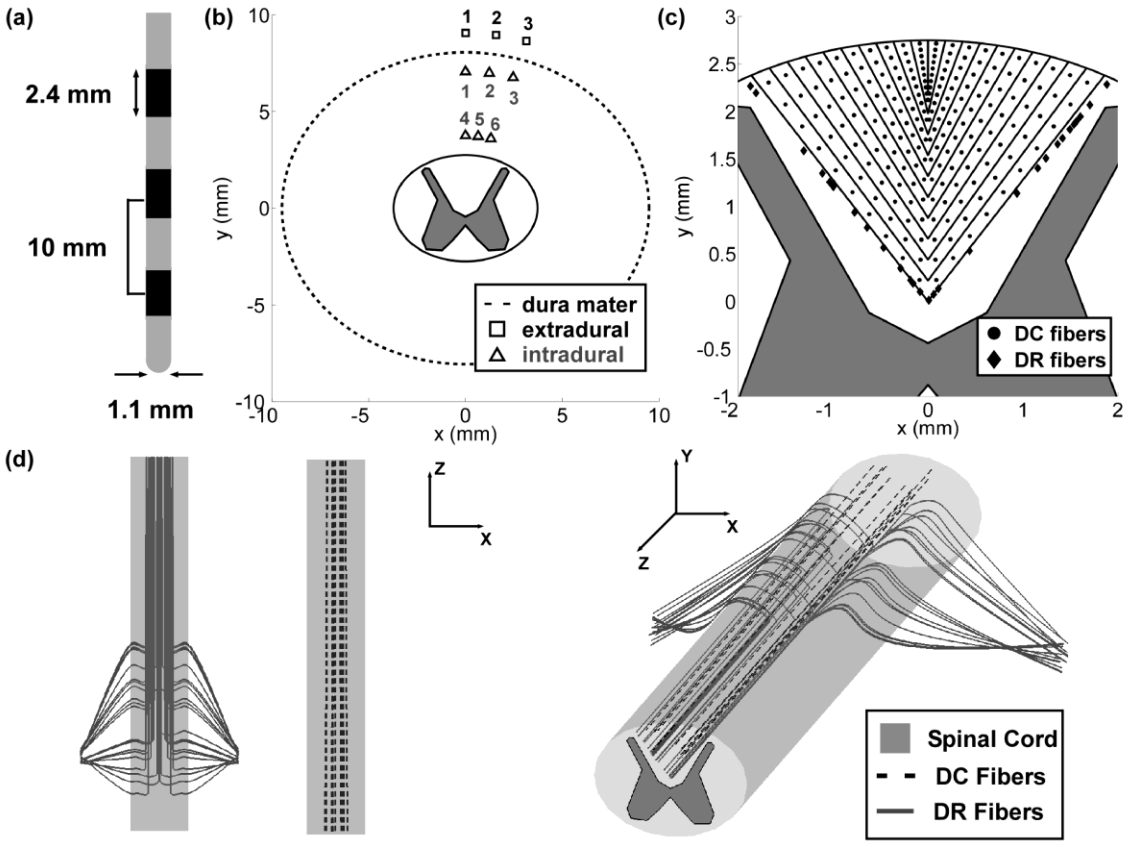

Figure 5.2: Placement of model dorsal column (DC) fibers, model dorsal root (DR) fibers, and the stimulation electrode.
(a) The modeled percutaneous array was placed in (b) nine different locations: three extradural locations and six intradural locations. (c) Transverse view of the spinal cord showing the locations of the modeled DC fibers and DR fibers within the dorsomedial white matter. (d) Planar dorsal and lateral views (left) and 3D view (right) illustrating modeled DC fibers and DR fibers.

5.2.3 Clinical protocol

Five subjects were enrolled in a controlled exploratory study of acute SCS trial system implantation (NCT02020460 on clinicaltrials.gov). The Duke University

Institutional Review Board approved the study, and all participants gave written informed consent.

5.2.4 Model evaluation

We constructed five models of SCS based on the individual spinal cord dimensions of patients that had undergone acute intraoperative evaluation of extradural and intradural SCS. Preoperative magnetic resonance imaging (MRI) scans of the corresponding patients were used to measure the geometries of the spinal cord and dural sac, and the position of the cord within the sac (Table 2). The geometry of the modeled spinal column did not vary across patients and reflected the geometry of an average adult human lower thoracic/upper lumbar spine [161-164] (Figure 5.1).

Patient-specific models were evaluated at nine different electrode locations (Figure 5.2b): three extradural locations 1 mm above the dura, three intradural locations 1 mm below the dura, and three intradural locations 1 mm above the spinal cord, where points one, two, and three in each set had lateral (clockwise) offsets of 0°, −10°, and −20° from the transverse midline, respectively.

Clinical conditions were emulated by stimulating the model DC and DR fibers with a 300 μs monophasic rectangular pulse, consistent with typical pulse widths (175-600 μs) used in SCS [179]. The cathode was proximal to T8, and the distal anode was rostral to the cathode. Due to linearity of the solution, the potentials at a given stimulus amplitude were calculated by multiplying the base (monopolar, bipolar, or tripolar) solution by a scalar. The stimulation threshold voltage for each fiber was calculated using

a bisection algorithm (relative error < 1 %). The stimulation threshold current was calculated by dividing the threshold voltage by R_a, and input-output curves of the number of activated model nerve fibers as a function of the stimulation amplitude and stimulation power were constructed.

The stimulation thresholds of the MRG and SW model fibers were compared to the clinically measured sensory thresholds, when the patient first reported a paresthesia, and the discomfort threshold, when the patient first reported pain or discomfort. We used the following procedure to determine the percentage and diameter of DC fibers that most closely matched the clinical findings. First, for each diameter, we calculated the percentage of DC fibers activated at the sensory and discomfort thresholds. Next, because two hundred model DC fibers were evenly split across 20 laminae (Figure 5.2c), the clinical findings were translated into an expected percent activation by assuming that paresthesia in one dermatome on one side of the body corresponded to activation of 5 % of the modeled DC fibers. The DC fiber population (of a given diameter) that best matched clinical findings was defined as the one whose percent activation at the clinical thresholds most closely matched the expected percent activation based on the number of dermatomes reported at the clinical thresholds.

Table 5.2: Spinal Cord Geometry from Individual Patients[a]

	Spinal Cord Dimensions (mm)		CSF Space Dimensions (mm)		Spinal Cord Placement[b]
Patient	Mediolateral	Ventrodorsal	Mediolateral	Ventrodorsal	
1	7	6	19	16	center[c]
2	8	7	21	18	ventral[d]
3	8	6	20	14	center
4	9	6	18	13	center
5	8	6	18	15	ventral

[a] Geometries were measured from MRI images (at 1.5 Tesla) with a resolution of 1 mm.
[b] Placement with respect to midline
[c] Spinal cord center placed at the center of the elliptical shell defining the dura mater
[d] The spinal cord center was twice as far from the dorsal interior surface of the dura mater as it was from the ventral interior surface of the dura mater

The model of SCS was used to quantify the efficiency and selectivity of stimulation. Stimulation efficiency was quantified by calculating the average electrical power (Equation 5.1) consumed during the stimulation pulse to activate the target DC fibers:

$$\overline{P} = PW^{-1} \int_0^{PW} \frac{V^2(t)}{R_a} dt \tag{5.1}$$

, where V(t) is the applied voltage, and PW is the duration of the rectangular pulse.

Selectivity was quantified using two different metrics: neural-element selectivity was analyzed by calculating the percent of DC fibers activated with no activation of DR fibers (DC_0) or with activation of a certain percentage (X) of DR fibers (DC_X), and

dermatome selectivity was analyzed by determining if DC fibers in target dermatomes could be activated without activation of DC fibers in non-target dermatomes. Since the computational models were based on data from patients receiving SCS for the treatment of chronic low back pain, we chose the low back dermatomes, L2-L5, to assess dermatome selectivity.

5.2.5 The effect of electrode geometry

In addition to analysis with the lead (AD-TECH Spencer Probe Depth Electrode) used in the clinical experiments, simulations were conducted to test the extradural and intradural performance of five different electrode designs (Figure 5.3): LT-1.5 and LT-6, which are two percutaneous leads, Medtronic Models 3776/3876 and 3777/3877 (Medtronic Inc., Minneapolis, MN), in longitudinal tripolar configurations with an inter-electrode spacing (IES) of 1.5 mm and 6 mm, respectively; TT-1 and TT-3, which are the St. Jude Medical Penta^{TM} (St. Jude Medical, Saint Paul, MN) in two transverse tripolar configurations with an IES of 1 mm and 3 mm, respectively; and our own novel design.

TTs are believed to have greater selectivity than LTs because their distal anodes hyperpolarize the DR fibers, termed anodal shielding [130, 153, 154]. However, we believed that the superior selectivity of TTs over LTs arose from their ability to steer current away from DR fibers so that the potentials decayed more rapidly with increasing distance from the cathode. To test this, we modeled a fifth tripolar design, a percutaneous azimuthal array in an angular tripolar (AT) configuration, which had a cathode adjacent to the dorsomedial aspect of the spinal cord and anodes that directed current away from

the cord, toward the dorsal aspect of the dura (Figure 5.3). The performance of all five designs was assessed with the each electrode array placed along the transverse midline, extradurally 1 mm above the dura mater and intradurally 1 mm above spinal cord (Figure 5.2b).

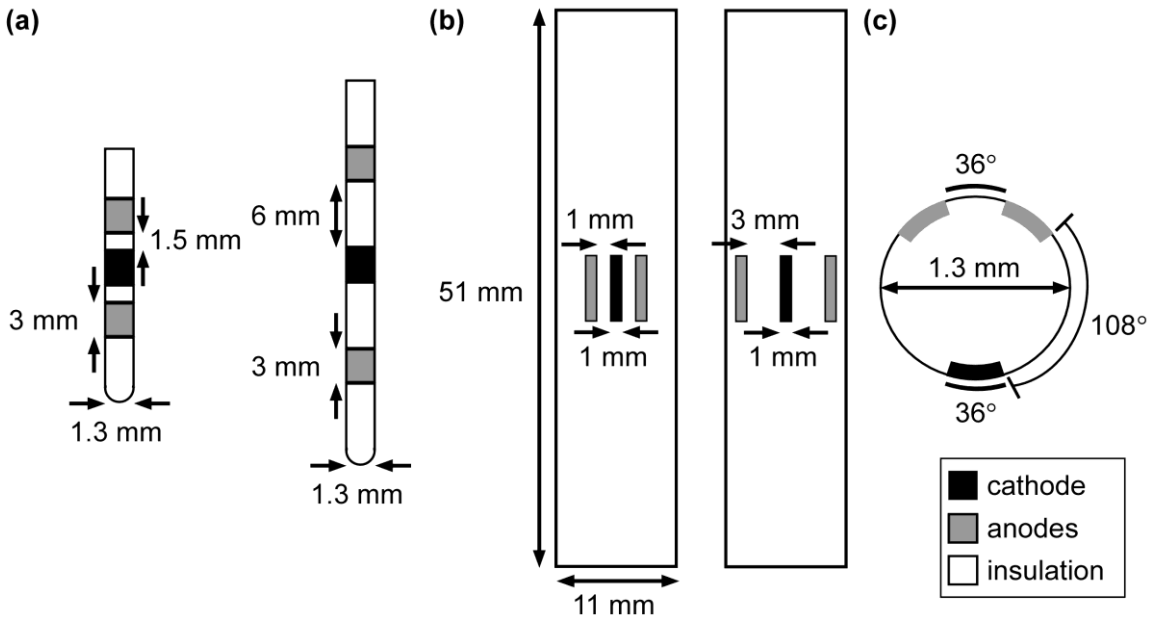

Figure 5.3: Five SCS electrode designs evaluated with the computational model.
(a) Medtronic Models 3776/3876 (left) and 3777/3877 (right) in longitudinal tripolar configurations. (b) St. Jude Medical Penta™ in two transverse tripolar configurations. (c) A transverse view of a novel percutaneous lead with an azimuthal array of electrodes in a tripolar configuration. Inactive contacts were not represented.

5.2.6 Statistical Analyses

The computational models of Patients 1-5 account for the effects of anatomical variability in the spinal geometry across patients. Yet, five sets of spinal geometries were not sufficient to determine if the geometrical parameters and subsequent output metrics (e.g., R_a and DC_0) varied normally across patients, so we used a Kolmogorov-Smirnov (K-S) test to determine differences in the distributions of the output metrics across Patients 1-5. The K-S test assumes nothing about how the output metrics are distributed, and all K-S tests were run at a significance level of 5 % ($\alpha = 0.05$).

Linear regression and subsequent calculation of coefficients of determination (r^2) were used to determine whether the variability in the sensory and discomfort thresholds could be explained by differences in anatomical measurements across patients.

5.3 Results

We constructed five patient-specific models of SCS, compared the model stimulation thresholds to clinical stimulation thresholds (Appendix C), and used the models used to quantify the efficiency and selectivity of both intradural and extradural SCS.

5.3.1 Comparing model predictions with clinical data

We used the number of dermatomes reported by patients at the sensory and discomfort thresholds to determine the diameter of the MRG model of DC fibers that

most closely matched the clinical findings. The diameter of the model DC fiber population that most closely matched the sensory thresholds differed across patients and between the intradural and extradural cases in some of the patients, and the same was true for the diameters that most closely matched the discomfort thresholds (Figure C.2). Patients 2 and 3 reported paresthesia in T8 at their sensory thresholds, but because this was not consistent across patients in the intradural and extradural cases, we did not compare the percentage and diameter of DR fibers to the sensory thresholds.

At the discomfort threshold in Patients 1-5, the locations of the paresthesias ranged from T8-S5 (Figure C.1), so we determined whether an increase in the activation of DC fibers or activation of DR fibers could predict discomfort. For all diameters except 3 μm ($p = 0.03$), the distributions of the percentage of DC fiber activated at the discomfort and sensory thresholds across patients were not significantly different, and for all fiber diameters, there was no significant difference between the distributions of the percentage of DC and DR fibers activated at the discomfort thresholds.

In addition to the above, we also compared the stimulation thresholds of SW models of DC fibers to the clinical stimulation thresholds. With the SW model, the diameter of the DC fiber population that most closely matched the sensory threshold was different across patients and between the intradural and extradural cases in some of the patients. In general, the stimulation thresholds predicted by the SW model were greater than the stimulation thresholds predicted by the MRG model, so compared to the MRG model, the SW model predicted that DC fibers with larger diameters were activated (Figure 5.4).

Because fibers with diameters from 3-15 μm could be activated within the range of the two clinical thresholds, we used the intermediate fiber diameter, 9 μm, to quantify the efficiency and selectivity of SCS. We used the MRG model in the remainder of our analyses.

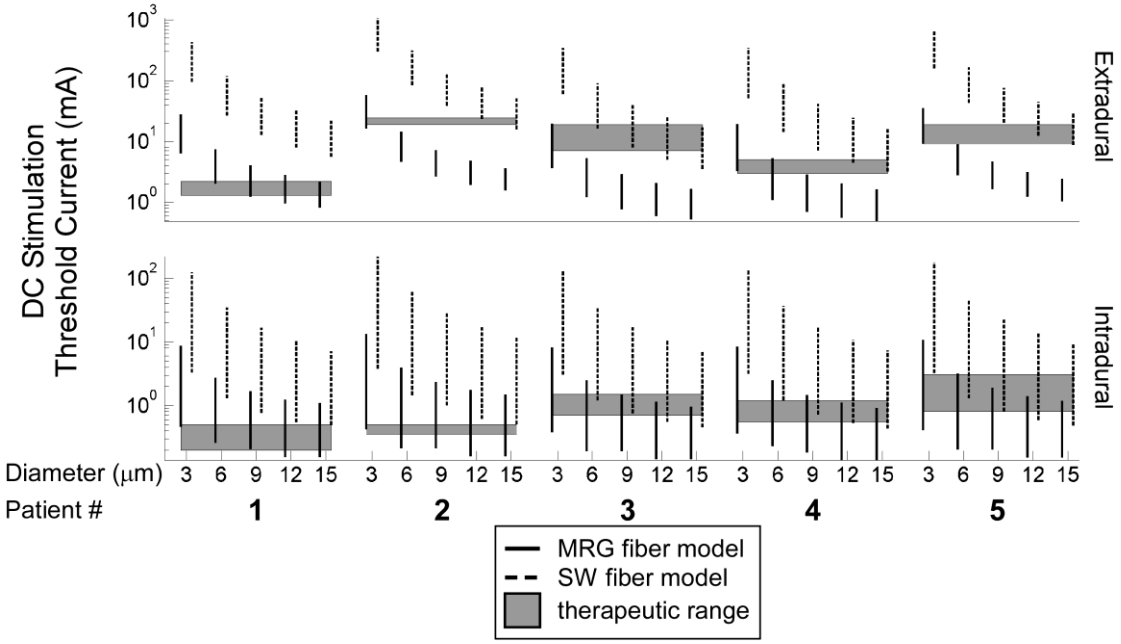

Figure 5.4: Comparing model predictions of stimulation thresholds between MRG and SW models of dorsal column (DC) fibers.
Plotted are distributions of the stimulation threshold currents of DC fibers when the AD-TECH was placed 1 mm above the spinal cord and 1mm above the dura in the intradural and extradural cases, respectively. The therapeutic range is defined as the stimulation amplitudes between the measured sensory and discomfort thresholds.

5.3.2 Power efficiency of intradural SCS

For electrodes positioned along the midline, the calculated access resistance (R_a) of the AD-TECH array was 1,150 Ω (mean, n=5) 1 mm above the dura mater, 165 Ω 1 mm below the dura mater, and 153 Ω 1 mm above the spinal cord. At a given dorsal-ventral position, distributions of R_a across models of individual patients for electrodes at

the three lateral deviations from the midline (0°, −10°, and −20°) were not significantly different from each other, but at a given lateral deviation, distributions of R_a across models of individual patients were significantly different ($p < 0.05$) between the dorsal-ventral positions. Therefore, R_a was sensitive to dorsal-ventral position, primarily between the intradural and extradural locations, and insensitive to lateral deviations.

The reduction of R_a by > 85 % when the electrode was moved from the extradural space to the intradural space, along with the increased proximity of the electrode to the spinal cord, dramatically reduced the power required to activate DC fibers (Figure 5.5). The average power required to activate half of the DC fibers at all six intradural locations was reduced > 90 % compared to epidural SCS at all three electrode locations.

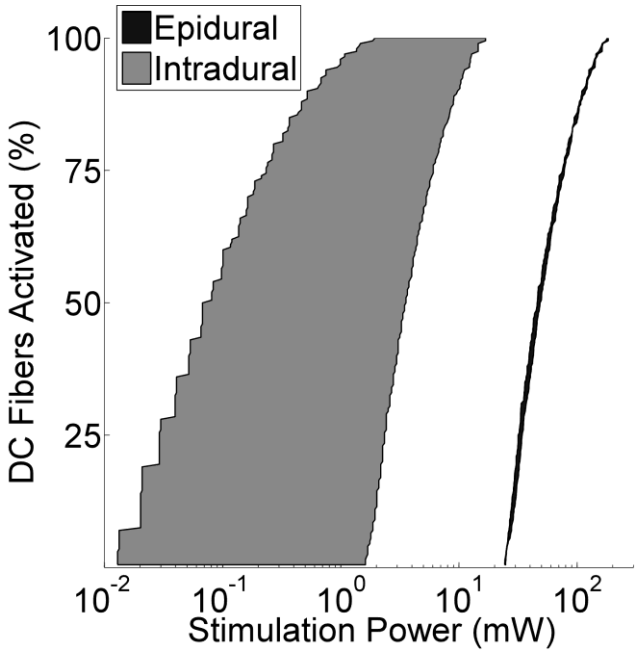

Figure 5.5: Power efficiency of extradural SCS versus intradural SCS.
Average power required to stimulate the dorsal column (DC) fibers in the SCS model of Patient 2. The shaded black and grey areas encompass the range of stimulation powers calculated over the three extradural electrode locations and six intradural electrode locations, respectively.

5.3.3 The selectivity of intradural SCS

The ability to activate selectively DC fibers over DR fibers was sensitive to electrode placement. In both the extradural and intradural cases, distributions of neural-element selectivity (i.e., DC_0) across models of individual patients at 0°, −10°, and −20° from the midline were significantly different ($p < 0.05$) from each other. DC_0 was greatest when the lead was positioned along the midline and declined with increasing displacement of the electrode from the midline (Figure 5.6a). At each of the lateral displacements from the midline, the distribution of DC_0 across models of individual patients was significantly greater ($p < 0.05$) with intradural placement than extradural placement. Thus, DC_0 was greatest when the intradural electrode was located along the midline and closest to the spinal cord.

It is not known how many DR fibers must be activated to evoke discomfort in SCS and whether this number varies from patient to patient. To account for this uncertainty in what constitutes discomfort, we constructed curves of the proportion of DR fibers activated versus proportions of the DC fibers activated (i.e., DC_X). DC_X was greater with intradural placement than with extradural placement when the electrode was located along the midline and closest to the spinal cord (Figure 5.6b).

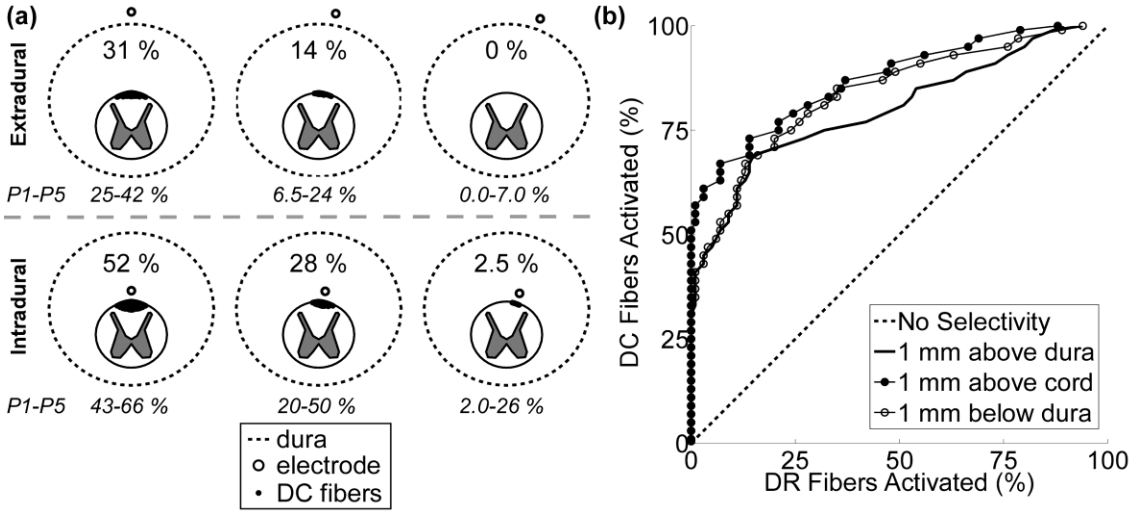

Figure 5.6: The selectivity of extradural SCS versus intradural SCS in model of Patient 5. The maximum percentage of dorsal column (DC) fibers activated with no activation of dorsal root (DR) fibers (DC_0) when the array was placed in the extradural (top row) and intradural (bottom row) spaces at lateral deviations of 0° (left column), −10° (middle column), and −20° (right column). For comparison, the range of DC_0 across all patients is shown below each panel. (b) Curves of the proportion of DC fibers activated versus proportion of DR fibers activated for three different electrode locations along the midline.

Activation of DC fibers in lateral dermatomes at lower amplitudes than required for activation of DC fibers in medial dermatomes was possible by displacing the electrode laterally from the midline. For example, in Patient 1, when the array was positioned along the midline, 1 mm above the cord, DC fibers in L2-L5 could not be activated without first activating DC fibers in S2-S5 (Figure 5.7a). However, when the array was displaced −20° from the midline, 1 mm above the cord, DC fibers in L2-L5 could be activated but not without co-activation of DC fibers in S1 and S2 (Figure 5.7a). Similar results were obtained in Patients 2-5.

5.3.4 The effect of electrode geometry

The performance of five additional tripolar electrode designs (2 LT, 2 TT, and the AT) was tested in the SCS models of Patients 1-5. In the extradural case, LT-1.5, LT-6, TT-1, TT-3, and AT had an average (n = 5) DC_0 of 30 %, 31 %, 27 %, 19 %, and 27 %, respectively. However, the variability in DC_0 across patients was large. For example, LT-6, which performed the best, on average, had DC_0 that ranged from 23-38 %; whereas TT-3, which performed the worst, on average, had DC_0 that ranged from 0-30 % (Figure 5.8a). As a result, the distributions of the selectivities of the five designs were not significantly different from each other in the extradural case.

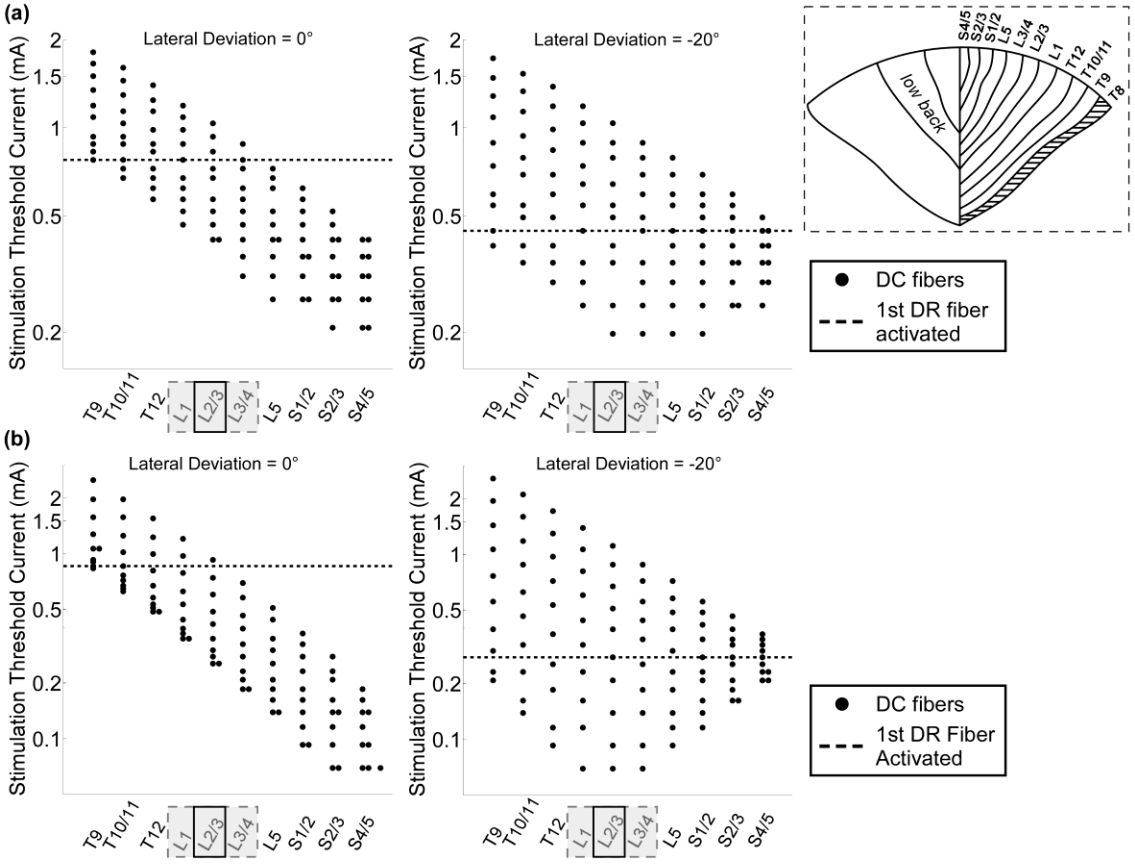

Figure 5.7: Selective activation of dorsal column (DC) fibers in the low back (L2-L5) dermatomes of Patient 1.
(a) Stimulation threshold current of each of the model DC fibers, split by dermatome (see inset), when the AD-TECH array was placed in the intradural space and laterally displaced 0° (left) and -20° (right) from the midline. The shaded area in the inset illustrates where the Aβ collaterals of the DR fibers were located with respect to DC dermatomes at T8. (b) The same as (a), except for the angular tripole electrode geometry. The locations of the paresthesias at the sensory and discomfort thresholds are denoted by the open black rectangles and filled grey rectangles, respectively.

All tripolar electrode designs had distributions of DC_0 in the intradural case that were significantly greater ($p < 0.01$) than the corresponding distributions of DC_0 in the extradural case (Figure 5.8a). Further, in the intradural case, distributions of DC_0 of the electrode designs across models of individual patients were all significantly different

from each other: the AT performed better than the two TTs ($p < 0.01$), and the two TTs performed better than the two LTs ($p < 0.05$). Thus, selectivity in the intradural case, compared to the extradural case, was less sensitive to anatomical variations across patients.

Since the AT had the greatest neural-element selectivity in the intradural case, we also assessed its ability to activate selectively DC fibers in the lateral dermatomes. When the AT was deviated −10° from the midline, it activated DC fibers in four dermatomes, L2-S2, without activation of DC fibers in the other dermatomes; and when further deviated to −20°, the AT activated DC fibers in three dermatomes, L1-L4, without activating DC fibers in the other dermatomes. In SCS for the treatment of chronic low back pain, the target dermatomes are typically L2-L5, thus the AT had the greatest selectivity in targeting the low back dermatomes (Figure 5.7b).

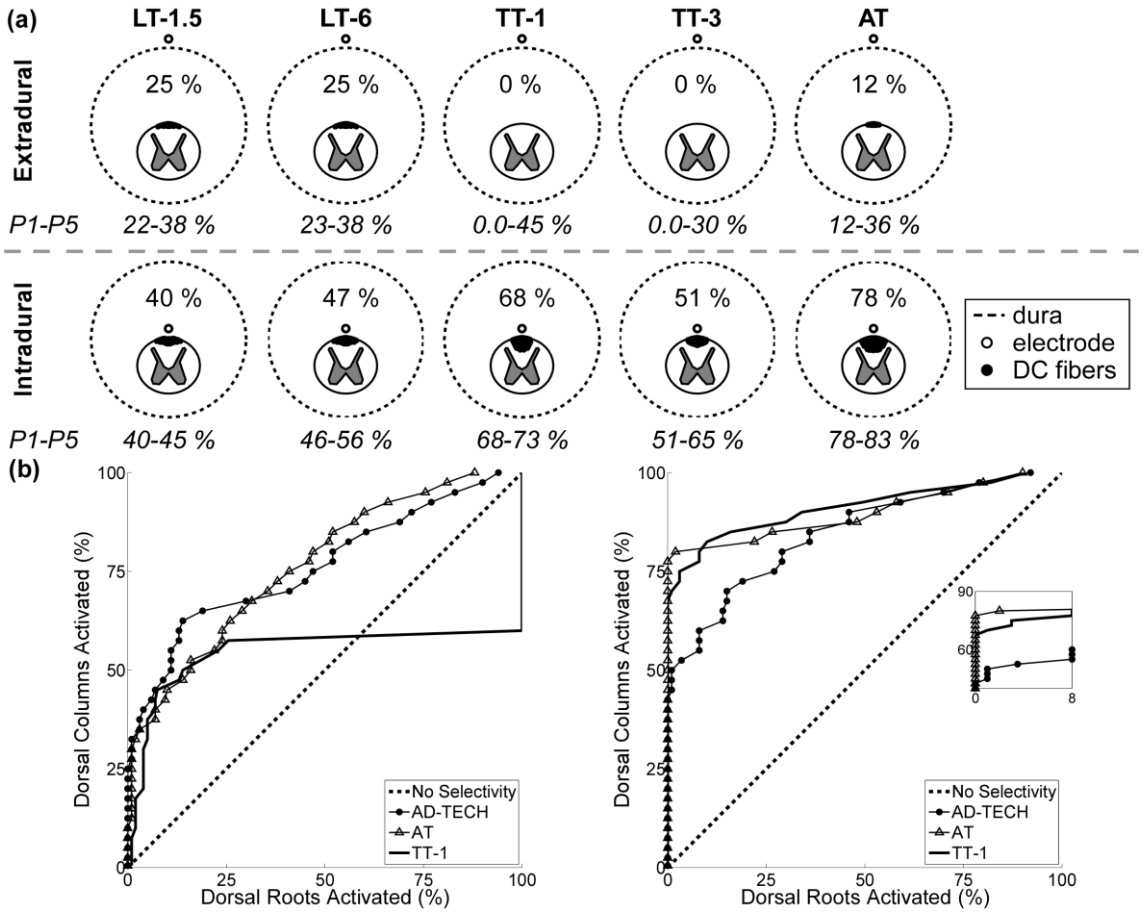

Figure 5.8: Selectivity of five tripolar electrode designs in model of Patient 2.
(a) The percent of dorsal column (DC) fibers activated with no dorsal root (DR) fiber activation (i.e., DC_0) when the electrode was placed along the midline, 1 mm above (top) and below (bottom) the spinal cord. DC_0 is shown above the spinal cord. For comparison, the range of DC_0 across all patients is shown below each panel. (b) Proportion of DC fibers activated versus proportions of the DR fibers activated (i.e., DC_X) for three electrode designs in the extradural (left) and intradural (right) cases. The inset shows a close-up of the curves. LT = longitudinal tripolar, TT = transverse tripolar, AT = angular tripolar, and the number after the hyphen indicates the interelectrode spacing in mm.

5.4 Discussion

We developed a computational model of SCS and quantified the efficiency and selectivity of different electrode designs placed either extradurally or intradurally. Intradural placement dramatically increased stimulation efficiency and reduced the power

required to stimulate the dorsal columns by more than 90%. Intradural placement also enabled activation of a greater proportion of dorsal column fibers before spread of activation to dorsal roots and produced more selective activation of individual dermatomes at different lateral positions. The results suggest that present electrode designs used for extradural SCS are not optimal for intradural SCS, and a novel azimuthal tripolar design increased stimulation selectivity, even beyond that achieved with an intradural paddle array in TT configurations. Increased stimulation power efficiency is expected to increase the battery lives of implantable pulse generators (IPGs), increase the recharge intervals of rechargeable IPGs, and potentially reduce IPG volume. The greater stimulation selectivity with intradural placement may improve the success rate of SCS by mitigating the sensitivity of pain relief to malpositioning of the electrode.

5.4.1 The design of more effective intradural SCS leads

Previous studies of extradural SCS have shown that bipolar and tripolar electrode configurations have greater selectivity than monopolar configurations [46], but the energy required for stimulation increases as the IES decreases [128]. More specifically, models of extradural SCS predict that PERC designs in longitudinal (rostrocaudal) bipolar (LB) and LT configurations have better selectivity than LAM designs in TT configurations [41, 47], although the opposite is observed in practice [129, 152, 153]. LAM designs are less prone to migration than PERC designs [151], and they compress

the dural sac, reducing the distance between the electrodes and the spinal cord, which improves selectivity [172, 173].

Our results corroborate the predictions of previous extradural SCS studies. LT-1.5, LT-6, and the AD-TECH array in a LB configuration, on average, achieved greater DC_0 than TT-1 and TT-3 (Figures 5.6a and 5.8a); and energy requirements increased with decreasing IES. However, the distributions of the extradural DC_0 of the six electrode designs across patients were not significantly different from each other, indicating that patient-to-patient variability in spinal anatomy can significantly impact the performance of the electrode. In the intradural case, the relationship between energy requirements and IES did not change, but each design had greater selectivity than the corresponding extradural case (Figures 5.6a and 5.8a). Therefore, not only is selectivity increased with increasing proximity to the dorsal aspect of the spinal cord, but selectivity with intradural placement is less sensitive to patient anatomical variations.

The AT electrode design had the greatest selectivity in the intradural case (Figure 5.8). To understand why the AT performed best, we examined the centered second difference of the extracellular potentials ($\delta^2\Phi$) across the model fibers for each electrode design, as $\delta^2\Phi$ is proportional to the source driving membrane polarization [39]. Across all six designs, $\delta^2\Phi$ across DC fibers had the same stereotypical triphasic shape, including a primary positive (depolarizing) lobe flanked by two smaller negative (hyperpolarizing) lobes (Figure 5.9a). All six designs also generated a triphasic $\delta^2\Phi$ across DR fibers, except at the boundary between the CSF and the white matter, where the discontinuity in conductivity created discontinuity in $\delta^2\Phi$ (Figure 5.9a), which was expected [41]. Since

no marked differences in the shape of $\delta^2\Phi$ between the designs were observed, we conclude that the superior selectivity of the AT arose from its ability to steer current away from the spinal cord so that $\delta^2\Phi$ decayed more rapidly with distance than it did with the LB, LT, and TT configurations. In other words, the difference in $\delta^2\Phi$ between the DC and DR fibers was greatest with the AT electrode (Figure 5.9b).

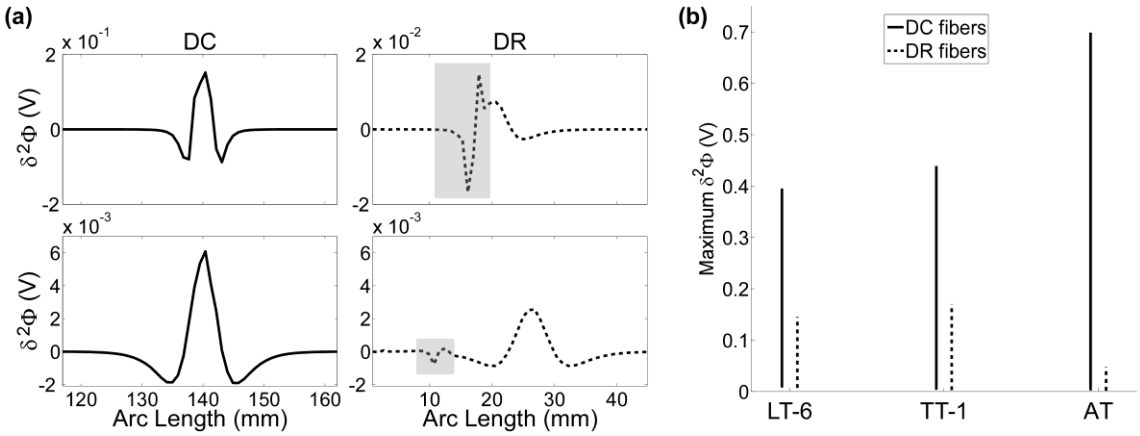

Figure 5.9: The source driving membrane polarization with three different electrode designs.
(a) Examples of the centered second difference of the potentials ($\delta^2\Phi$) along two dorsal column (DC) fibers and two dorsal root (DR) fibers. The grey boxes indicate regions where changes in tissue conductivity caused abrupt changes in $\delta^2\Phi$. (b) The range of maximum $\delta^2\Phi$ across across all modeled DC fibers and DR fibers for three electrode configurations. LT = longitudinal tripolar, TT = transverse tripolar, AT = angular tripolar, and the number after the hyphen indicates the interelectrode spacing in mm.

In addition to efficiency and selectivity, additional factors, such as risk and cost, should also be considered when comparing the performance of PERC and LAM designs. PERC arrays are less invasive than LAM arrays: the former are inserted using a percutaneous needle, while the latter require multi-level laminectomies for placement.

Further, compared to LAM arrays, PERC arrays are less prone to fracture [151] and may be less damaging [158], as the tissue response depends on electrode size [180]. In regards to practical limitations, PERC arrays are more prone to migration and movement than LAM arrays [151, 181]. For example, rotating the AT by ± 10°, ± 20°, and ± 30°about its longitudinal axis reduced the DC_0 from 80 % to 73 %, 58 %, and 47.5 %, respectively. Reductions in pain relief that result from lead migration or movement are problematic because they may lead to greater reoperation rates to replace or reposition the lead [158]. Despite these differences, the long-term health-care costs were similar between the PERC and LAM arrays [158].

5.4.2 Limitations

Two important limitations of the models used in this study require consideration. First we ignored the branching collaterals of the Aβ (DC) fibers. As the Aβ fibers ascend the spinal cord to the gracile and cuneate nuclei in the brainstem, they project smaller diameter collaterals to neurons within the grey matter of the spinal cord [182]. This branching can reduce stimulation thresholds by up to 50 % in SW models of DC fibers [174], and the stimulation thresholds reported in the present study may therefore be overestimated.

The second limitation was ignoring the presence and properties of the electrode-tissue interface (ETI). The filtering effects of the ETI have not been studied in SCS, but they have been studied in electrical stimulation of the brain [78, 80, 81]. The ETI, which is typically modeled as the parallel combination of a distributed resistor and a distributed

capacitor, has a time constant on the order milliseconds. Because typical pulse widths for SCS range from 175-600 μs, the ETI is expected to charge by an appreciable amount during the stimulus pulse, increasing the dynamic load on the stimulator. The rate at which the dynamic load increases depends on the electrical properties of the ETI and tissue, which depend on electrode geometry. Thus, representation of the ETI is recommended for future studies comparing the efficiency of SCS electrode designs.

In addition to model limitations, this study was also limited by experimental variability in the clinical study. Sources of uncertainty included variability in electrode placement and position and variability in the experimental conditions. For example, in Patient 1, intradural stimulation thresholds were assessed before extradural stimulation thresholds, while the order was reversed in Patients 2-5. Because the dura of Patient 1 was punctured before extradural assessment, leakage of CSF might explain why the extradural clinical thresholds of Patient 1 were smaller than those of Patients 2-5 (Figure 5.4). Experimental variability can be reduced in future studies by standardizing all aspects of the clinical procedure and using intraoperative fluoroscopy images to determine more accurately the position of the electrode during stimulation.

5.5 Conclusion

The present study used a computational model of SCS to evaluate quantitatively the performance of intradural SCS for treating chronic pain. Intradural electrode placement markedly reduced energy consumption and improved selectivity of activation of DC fibers in both medial and lateral dermatomes without co-activation of DR fibers.

Further, the results suggest that DC fibers with diameters as small as 3 μm are activated within the therapeutic range of SCS parameters, challenging the notion that only DC fibers with diameters > 9 μm are activated in SCS. More anatomical studies are needed to characterize better the distribution of fiber diameters within the DC so that subsequent modeling studies can more accurately quantify the population of Aβ fibers that correspond to evoking paresthesia and discomfort; and long-term clinical studies are needed to test the predications of our model, understand better the percentage and diameter of neural elements that correspond to comfortable and uncomfortable sensations, and assess the potential therapeutic benefits of intradural SCS.

Chapter 6 : Conclusions and Future Directions

6.1 Conclusions

The goal of this dissertation was to advance our understanding of how electrode geometry can increase the efficiency and selectivity of electrical stimulation therapies. Prior efforts to improve stimulation efficiency focused on decreasing electrode impedance (Z_e) by altering the properties of the electrode and/or increasing the electrode area or perimeter. There is a paucity of work quantifying the effect of electrode geometry on stimulation efficiency, and trial and error experimentation is unlikely to lead to an optimal result. Therefore, model-based design was used as a tool to develop improved electrode designs.

The most efficient electrodes were not always those with the smallest Z_e. In cases where reductions in Z_e did not predict the most efficient design, increases in efficiency were explained by examining the spatial second difference of the potentials ($\delta^2\Phi$). For example, when one electrode, A, was more efficient than another electrode, B, despite A having a larger Z_e than B, the former was more efficient because A, compared to B, had a greater maximum $\delta^2\Phi$ across the target neural elements. However, the electrode design with the greatest maximum $\delta^2\Phi$ was not always the most efficient, indicating $\delta^2\Phi$, by itself, cannot be used to predict stimulation efficiency. Therefore, one conclusion of this work is that analysis of stimulation efficiency requires consideration of both the effect of

electrode geometry on Z_e, which determines how much current is applied per volt, and the effect of the resultant $\delta^2\Phi$ on the applied voltage required to activate the target neural elements.

Model-based optimization was also used to design more selective electrode geometries. Activation of passing axons based on their orientation was achieved using bipolar and tripolar electrode configurations, and activation of terminating axons over passing axons was achieved using an anode displaced from the center of the target region. Bipolar and tripolar electrode designs are used in DBS and SCS for their ability to activate neural elements near the electrode while minimizing activation of more distant non-target elements. The current work improves our understanding of how electrode geometry and polarity can be used to activate neural elements based on their orientation and type. These improvements in selectivity were explained by examining $\delta^2\Phi$ – as well as $\Delta\Phi$ for terminating axons – and selectivity was increased by maximizing the driving force ($\Delta\Phi$, $\delta^2\Phi$) of target neural elements while minimizing the driving force of non-target elements.

Advancing our understanding of the features of electrode geometry that are important for increasing stimulation efficiency and selectivity facilitates the design of the next generation of DBS electrodes. Altering and optimizing electrode geometry and polarity uses existing biocompatible materials, and therefore may help to translate more rapidly new electrode designs into clinical use. Electrodes with greater stimulation efficiency will increase the lifetime of battery-powered IPGs and increase the recharge intervals of RPGs, thereby mitigating the costs and risks of repeated battery replacement

surgeries. Electrodes with greater stimulation selectivity may reduce the sensitivity of clinical outcomes to malpositioning of the electrode.

6.2 Future Directions

This body of work advanced our understanding of how electrode geometry can improve the efficiency and selectivity of electrical stimulation therapies. However, determining the optimal electrode geometries for specific target regions in DBS and SCS remains an opportunity. Designing electrodes that are best suited to different target regions will require more detailed models of electrical stimulation that incorporate the homogeneous and anisotropic conductivity of the tissue and complex geometry of the neural elements. Further, issues, such as safety, physical limitations, and device programming, will need to be considered before the next generation of electrode designs can be implemented.

6.2.1 Improving the Predictive Power of Models of Electrical Stimulation

Accurate modeling of the distribution of potentials in nervous tissue, as demonstrated in Chapter 4, requires accounting for heterogeneities and anisotropies in the conductivity of the nervous tissue [72, 73]. The tissues that compose the spine and nerves are distinct enough to be segmented into regions with relatively homogeneous electrical properties. For example, the spine can be segmented into vertebrae, intervertebral disks,

dura, cerebral spinal fluid (CSF), muscle, fat, and grey and white matter. However, segmentation of the brain is less straightforward, as the boundaries between the grey and white matter are less distinct. With the advent of diffusion magnetic resonance imaging (MRI) in the mid-1980s and recent improvements to image processing algorithms and processing power, computational models are now able to represent the highly heterogeneous and anisotropic conductivity of the brain.

Incorporation of the heterogeneous and anisotropic conductivity of the brain can be broken into two steps. In the first step, an imaging processing algorithm is used to segment an MRI of a person's head into its separate regions: the scalp, skull, dura, CSF, and parenchyma of the brain. The conductivities of the scalp, skull, dura, and CSF are approximately homogeneous and isotropic, and therefore can be modeled using lumped scalar quantities; whereas a tensor field is required to model the conductivity of the parenchyma of the brain. In the second step, diffusion MRI, also known as diffusion-weighted imaging (DWI), is used to calculate the conductivity tensor field. Diffusion tensors are extracted from each voxel of the DW image, and the diffusion tensors, in turn, are converted to conductivity tensors [183]. Subsequently, the images from the MRI and DWI are co-registered, a smooth continuous tensor field is created by interpolating the discrete tensor field between the centers of each voxel, the continuous tensor field is mapped to the nodes of the FEM mesh, and the model is solved as described in Chapter 2.

DWI can also be used to determine the geometry of fibers tracts in the brain, termed tractography, which, as demonstrated in Chapters 4 and 5, can markedly impact

neural activation profiles. There are two types of tractography algorithms: deterministic and probabilistic [184]. Deterministic tractography builds a three-dimensional space curve by specifying a starting location, termed the seed point, and constructing a streamline that is tangent to the largest eigenvectors of the tensor field. Deterministic tractography is less computationally expensive than probabilistic tractography but susceptible to large errors. Errors can arise from identification of false fiber tracts, as a diffusion tensor model cannot resolve fiber crossings or bends [185]; and errors from integration are always present and compound as the streamline is constructed because of imaging noise (e.g., motion artifacts) and the discrete nature of the vector field, which only approximates the rate of change of the streamline in space.

The alternative to deterministic tractography is probabilistic tractography, which constructs streamlines using an orientation density function (ODF) that describes the probability density of fibers orientations in space. Probabilistic tractography begins by constructing a fiber ODF (fODF) that describes the proportion of fibers that course in a particular orientation. An fODF can be constructed by defining a region of voxels, termed a seeding region, and using deterministic tractography at each seed point within the seeding region to construct a population of candidate streamlines. This method has the advantages that it accounts for the sensitivity of streamline construction to the choice of the seed point and can be repeated on multiple images to reduce image noise, but because it uses a tensor model, it cannot resolve fibers crossing or bends.

An fODF can also be constructed using a DWI modality known as high angular resolution diffusion imaging (HARDI) that does not make any assumptions about the

directionality of the fibers [186]. Standard DWI measures diffusion in the three Cartesian directions and is referred to as diffusion tensor imaging (DTI) because the implicit assumption is that diffusion occurs either in the x, y, or z directions at a given location in space. Instead, HARDI measures diffusion in a larger number of directions (typically > 50) distributed across a hemisphere, and is thereby able to resolve fiber bends and crossings. HARDI can be used to construct a diffusion ODF (dODF) that measures the probability of water particles diffusing in a particular direction, and the fODF is constructed from the dODF.

After the fODF has been calculated, statistical methods, such as bootstrapping or Bayesian methods [184, 187] are used to convert the fODF into an uncertainty ODF (uODF) that characterizes the statistical uncertainty of the fiber orientation at each point in space. Streamlines are constructed by starting from a seed point and connecting orientations sampled from the uODF. Probabilistic tractography, compared to deterministic tractography, is able to quantify better the variability in fiber orientations, especially in regions of high uncertainty, where many fibers are crossing and/or bending; but the requirement for multiple iterations makes this method more computationally expensive than deterministic tractography.

Although more detailed models of electrical stimulation have greater predictive power, there is a tradeoff between model complexity and computation time. For example, the computational model of DBS used in Chapters 2-4, although simplified, solved on the order of minutes, allowing us to search a very large parameter space of electrode geometries. However, these models were limited in their ability to predict the effects of

the homogeneous and anisotropic tissue conductivity on stimulation efficiency and selectivity. In contrast, the computational model of SCS in Chapter 5 did account for heterogeneities and anisotropies in the tissue conductivity, and the more complex geometry of the target passing fibers, but computation time was increased from several minutes to 1-2 hours. Because of the increased computational time, only a limited number of electrode geometries were studied. The rate of increase in computer processing power has declined significantly over the past decade, and the use of parallel computing will be necessary to reduce computation time in future models of electrical stimulation.

6.2.2 The next generation of electrical stimulation electrodes

One implication of this work is that there is no global optimal electrode configuration for efficient or selective stimulation of neural elements. In Chapter 3, we saw that decreasing Z_e by increasing the electrode area and/or perimeter does not always produce an increase in stimulation efficiency, as stimulation efficiency depends on $\delta^2\Phi$; and $\delta^2\Phi$ varies significantly depending on the orientation and distance of the neural elements. Chapter 4 expanded the findings of Chapter 3 and demonstrated that selectivity markedly depends on the polarity and geometry of the electrode. And, in Chapter 5, we saw that the optimal electrode configuration for selective activation of target elements in SCS depended on electrode placement, as heterogeneities and anisotropies in the tissue conductivity had a marked impact on $\delta^2\Phi$. Therefore, a wide variety of electrode geometries will be required to deliver efficient and selective stimulation across not only

different electrical stimulation therapies but also across the different target regions in these therapies.

New electrode designs that are regarded as “substantially equivalent” to existing electrode designs will require premarket notification (or 510(k) clearance), whereas all other designs will require premarket approval, which is lengthy and costly process. Since fabrication of a multitude of different electrode geometries is impractical, one seeks an electrode design that can generate a wide variety of electrode configurations without having to change the electrode geometry. This can be accomplished with a high density array (HDA) of electrodes.

HDAs consisting of hundreds to thousands of independent electrode contacts can be programmed in configurations that approximate the potentials of optimal electrode geometries. For example, consider a cylindrical HDA segmented in both the axial and azimuthal dimensions: the electrodes can be used separately to target small volumes of tissue [125] or combined to form macro-electrode geometries (Figure 4.6); or electrodes can be combined in multipolar configurations to limit the spread of current or shape the potential distributions, improving stimulation selectivity [50]. Despite the prospects of HDAs, however, their implementation requires several issues to be addressed.

Risk of tissue damage is one issue that will need to be addressed when implementing HDAs. As an electrode decreases in size, power densities increase, leading to increased heat generation. Heat generation can be mitigated by increasing the thermal conductivity of the insulation surrounding the electrodes (Section 1.2.3), but depending on the stimulation parameters, there will be a limit to how small the electrodes can be

without causing temperatures to increase by more than 1-2 °C (Section 1.2.3.1), which can have profound effects on the brain tissue [188].

The biological heat equation [64] can be used to approximate the temperatures generated in brain tissue during electrical stimulation. Consider a spherical current source in an infinite medium with a homogeneous and isotropic conductivity (σ = 0.2 S/m). To simplify, let us ignore perfusion and metabolic heat production, and assume the temperatures are at steady state. In this case, the solution of the biological heat equation takes the following form:

$$T(r) = 37 + \left(\frac{I}{4\pi}\right)^2 \frac{1}{K\sigma}\left(\frac{1}{r_o r} - \frac{1}{2r^2}\right) \tag{6.1}$$

T is the temperature (in °C); I is the root-mean-square amplitude of the applied current waveform; K is the thermal conductivity (in W/m/°C), which has a median value of 0.525 for brain tissue [64]; and r_o is the radius of the spherical electrode. If we consider a current-regulated waveform consisting of a train of asymmetric rectangular pulses with a short 100 μs cathodic primary phase at 3 mA, followed by a 900 μs anodic secondary phase at 3/9 mA delivered at 130 Hz, then I = 0.36 mA. In this case, peak temperatures in the brain tissue are < 37.01 °C when r_o = 0.635 mm, the radius of the Model 3387, and r_o can be as small as 0.045 mm before temperatures in the brain tissue exceed 39 °C.

Smaller electrodes also produce larger current and charge densities, and therefore have a greater propensity for damaging the electrodes and/or tissue [69]. Damaging

irreversible redox reactions can be prevented by choosing materials that have a high reversible charge injection capacity, and charge densities can be reduced by choosing a smaller pulse width (Section 1.2.3.2). However, there will still be a limit to how small the electrodes can be before they are damaging to the tissue.

In addition to considerations of tissue damage, there is also the issue of the maximum number of electrodes possible with current device designs. DBS and SCS leads are made up of platinum-iridium electrodes inlaid in a hollow polyurethane substrate, and the wires connecting the electrodes to the IPG are bundled within the insulation. We used calipers to measure the diameter of the wires inside an explanted DBS lead and SCS lead. The wires were 0.10 mm in diameter. Because the insulation has an inner diameter of < 1.3 mm, the physical limit of how many contacts can be placed on a lead is < 13.

We ran additional simulations to assess if a 12-electrode array could be configured to closely approximate the potential distributions of the optimal electrode configurations in Chapter 4. The electrodes in the array were approximately 0.9 mm in height and spaced by 0.1 mm, and the neural elements were placed so that the furthest element was < 5 mm from the origin of the model (Figure 4.1). The 12-electrode array achieved RPU (Section 4.2.2) of 77-95 % and 32-39 % in activating neural elements oriented parallel and perpendicular to the electrode shaft, respectively, whereas, recall, the optimal monopolar configurations had RPU of 86-96 % and 25-34% (Figure 4.4), respectively. In addition, the 12-electrode array achieved an AUC (Equation 4.2) of 32 in activating parallel axons of passage (AOPs) over perpendicular AOPs, an AUC of 96 in activating perpendicular AOPs over parallel AOPs, and an AUC of > 87 in activating

parallel terminating axons (TAs) over AOPs. These stimulation selectivities were relatively close to the AUC of the optimal configurations (Figures 4.5 and 4.6). Constructing an n-contact array with greater than 12 electrodes will require new technologies. For example, it is possible to construct an HDA on a flexible substrate [29, 189], such as polyimide, where micron-sized metal traces, rather than wires, are used to connect the electrodes to the IPG. Although these types of electrode designs are not currently FDA approved for implantation in the spine or brain, they are a promising technology for the next generation of stimulation electrode designs.

Finally, there is the issue of programming the electrical stimulation device. The space of possible pulse widths, amplitudes, and frequencies is vast. For example, the Medtronic Activa Model 37601 (Medtronic Inc., Minneapolis, MN, USA), in voltage-regulated mode, has 211 amplitudes, 40 pulse widths, and 57 frequencies, which amounts to 481,080 possible choices of stimulation parameters; and implementation of HDAs will greatly increase the number of possible electrode configurations. To prevent the programming of the device from becoming an intractable process, it is important to synthesize the concepts of efficient and selective stimulation so that the patients, clinicians, and corporate representatives understand how to select the optimal electrode geometries for a given therapy and target region. We envisage a graphical interface where the programmer inputs the type, orientation, and extent of the target neural elements; and the system displays the potential optimal electrode configurations. Therefore, the programmer does not need to understand the theory behind why these electrode

configurations are optimal, and he or she can alter the optimal solutions in a constrained parameter space surrounding the expected optimal solution.

Appendix A Design Considerations for Recording Electrodes

A.1 Introduction

The flow of ions across the membrane of an electrically excitable cell generates a distribution of potentials in the extracellular space that can be recorded with an electrode. The spatiotemporal characteristics of the potentials depend on the cellular source of the transmembrane current, so a wide spectrum of signals exists: potentials recorded from neurons in the brain are referred to as an electroencephalogram (EEG) when recorded from the scalp and as local field potentials (LFP, many cells) or single unit activity (one cell) when recorded from within the brain; and potentials recorded from axons in the CNS and PNS are referred to as an electroneurogram (ENG), in general, and more specifically as an compound action potential (CAP) when the electrically activity is synchronized.

A recording electrode must satisfy three design criteria to be effective. First, a recording electrode must discriminate the target neural signal, both spatially and temporally, from non-target neural signals. In some cases, the ability to discriminate the neural signal depends primarily on the proximity of the electrode to the cellular source, but in other cases (e.g., discrimination of a single unit), the geometry of the electrode is also important. Second, the recording electrode must minimize both intrinsic and extrinsic forms of electrical noise so that the target signal can be recorded with a high

signal to noise ratio (SNR). And third, a recording electrode should produce minimal tissue damage from the implantation and residence of the electrode.

A.2 Discrimination of the target neural signal

The electric potentials generated in a volume of tissue by biological current sources and sinks can be discriminated based on spatial and temporal characteristics. Spatial discrimination is achieved by selecting the appropriate location, geometry, configuration, and material of the electrode based on the signal properties; while temporal discrimination is achieved through filtering (or signal processing) of the signal based on its amplitude or spectral properties. Because the latter does not depend on the electrode design, it will be covered only briefly.

A.2.1 Spatial discrimination

The reciprocity theorem, derived from Green's theorem in classical electromagnetism [190], can be used to understand how an electrode spatially discriminates electric signals arising from neural sources. Consider an arbitrary conducting volume with electrical properties that are independent of any generated potentials. If the volume has no sources on its surface, then the reciprocity theorem states the potential generated at one location, P_1, from the passage of a unit current at another location, P_2, is equivalent to the potential generated at P_2 from the passage of a unit current at P_1. In other words, there is equivalence between the potential impressed upon an electrode from a unit source in neural tissue and the potential generated at the location

of the source by an electrode releasing a unit amount of current. It then follows that spatial discriminability of a recording electrode can be studied by analyzing the potentials it generates when acting as a source.

In neural prostheses, such as BMIs, where the goal is to differentiate the electrical activity of individual neurons from non-target electrical activity in the surrounding tissue, one requires an electrode that – when acting as a source – generates potentials that decay rapidly with distance. The potentials of an arbitrary source decay at a rate ($-\nabla\Phi$) that is proportional to $\vec{J}$ (section 7.2.2.1). The magnitude of $\vec{J}$ increases with increasing proximity to the source, and the geometry that minimizes the surface area of a given unit of volume is a sphere. Therefore, the electrode that theoretically maximizes $-\nabla\Phi$ is a spherical point source whose potentials decay proportional to 1/r (Figure A.1). This explains why electrodes that most resemble a point source; for example, an insulated microelectrode with an exposed sharp tip (Figure 1.1a/c), are preferred when recording the electrical activity from single units [191].

In some cases, it is also desirable to have a recording electrode that can measure the aggregate electrical activity of many neurons distributed throughout a volume of tissue. For example, in DBS, simultaneous recording of the electrical activity within the targeted tissue may provide an objective metric for optimizing the selection of stimulation parameters [97, 192]. These types of recordings require a large (macro) electrode (e.g., Figure 1.1e) whose dimensions are on the same order as the length scales being targeted. As the dimensions of an electrode increase, $\left|\vec{J}\right|$ decreases, so the

potentials of larger electrodes decay much more gradually than 1/r (Figure A.1). Thus, as a general principle, the ability to discriminate spatially larger volumes of tissues increases with electrode size, and the shape of the volume can be tailored by altering the electrode geometry.

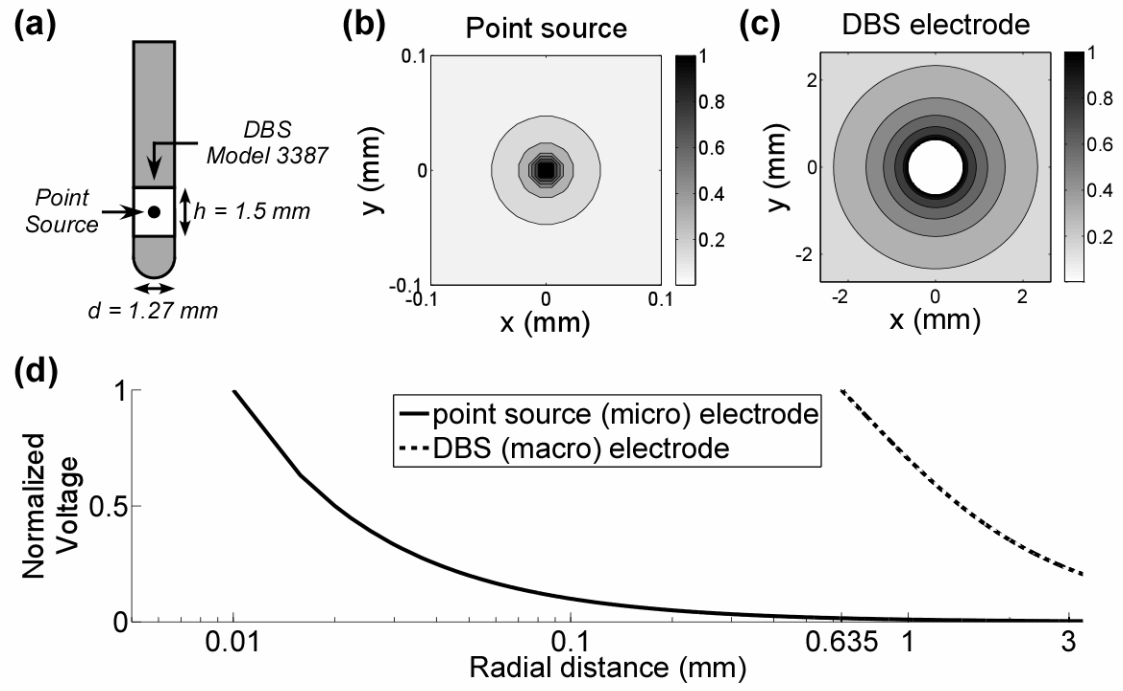

Figure A.1: Using the reciprocity theorem to assess the effect of electrode geometry on the ability to discriminate spatially different volumes of tissue.
(a) A point source and the distal most contact on the Model 3387 array (Medtronic Inc., Minneapolis, Minnesota) are used to inject separately a unit current into an infinite medium with a homogeneous and isotropic conductivity of 0.2 S/m [40]. (b) Filled contours of the normalized potentials for the point source. (d) The same as b, except for the 3387 electrode. (d) The potentials impressed upon the electrode for a unit current at increasing radial distances from the origin, normalized by the corresponding maximum value. Note: The potentials of the point source were sampled ≥ 10 μm from the origin.

A.2.2 Temporal discrimination

The temporal characteristics of transmembrane currents during the AP vary across different types of electrically excitable cells. APs generated in the axon and soma of neurons have a short duration (approximately 1 ms), so large filter passbands with high cutoffs, typically between 100 Hz and 5-10 kHz, are used to discriminate an ENG, ECAP, or a single unit [193-195]. However, APs are not the only electrical signals that can be recorded. In neurons, when an AP reaches the axon terminal, neurotransmitter is released and bound to ligand-gated ion channels on the soma and/or dendrites of the postsynaptic neuron. The subsequent flow of ions elicits an electrical event known as a post synaptic potential (PSP). Compared to an AP, a PSP is longer in duration, lasting anywhere from 1 millisecond to 100s of milliseconds, and it can be temporally discriminated from an AP by filtering between 0.5-500 Hz [196, 197]. PSPs and other relatively long lasting signals (e.g., calcium spikes) are predicted to be the origins of LFPs [196], so temporal discrimination – regardless of electrode geometry – can be used to differentiate LFPs from single units.

A.3 Reduction of electrical noise

A recording electrode should be designed to minimize intrinsic and extrinsic forms of electrical noise, as well as forms of noise that arise from the motion of the electrode and/or tissue.

A.3.1 Intrinsic electrical noise

Intrinsic electric noise can be classified into four types: thermal (Johnson or white) noise that arises from the random (Brownian) motion of the charge carriers, flicker (or pink) noise that arises from the changing energy states of the charge carriers, shot noise that arises from the discrete nature of the charge carriers, and generation-recombination (G-R) noise that arises from the statistical generation and recombination of charge carries. All four types of noise have a marked effect at the nanoscale, especially shot noise and G-R noise when recording signals from single ion channels, but at the microscale (single neuron level) and beyond, only the former two have an appreciable effect.

White noise can be reduced by altering the electrical properties of the electrode. Consider a noise source, consisting of a voltage source in series with a noise-generating resistor (R_N), attached to a load (Z_e) that does not generate noise. It can be shown that the root-mean-square voltage across Z_e (V_{white}) obeys the following equation:

$$V_{white} = \left(4k_B T R_N \int_0^\infty Z_e(f)\,df \right)^{1/2} \tag{A.1}$$

where k_B is the Boltzmann constant, and T is the absolute temperature of the circuit [198]. We see from Equation A.1 that V_{white} can be reduced by reducing the Z_e of the recording electrode.

Z_e can be reduced in three ways (section 1.3.1.2): by applying a Faradaic electric coating, by roughening the electrode surface, and by increasing the electrode dimensions. All of these approaches can have a marked effect on reducing Z_e, and thereby V_{white}, but with recording electrodes, one should use caution when altering the electrode dimensions. For example, increasing the A of a microelectrode reduces its V_{white} but also reduces the ability to discriminate spatially the electrical activity of single units. Therefore, there is tradeoff between spatial discrimination and noise reduction with microelectrodes, and this is typically minimized by selecting microelectrodes with impedances between 0.1-100 MΩ [191].

Pink noise has an inverse dependence on frequency (f), so unlike white noise, it is not equally present at all frequency ranges (i.e., broadband). Pink noise can be reduced by low pass filtering the recorded signal, but because its effects are independent of Z_e, it is unaffected by electrode design.

A.3.2 Extrinsic electrical noise

Electrical noise that originates outside the neural tissue is termed extrinsic noise. External sources of electromagnetic radiation include atmospheric disturbances, such as solar flares and lighting discharges; manmade devices, such as power lines, lighting fixtures, and electrical equipment; and other electrically excitable tissues in the body, such as muscle and cardiac tissue. Although these noise sources are external to the tissue, they can be minimized with certain techniques.

Extrinsic noise can be reduced by subtracting it from the recorded signal using two or more electrodes in a multipolar differential configuration. The simplest example is a bipole. In a bipolar recording, the signal recorded with one electrode (the negative pole) is subtracted from the signal recorded with the second electrode (the positive pole). Noise, of course, can never be completely removed, but it can be attenuated by choosing electrodes that record similar noise waveforms. We know the ability of the electrode to record a signal depends on its geometry (section A.2.1) and Z_e (section A.3.1), so contacts on the bipole should have a matching geometry and impedance. Further, as the distance between the electrodes decreases, both the recorded signal and recorded noise become increasingly similar. Therefore, the bipolar pair should be close enough in proximity that the noise recorded is similar, but not so close that the target signal is also subtracted.

There are instances where use of a multipolar configuration alone is not effective. For example, raw ENG signals are typically on the order of a few μV [194], and raw EMG signals are typically on the order of a few mV [199]. Because the nerve and muscle are in close proximity, the signal to noise ratio is small, and subtraction reduces the neural signal more than the noise. In these instances, insulation and/or electrical shielding can help increase the SNR (Figure A.2).

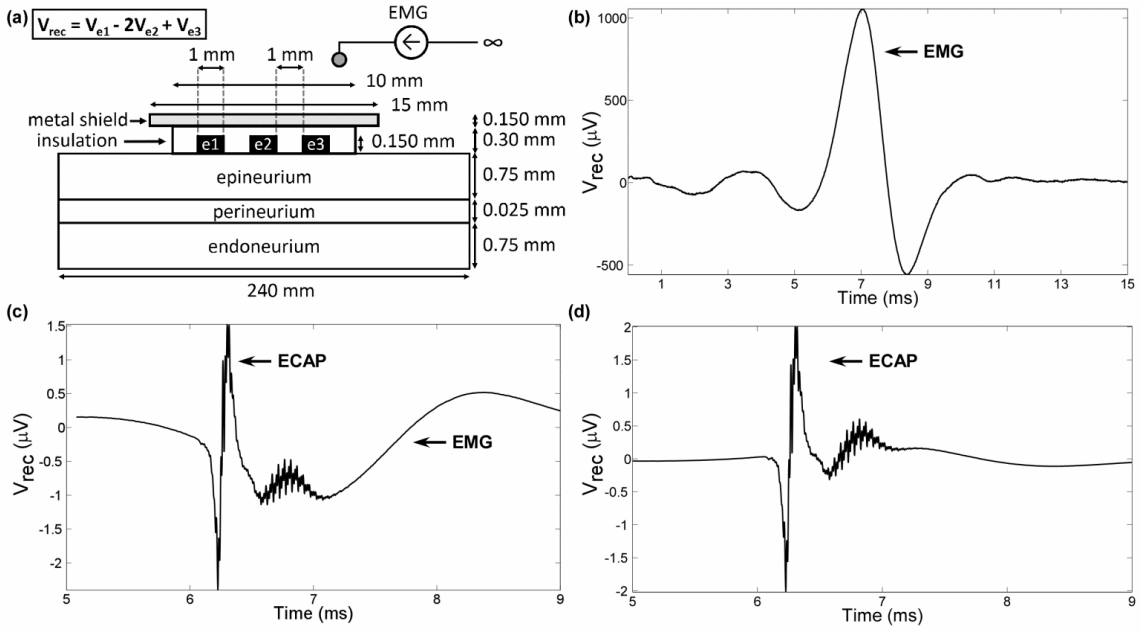

Figure A.2: Reducing extrinsic noise with a tripolar recording electrode.
(a) A population of model axons [85] is distributed within a nerve, action potentials (APs) are initiated at one end of the nerve, and the resulting ECAP is recorded using a tripolar configuration of three cylindrical electrodes. Extrinsic noise is added by placing a current source that emulates an EMG signal in close proximity to the recording electrodes. Plotted are the recorded responses when the electrodes are (b) neither insulated nor shielded, (c) insulated but not shielded, and (d) both insulated and shielded. The simulations in (a) included 100 axons randomly distributed within an axisymmetric finite-element method model of a nerve. The axons were split into two sub-populations whose diameters were drawn from a normal distribution: 50 axons with $\mu = 2.5$ μm and $\sigma = 0.3$ μm and 50 axons with $\mu = 10$ μm and $\sigma = 1.25$ μm. The model dimensions (not drawn to scale) were representative of the sciatic nerve of a cat [200], and the conductivities of the neural tissue were taken from published values [201].

In peripheral nerve recordings, insulated tripolar configurations that record $\Delta^2\Phi$ between its electrodes are used to attenuate extrinsic noise. The insulation helps by constraining the flow of charge between the electrodes and nerve. Because sources outside the insulation generate potentials that decay linearly from one end of the constrained space to the other, while the potentials arising from within the nerve do not, the tripole works by primarily rejecting extrinsic noise. Of course, towards the edges of

the insulation, the potentials beneath the electrodes are no longer linear, so as a general design principle, the distal electrodes should be sufficiently far from the edges [202, 203].

In addition to insulation, the SNR can be further increased by electrically shielding the electrodes with a highly conducting metal material – and grounding that material, if possible. Metals are typically 7-8 orders of magnitude less resistive than neural tissue so external currents are diverted around and away from the recording contacts. Although shielding is not currently used in implantable devices, recent work has shown that it can reduce extrinsic noise as much as 80 % [204].

A.3.3 Motion artifact

The electrode and surrounding tissue are never truly at rest due to disturbances from physiological processes, such as the cardiac cycle, the respiratory cycle, and muscle contraction. For example, in rats, brain micromotion relative to a stationary implant can be as large as 30 μm during cardiac and respiratory cycles [205]. Movement of the electrode and surrounding tissue relative to each other alters the distribution of charge carriers on either side of the ETI. Since the potential gradient across the ETI (i.e., the half-cell potential) depends on the effective concentrations (activities) of the charge carriers, motion-induced fluctuations in the half-cell potential give rise to another source of extrinsic noise termed motion artifact.

Motion artifact can be reduced by stabilizing the charge distribution on either side of the ETI. This cannot be accomplished with polarizable electrodes, such as those made

from the noble metals (e.g., Pt, Au, Ir, etc.), because their half-cell potentials depend on the distribution of freely moving charge in the surrounding tissue. However, this can be accomplished with non-polarizable electrodes, where charge is transferred between the electrode and a relatively insoluble layer, because the interface is stable despite movement of the electrode or tissue. One example is the silver/silver-chloride (Ag/AgCl) electrode, which is typically used as a surface electrode for recording biopotential signals [206]. Ag/AgCl surface electrodes not only mitigate motion artifact from skin movement with respect to the electrode, but they can also be recessed and filled with a conductive fluid/gel to further mitigate movement of charge at the ETI [206]. Ag/AgCl is toxic within the body [207], so biocompatible materials, such as PtIr, that have both polarizable and non-polarizable behavior are recommended to reduce motion artifact in implanted electrodes.

In cases where the electronic noise and signal occupy two separate bandwidths, noise can be further reduced through the use of electronic filtering. For example, motion artifacts typically occupy a bandwidth of < 5 Hz, so motion artifacts can be reduced by filtering, independent of the electrode geometry and configuration, and still preserve most or all of the energy in the target signal.

A.4 Designing non-damaging recording electrodes

The input impedance of the recording instrumentation (i.e., electrode + amplifier) is typically many orders of magnitude larger than the lumped impedance of the tissue. As a result, recordings electrodes operate under very low current density conditions, and

irreversible electrochemical reactions that degrade the electrode and/or damage tissue do not occur. Yet, implantation and presence of the electrode elicits a passive tissue response that may degrade the performance of the electrode, so whether for recording or stimulation purposes, implanted electrodes must mitigate the passive tissue response.

A.4.1 The passive tissue response

Neural tissue is displaced during implantation, severing capillaries, extracellular matrix (ECM), and glial and neuronal processes. As blood-borne cells and proteins enter the tissue, the wound healing process is initiated. Hemostasis occurs within the first seconds to hours, where the formation of a clot prevents further bleeding and spread of pathogens, and molecules within the clot signal the start of the inflammation process [208]. Within the next hours to days, the inflammation process clears the cellular debris, contains and neutralizes the injury-causing agent (i.e., the electrode), and mitigates further damage to the tissue [209]. In the CNS, this is mediated by microglia and astrocytes, and in the PNS and muscle, this is mediated by leukocytes and macrophages [208]. After several days, the inflammation process subsides and transitions into a process of repair that lasts for days to weeks.

Axons and tissue in the PNS can regenerate to a significant degree, as long as the soma of the axon remains viable and the perineurium and epineurium remain intact [210]. In more severe cases, where disruption of the endoneurium and/or perineurium results in the rupturing of the blood-nerve barrier, extensive fibrous ECM (i.e., fibrosis) is required

to repair the damaged tissue [210]. Neurons and tissue in the CNS, however, do not regenerate. Astrocytes, recruited in a process known as gliosis, form a boundary (or glial scar) around the damaged tissue. The glial scar limits the spread of inflammatory cells and aids in the repair of the blood-brain barrier [211, 212], but it also inhibits the growth of new axons and signals the degradation of ECM [208]. For up to several months, the glial scar encapsulating the electrode increases in density [213], and a similar response is expected for fibrous scar tissue in the PNS [214].

Scarring both helps and hinders the performance of a recording electrode. Scar tissue has a ρ of 5-20 Ω-m [127], whereas brain tissue has a ρ of 3.3-5 Ω-m [77]. Indeed, a greater ρ leads to a greater voltage drop across the scar tissue – as $\vec{J} \cdot \rho = -\nabla\Phi$ – but because the electrode is encapsulated by the tissue, a distributed voltage divider is created that helps by increasing the amplitude of the recorded signal [215, 216]. Scar tissue, however, also limits the proximity of the electrode and target elements. For example, the glial scar surrounding a microelectrode typically has a thickness of 5-75 μm, although it can be as thick as 250 μm [217]. Because recording signals from a single neuron requires that the electrode lie within ~ 100-200 μm of the active neuron (Figure A.1d), the adverse effect of scarring on the recorded signal can be greater than its helpful effect (Figure A.3).

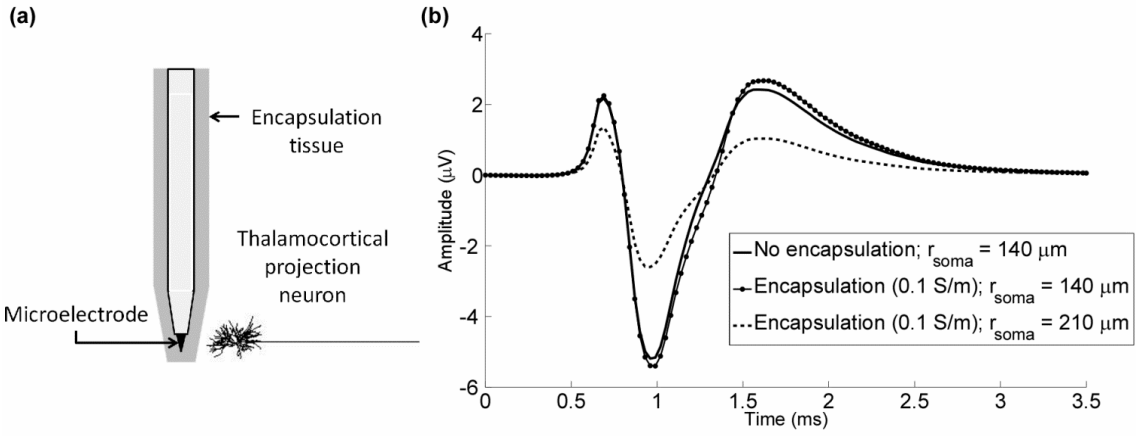

Figure A.3: The effect of the passive tissue response on microelectrode recordings of single units.
(a) An insulated microelectrode with an exposed sharp tip (area ~ 324 μm^2) is placed in grey matter and used to record the electrical activity of a thalamacortical projection neuron [70]. (b) Single unit recordings taken when no encapsulation tissue is present and the (soma of the) neuron is 140 μm from the electrode surface, when 50 μm thick encapsulation tissue is present and the neuron is 140 μm from the electrode, and when 100 μm thick encapsulation tissue is present and the neuron is 210 μm from the electrode. For the simulation in (a), the grey matter had a conductivity of 0.2 S/m [40], and the encapsulation tissue had a conductivity of 0.1 S/m [77]. The recorded potentials were calculated by numerically solving a single reciprocal problem with the finite element method [216].

The electrical effects of scarring on the surrounding tissue stabilize after several weeks [218]. In instances where the scarring is minimal, the signal amplitude declines, but not enough to substantially degrade the recording performance [219]). Yet, recording failures still occur. In these instances, recording failures are better explained by a local neurodegenerative state surrounding the electrode – characterized by neuron loss, dendrite loss, and axon pathology – that is believed to result from chronic inflammation [220]. Thus, the chronic inflammatory response can also be deleterious to the performance of the recording electrode.

A.4.2 Mitigating the passive tissue response

In the CNS, the overall magnitude of glial activation is dependent on the extent of damage to the blood-brain barrier and tissue [212]. Certainly, the blood-brain barrier and tissue incur damage during implantation, but damage also results from the residence of the electrode within the tissue, as movement of the electrode and tissue causes tissue compression and tearing [221]. The same is also expected to be true in the PNS [214, 222]. Therefore, damage incurred acutely during implantation should be distinguished from chronic damage incurred while the electrode resides in the tissue.

The acute response of the tissue to implantation depends on the geometry and surface texture of the electrode [180, 217]. Electrodes with larger cross-sectional areas and rough textures (i.e., sharp edges) have a more severe initial response than smaller electrodes with smooth surfaces [180], so the acute response of the tissue can be mitigated by using smaller electrodes with smoother surfaces. This is only advantageous, however, as long as altering the geometry and surface texture of the electrode does not degrade its performance. Recall, reducing the size of a recording electrode increases the amplitude of white noise (section A.3.1), while at the same time decreasing its ability to record activity from large volumes of tissue (section A.2.1); and reducing the size of a stimulation electrode increases Z_e, which decreases its efficiency (section 1.3.1.2).

Unlike the acute response, the chronic response of the tissue to the presence of the electrode is independent of its geometry and surface texture [180, 217]. One apparent influence on the chronic tissue response is the large disparity between the mechanical

properties of the rigid electrode substrate, typically silicon, and the soft neural tissue. For example, silicon has an elastic modulus of ~ 200 GPa [223], while brain tissue has an elastic modulus of 6 kPa [224]. Therefore, when the electrode or tissue moves (e.g., during brain micromotion), the large mismatch in stiffness has the potential to generate mechanical forces that deform and tear the tissue [221].

The mismatch in stiffness between the electrode and tissue can be reduced by applying a conductive polymer coating to the electrode surface. Two widely used conductive polymers are polypyrrole (PPy) and poly (3, 4-ethylenedioxythiophene) (PEDOT) because of their many advantages in addition to reducing mechanical stress. PPy and PEDOT are stable, biocompatible [225, 226], and support the growth of neurons and neurites [227]. In addition, these polymers can also be used to decrease Z_e by roughening the electrode surface. – PEDOT, for example, has been used to decrease the Z_e of gold microelectrodes by 1-2 orders of magnitude [228]. Because surface roughening does not affect the macroscopic dimensions of the electrode, conductive polymer coatings reduce mechanical stress on the tissue, while at the same time improving the SNR by reducing V_{white} [218, 228].

Another origin of the chronic tissue response is persistent inflammation. Microglia, macrophages and other inflammatory cells clear foreign and necrotic debris at the site of implantation. The electrode, also viewed as a foreign body, is nondegradable and too large to undergo phagocytosis, so the macrophages form giant multinucleated cells that continuously release degradative agents, such as superoxides and free radicals, into the tissue [27, 221]. This process, known as “frustrated phagocytosis”, damages both

the foreign body and the surrounding tissue, and is an additional potential explanation for why neurons and dendrites are lost, despite stabilization of the glial scar [220].

There are passive and active strategies for reducing the inflammatory response. Passive strategies attempt to reduce inflammation by preventing the adsorption of non-specific proteins and inflammatory cells on the electrode surface. Examples of this include pre-treating the electrode with cells or proteins, such as albumin, that elicit little to no inflammatory response, or by coating the electrode with polymers, such as polyethylene glycol (PEG), that resist protein adsorption [229]. Passive strategies are straight-forward and simple, but their performance in vivo is still inconclusive [229]. Active strategies, in contrast, attempt to reduce inflammation by using the electrode to deliver anti-inflammatory agents, including dexamethasone (DEX), heparin, and alpha melanocyte-stimulating hormone. Agents can be delivered via diffusion from polymer coatings and hydrogels, such as PPy [230] and sodium alginate [231], respectively, or via dissolution from biodegradable coatings, such as poly lactic acid (PLA) [232]. These strategies, although more complex, offer fine control over the presentation and kinetics of immunomodulatory agents.

A.5 Future Directions

Creating stimulation electrodes that are efficient, selective, and non-damaging requires the development of new technologies. Vertically aligned carbon nanofibers (CNF) arrays are of one the emerging technologies that show great promise in increasing stimulation efficiency by reducing Z_e. CNF arrays form a highly porous surface area that

is freely accessible to charge. Unmodified, CNF arrays have a c_{dl} of ~0.4 mF/cm^2, which is greater than the c_{dl} of conventional noble metal electrodes (~ 20 μF/cm2) [80], but less than the c_{dl} of PtIr electrodes (~0.6 mF/cm^2) used in therapies, such as DBS and SCS [233]. However, when modified with a coating of PPy, CNF arrays have a c_{dl} that can be as large as 100 mF/cm^2 [233], and as a result, they have the potential of being more efficient than PtIr electrodes [234]. The in vivo biocompatibility of CNF arrays is still inconclusive, so their future success depends on continuing research [233, 235, 236].

As fabrication techniques improve, high density arrays (HDAs) consisting of hundreds to thousands of electrodes will emerge. HDAs show great promise in increasing stimulation selectivity: electrodes can be used separately to target small volumes of tissue [125] or combined to form macro-electrode geometries, or electrodes can be combined in multipolar configurations to shape the generated fields [50]. Yet, implementation of HDAs will have some issues. As electrodes decrease in size, greater power densities and charge densities will lead to increased heat generation and the propensity for tissue damage, respectively [69]; and as the number of electrodes increases so will the difficulty in programming the device.

Emerging technologies also hold great promise for creating more effective recording electrodes. There have been considerable advancements over the past decades in increasing the discriminability and noise rejection capabilities of recording electrodes, but many challenges still remain for minimizing the tissue response. The biggest of these challenges is reducing the chronic inflammatory response, as it has a marked impact on neuron viability [220, 231] and thereby the long-term stability of the recordings [16].

The majority of emerging technologies focus on reducing neuron losses by eliminating inflammation, but neuron losses can also be reduced by promoting their growth and survival using neurotrophic factors. Designs that employ this strategy are known as neurotrophic electrodes, which have been studied for over two decades.

The most studied neurotrophic electrode is the cone electrode, consisting of conical hollow glass tube containing metal wires and a neurotrophic medium that promotes the growth of dendrites and axons [237, 238]. Such a design is advantageous because it brings neurites in close proximity to the electrode, while at the same time isolating the neurite from potentially harmful inflammatory factors. Neurotrophic electrodes have had much success, particularly in humans, where they have been able to isolate single units for over four years [239]. However, despite remarkable stability, neurotrophic electrodes are not widely used because their relatively large size (of hundreds of microns) limits their ability to isolate multiple neurons in close proximity. As technology progresses, miniaturization of the substrate and wires will allow for multiple isolated cavities to be used to spatially discriminate many signals at once.

Appendix B Finite Element Method Implementation of the Electrode-Tissue Interface in a Model of Electrical Stimulation

B.1 Linear form of Equations

The weak form of Equation 2.1 was obtained by multiplying both sides of Equation 2.1 by a weighting function (w), integrating over the domain Ω and its boundary Γ, and using the divergence theorem to represent the volume integral of the divergence of $\vec{J}$ over Ω as the flux of $\vec{J}$ over its boundary Γ.

$$\int_{\Omega} \nabla w \cdot (\sigma \cdot \nabla \Phi) d\Omega + \int_{\Gamma_{ETI}} w \hat{n} \cdot \vec{J} d\Gamma = 0 \tag{B.1}$$

Where σ is a conductivity tensor, Γ_{ETI} is the boundary of the ETI, ρ is the radial distance, and ρ_e is the radius of the electrode and its shaft.

We used the Galerkin method to approximate solutions of the boundary-value problem based on its weak formulation. The solution and weighting spaces were discretized using 4-node quadrilateral elements with bilinear shape functions shown below:

$$\Phi^h(z,\rho) = \sum_{a=1}^{n_{eqns}} N_a(z,\rho) d_a \tag{B.2}$$

$$N_a(z,\rho) = \frac{1}{4}(1+\xi_a\xi)(1+\eta_a\eta) \tag{B.3}$$

Where, the superscript h denotes an approximation, n_{eqns} is the number of shape functions on the quadrilateral element, ζ and η are the variables, z and ρ, mapped onto the bi-unit square domain, and d_a and c_a are arbitrary constants. Application of (B.2) to (B.1) yielded the following system of equations:

$$M\dot{d} + (K+H)d = F \tag{B.4}$$

$$K = \int_{\Omega} \nabla N_A \cdot \sigma \cdot \nabla N_B d\Omega \tag{B.5}$$

$$M = \int_{\Gamma_{ETI}} N_A \cdot c_{dl} \cdot N_B d\Gamma \tag{B.6}$$

$$H = \int_{\Gamma_{ETI}} N_A \cdot r_f^{-1} \cdot N_B d\Gamma \tag{B.7}$$

$$F = \int_{\Gamma_{ETI}} N_A \cdot r_f^{-1} \cdot \Phi_{stim} d\Gamma \tag{B.8}$$

Where, K is the stiffness matrix; and M, H, and F are sparse matrices that contain components arising from the ETI. M contains contributions from the non-Faradaic, capacitive current, and H and F contain contributions from the Faradaic, resistive current.

B.2 Nonlinear form of Equations

(B.5) - (B.8) was linearized using the Newton-Raphson (NR) method, which yielded:

$$R + \frac{\partial R}{\partial d}\Delta d = 0 \tag{B.9}$$

$$R = F_{ext} - F_{\text{int}} \tag{B.10}$$

$$\frac{\partial R}{\partial d} = \frac{\partial F_{ext}}{\partial d} - K - \frac{\partial H}{\partial d} - \frac{\partial M}{\partial d} \tag{B.11}$$

$$F_{ext} = \int_{\Gamma_{ETI}} N_A \cdot r_f^{-1} \cdot \left(\Phi_{n+1}^{i}\right) \cdot \Phi_{stim} d\Gamma \tag{B.12}$$

$$\Phi_{n+1}^{i}(z,\rho) = \sum_{c=1}^{n_{eqns}} N_c(z,\rho) d_{n+1}^{i} \tag{B.13}$$

$$F_{\text{int}} = M\left(\frac{\partial \Phi^{i}_{n+1}}{\partial t}\right) + Kd^{i}_{n+1} + H\left(d^{i}_{n+1}\right) \tag{B.14}$$

$$\frac{\partial \Phi^{i}_{n+1}}{\partial t}(z,\rho) = \sum_{c=1}^{n_{eqns}} N_c(z,\rho)\frac{\partial d^{i}_{n+1}}{\partial t} \tag{B.15}$$

Where, the superscript i denotes the iteration number in the NR method. Note, (B.5) has no dependence on tissue potentials being solved for, so it remained unchanged. However, (B.6)-(B.8) were dependent on the potentials, so they were differentiated with respects to the degrees of freedom. Differentiation of (B.6)-(B.8) yielded:

$$\frac{\partial F_{ext}}{\partial d} = -\int_{\Gamma_{ETI}} N_A \cdot \left[r_f^{-2}\left(\Phi^{i}_{n+1}\right) \cdot \frac{\partial r_f}{\partial \Phi}\left(\Phi^{i}_{n+1}\right) \cdot \Phi_{ref} \right] \cdot N_B d\Gamma \tag{B.16}$$

$$\frac{\partial H}{\partial d} = -\int_{\Gamma_{ETI}} N_A \cdot \left[r_f^{-2}\left(\Phi^{i}_{n+1}\right) \cdot \frac{\partial r_f}{\partial \Phi}\left(\Phi^{i}_{n+1}\right) \cdot \Phi^{i}_{n+1} \right] \cdot N_B d\Gamma + \int_{\Gamma_{ETI}} N_A \cdot r_f^{-1}\left(\Phi^{i}_{n+1}\right) \cdot N_B d\Gamma \tag{B.17}$$

$$\frac{\partial M}{\partial d} = \int_{\Gamma_{ETI}} N_A \cdot \left[\frac{\partial c_{dl}}{\partial \Phi}\left(\Phi^{i}_{n+1}\right) \cdot \frac{\partial \Phi^{i}_{n+1}}{\partial t} \right] \cdot N_B d\Gamma + \int_{\Gamma_{ETI}} N_A \cdot \left[c_{dl}\left(\Phi^{i}_{n+1}\right) \cdot \frac{1}{\alpha \Delta t} \right] \cdot N_B d\Gamma \tag{B.18}$$

Appendix C Intradural Spinal Cord Stimulation

C.1 Clinical protocol

Subjects were injected with a local anesthetic in the lower back, and a sedative was administered intravenously. Fluoroscopy was used to guide placement of an eight-contact extradural trial lead, the Spencer Probe Depth Electrode (AD-TECH Inc., Racine, WI) (Figure 5.2a), in the extradural space and pick five consecutive contacts that spanned the vertebral levels of interest, T8-T10. The extradural array was connected to an external stimulator (MTS, St. Jude Medical, Saint Paul, MN), and stimulation was delivered in a bipolar configuration between the two contacts closest to T8, where the rostral cathode and caudal anode were proximal and distal to T8, respectively. Stimulation waveforms were current-regulated, asymmetric pulses with a short 300 μs positive phase followed by a long 700 μs negative phase delivered at 60 Hz.

A staircase paradigm was used to determine sensory and discomfort thresholds. First, a reference for paresthesia was established: the stimulation amplitude (I_A) was increased in 1 mA increments from 0 mA until the subject reported a sensation (i.e., S), and I_A was decreased in decrements of 1 mA until S was no longer perceived. The subject was asked to describe orally the location of S. Second, I_A was increased in 0.1 mA increments until S was reported, defined as I_{S1}. Third, I_A was decreased in 0.1 decrements until S went away, defined as I_{S2}. Fourth, I_A was increased in 0.1 mA increments until S

was reported, defined as I_{S3}. The sensory threshold was defined as the average of I_{S1}, I_{S2}, and I_{S3}. Finally, I_A was increased in increments of 0.1 mA until the subject reported discomfort and/or pain, which was defined as the discomfort threshold. As I_A was increased, the subject was asked to describe orally any additional locations of S.

After sensory and discomfort thresholds were measured in the extradural case, fluoroscopy was used to place the AD-TECH array within the dura in a fashion similar to insertion of a standard lumber drain catheter, and the array was connected to the external stimulator. As in the extradural case, current-regulation stimulation was delivered at 60 Hz between the two contacts most proximal to T8, and the staircase paradigm was used to determine sensory and discomfort thresholds.

C.2 Clinical Findings

Paresthesias at the sensory thresholds of Patients 1-5 were reported in the legs, middle and lower back, buttocks, belly, and waistline region (Figure C.1). In Patients 1, 4, and 5, the location of paresthesia differed between the intradural and extradural cases; whereas in Patients 2 and 3, the locations of the paresthesia in the two cases overlapped. In all patients, as the stimulation amplitude increased, paresthesias were reported in additional locations. The quality of the paresthesias and the location of discomfort were not determined.

The sensory thresholds across all patients ranged from 0.2-0.8 mA and 1.3-19 mA in the intradural and extradural cases, respectively, whereas the discomfort thresholds ranged from 0.5-3.1 mA and 2.2-25 mA (Figure C.1). Distributions of the sensory and

discomfort thresholds across patients were not significantly different within the intradural and extradural cases. However, between the intradural and extradural cases, the distributions of sensory ($p < 0.01$) and discomfort ($p < 0.05$) thresholds across patients were significantly different.

The extradural sensory thresholds showed a strong linear correlation ($r^2 > 0.80$, $p < 0.07$) with the ventrodorsal width of the CSF space and the ventral displacement of the spinal cord from the center of the CSF space. The intradural sensory ($r^2 < 0.42$, $p > 0.18$) and discomfort ($r^2 < 0.43$, $p > 0.19$) thresholds and the extradural discomfort thresholds ($r^2 < 0.56$, $p > 0.14$) showed much weaker correlations with differences in the patient geometries.

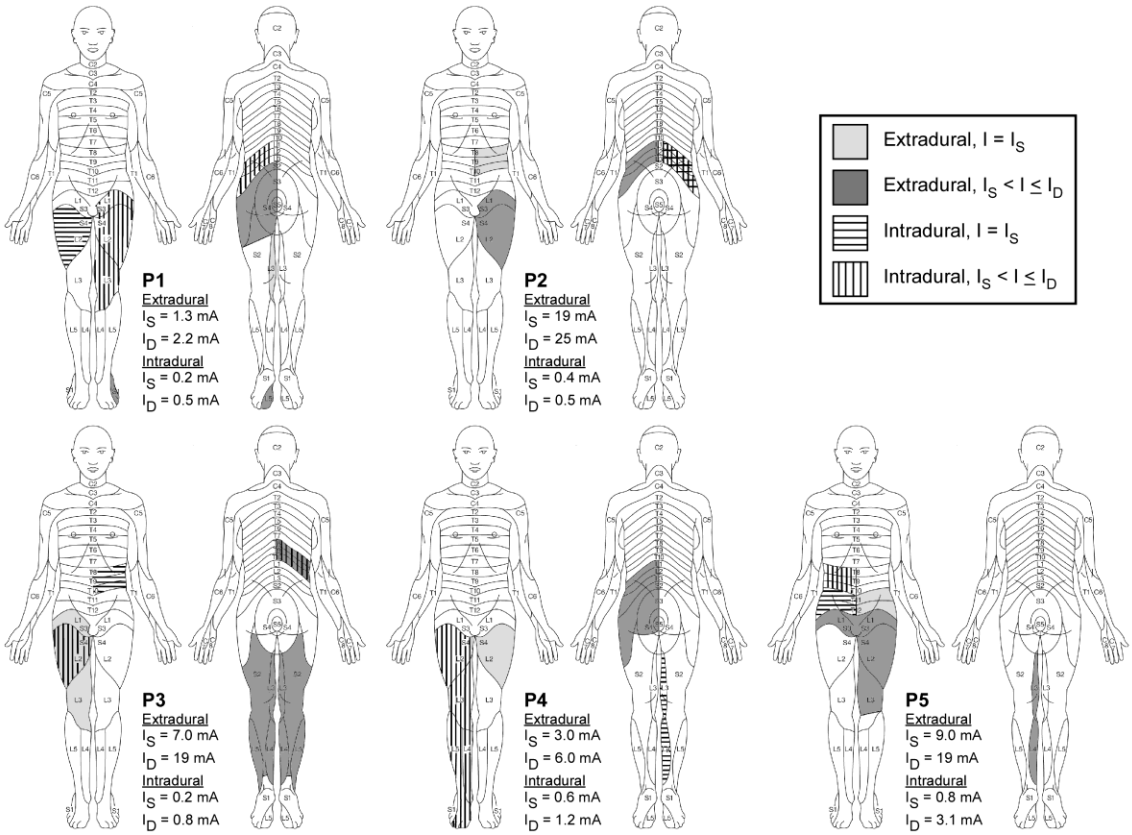

Figure C.1: Reported locations of paresthesias in Patients 1-5.
Paresthesias in each patient (P) were charted based on their oral descriptions at the sensory threshold (I_S) and increasing amplitudes until the discomfort threshold (I_D) was reached. Dermatome maps were adapted from a free resource on http://www.change-pain.co.uk/.

C.3 Clinical Implications

Models incorporating patient-specific dimensions predicted the relative order of stimulation thresholds, the greater than five-fold difference between extradural and intradural stimulation thresholds, and the sensitivity of stimulation thresholds to spinal cord position (Figure 5.4). However, across these five models, there was no clear

distinction of either the diameter or proportion of Aβ fiber activation that correlated best with the sensory and discomfort thresholds of the patients (Figure C.2).

Myelinated fibers in the gracilis fasciculus and cuneatus fasciculus at T3 have diameters ranging from 1-15 μm, with ~ 60 % between 1 and 3 μm [240]; and myelinated fibers in the gracilis fasciculus at T5 have diameters ranging from 1-7 μm, with the majority between 2 and 3 μm [178]. Prior models of extradural SCS showed that DC fibers with diameters > 9.4 μm were activated between measured sensory and discomfort thresholds [41], and activation of large DC fibers with a diameter of 12 μm, which constitute < 0.5 % of all DC fibers [175], best matched measured sensory thresholds [41, 42]. The results of our study corroborated these prior findings in some patients (e.g., Patient 1), depending on the choice of axon model, but in the other patients (e.g., Patient 5), the results suggest that DC fibers with diameters as small as 3 μm are also activated at the sensory threshold (Figures C.2 and 5.4).

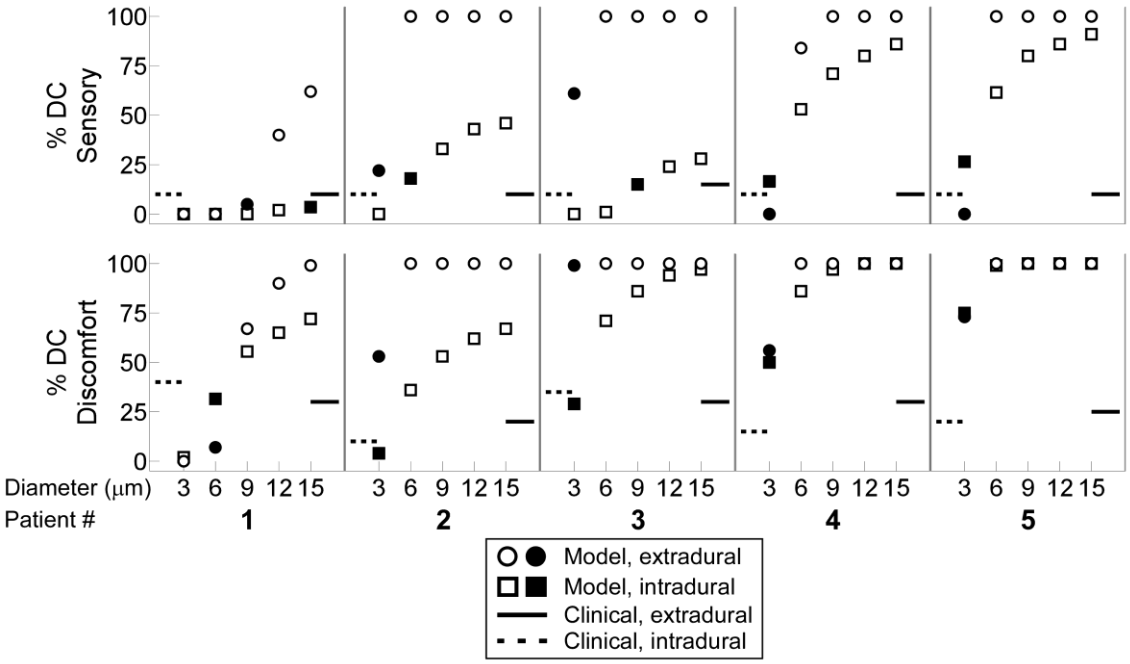

Figure C.2: Predicting the diameter of dorsal column (DC) fibers activated based on clinical thresholds.
The percentage of MRG model DC fibers (denoted by circles and squares) activated at the sensory (top) and discomfort (bottom) thresholds compared to the percent activation expected (denoted by solid and dashed lines) based on the number of dermatomes reported at the corresponding clinical thresholds (see Methods). The filled shapes indicate the fiber diameters that yielded the smallest percent difference between the former and latter cases.

The discrepancy between our results and previous findings may be explained by the choice of axon model. Prior models of extradural SCS used a simplified SW model of a mammalian nerve fiber with perfectly insulating myelin [41, 42, 46, 47, 130, 153, 154, 167, 172-174], whereas we used a more detailed MRG axon model that better replicates the excitability of mammalian nerve fibers [102]. The SW model overestimated stimulation thresholds compared to the MRG model (Figure 5.4), possibly explaining why prior modeling studies concluded that DC fibers with diameters > 9 μm are the therapeutic targets of SCS.

The present results provide an alternate interpretation of which DC fibers are the potential therapeutic targets of SCS. Although it is possible that activation of one (or a few) 12 μm DC fibers is sufficient to evoke paresthesia [41], the results suggest that paresthesia induction requires activation of a larger proportion of DC fibers with diameters as small as 3 μm. Resolving these two possible interpretations will require more closely matching patient-specific models with the experimental conditions. For example, the presence of interstitial fluid and blood around the electrode and the distance and orientation of the stimulating array with respect to spinal cord will influence thresholds, and thereby influence the assessment of which Aβ fiber diameters are activated at sensory and discomfort thresholds. In addition, patient-to-patient variability in sensorimotor and pain networks (i.e., variability in the reporter) could influence threshold sensations.

Additionally, the clinical results provide an alternate interpretation of which neural elements are responsible for discomfort. Due to the relatively low stimulation thresholds of fibers entering the DR [42], discomfort is often associated with segmental motor reflexes [241] and/or uncomfortable sensations [242] that arise from stimulation of Ia and Aβ fibers in the DR, respectively. In our study, only Patients 3 and 5 reported discomfort in T8 (Figure C.1). Although the results cannot address where discomfort occurred or what were the qualities of discomfort, they provide evidence that discomfort can be associated with activation of Aβ fibers in both target and non-target dermatomes (Figure C.1). Further, a percent increase in activation of model DC fibers was not able to explain the onset of discomfort, so other mechanisms may be required to explain

discomfort. For example, discomfort may arise from stimulation of other neural elements in the DC, such as ascending nociceptive fibers or descending fibers from the brain [243], or supra-threshold depolarization of Aβ fibers, which can result in a volley of action potentials per stimulation pulse, rather than a single action potential [244].

References

[1] P. Limousin, J. D. Speelman, F. Gielen, and M. Janssens, "Multicentre European study of thalamic stimulation in parkinsonian and essential tremor," *J Neurol Neurosurg Psychiatry,* vol. 66, pp. 289-96, Mar 1999.

[2] E. B. Montgomery, Jr., "Deep brain stimulation reduces symptoms of Parkinson disease," *Cleve Clin J Med,* vol. 66, pp. 9-11, Jan 1999.

[3] M. Hodaie, Richard A. Wennberg, Jonathan O. Dostrovsky, and Andres M. Lozano, "Chronic Anterior Thalamus Stimulation for Intractable Epilepsy," *Epilepsia,* vol. 43, pp. 603-608, 2002.

[4] M. Velasco, F. Velasco, and A. L. Velasco, "Centromedian-Thalamic and Hippocampal Electrical Stimulation for the Control of Intractable Epileptic Seizures," *Journal of Clinical Neurophysiology,* vol. 18, pp. 495-513, 2001.

[5] J. Kuhn, T. O. Grundler, D. Lenartz, V. Sturm, J. Klosterkotter, and W. Huff, "Deep brain stimulation for psychiatric disorders," *Dtsch Arztebl Int,* vol. 107, pp. 105-13, Feb 2010.

[6] H. S. Mayberg, A. M. Lozano, V. Voon, H. E. McNeely, D. Seminowicz, C. Hamani, *et al.*, "Deep Brain Stimulation for Treatment-Resistant Depression," *Neuron,* vol. 45, pp. 651-660, 2005.

[7] R. J. Coffey, "Deep Brain Stimulation for Chronic Pain: Results of Two Multicenter Trials and a Structured Review," *Pain Medicine,* vol. 2, pp. 183-192, 2001.

[8] T. Cameron, "Safety and efficacy of spinal cord stimulation for the treatment of chronic pain: a 20-year literature review," *Journal of Neurosurgery: Spine,* vol. 100, pp. 254-267, 2004.

[9] R. V. Shannon, "Advances in auditory prostheses," *Current Opinion in Neurology,* vol. 25, pp. 61-66 10.1097/WCO.0b013e32834ef878, 2012.

[10] J. F. Rizzo and J. Wyatt, "REVIEW ■ : Prospects for a Visual Prosthesis," *The Neuroscientist,* vol. 3, pp. 251-262, July 1, 1997 1997.

[11] S. C. Schachter and C. B. Saper, "Vagus Nerve Stimulation," *Epilepsia,* vol. 39, pp. 677-686, 1998.

[12] H. A. Sackeim, A. J. Rush, M. S. George, L. B. Marangell, M. M. Husain, Z. Nahas*, et al.*, "Vagus Nerve Stimulation (VNS[trade]) for Treatment-Resistant Depression: Efficacy, Side Effects, and Predictors of Outcome," *Neuropsychopharmacology,* vol. 25, pp. 713-728, 11//print 2001.

[13] R. L. Weiner and K. L. Reed, "Peripheral Neurostimulation for Control of Intractable Occipital Neuralgia," *Neuromudulation: Technology at the Neural Interface,* vol. 2, pp. 217-221, 1999.

[14] S. Jezernik, M. Craggs, W. M. Grill, G. Creasey, and N. J. M. Rijkhoff, "Electrical stimulation for the treatment of bladder dysfunction: Current status and future possibilities," *Neurological Research,* vol. 24, pp. 413-430, // 2002.

[15] P. H. Peckham and J. S. Knutson, "FUNCTIONAL ELECTRICAL STIMULATION FOR NEUROMUSCULAR APPLICATIONS*," *Annual Review of Biomedical Engineering,* vol. 7, pp. 327-360, 2005.

[16] M. A. Lebedev and M. A. L. Nicolelis, "Brain–machine interfaces: past, present and future," *Trends in Neurosciences,* vol. 29, pp. 536-546, 9// 2006.

[17] C. E. Elger and K. Lehnertz, "Seizure prediction by non-linear time series analysis of brain electrical activity," *European Journal of Neuroscience,* vol. 10, pp. 786-789, 1998.

[18] G. Kleiner-Fisman, J. Herzog, D. N. Fisman, F. Tamma, K. E. Lyons, R. Pahwa*, et al.*, "Subthalamic nucleus deep brain stimulation: Summary and meta-analysis of outcomes," *Movement Disorders,* vol. 21, pp. S290-S304, 2006.

[19] R. S. Taylor, M. J. Desai, P. Rigoard, and R. J. Taylor, "Predictors of pain relief following spinal cord stimulation in chronic back and leg pain and failed back surgery syndrome: a systematic review and meta-regression analysis," *Pain Practice,* vol. . doi: 10.1111/papr.12095, Jul 8 2013.

[20] M. S. Okun, R. L. Rodriguez, K. D. Foote, A. Sudhyadhom, F. Bova, C. Jacobson*, et al.*, "A case-based review of troubleshooting deep brain stimulator issues in movement and neuropsychiatric disorders," *Parkinsonism Relat Disord,* vol. 14, pp. 532-8, Nov 2008.

[21] G. K. Bell, D. Kidd, and R. B. North, "Cost-effectiveness analysis of spinal cord stimulation in treatment of failed back surgery syndrome," *Journal of Pain and Symptom Management,* vol. 13, pp. 286-295, 5// 1997.

[22] E. J. Boviatsis, L. C. Stavrinou, M. Themistocleous, A. T. Kouyialis, and D. E. Sakas, "Surgical and hardware complications of deep brain stimulation. A seven-year experience and review of the literature," *Acta Neurochir (Wien),* vol. 152, pp. 2053-62, Dec 2010.

[23] J. M. Bronstein, M. Tagliati, R. L. Alterman, A. M. Lozano, J. Volkmann, A. Stefani, *et al.*, "Deep Brain Stimulation for Parkinson Disease: An Expert Consensus and Review of Key Issues," *Arch Neurol,* vol. 68, pp. 165-, February 1, 2011 2011.

[24] M. S. Okun, M. Tagliati, M. Pourfar, H. H. Fernandez, R. L. Rodriguez, R. L. Alterman, *et al.*, "Management of referred deep brain stimulation failures: a retrospective analysis from 2 movement disorders centers," *Arch Neurol,* vol. 62, pp. 1250-5, Aug 2005.

[25] T. M. Ellis, K. D. Foote, H. H. Fernandez, A. Sudhyadhom, R. L. Rodriguez, P. Zeilman, *et al.*, "Reoperation for suboptimal outcomes after deep brain stimulation surgery," *Neurosurgery,* vol. 63, pp. 754-60; discussion 760-1, Oct 2008.

[26] A. M. Kuncel and W. M. Grill, "Selection of stimulus parameters for deep brain stimulation," *Clinical Neurophysiology,* vol. 115, pp. 2431-2441, 2004.

[27] V. S. Polikov, P. A. Tresco, and W. M. Reichert, "Response of brain tissue to chronically implanted neural electrodes," *Journal of Neuroscience Methods,* vol. 148, pp. 1-18, 2005.

[28] D. Budai, *Carbon Fiber-based Microelectrodes and Microbiosensors*, 2010.

[29] R. Cicione, M. N. Shivdasani, J. B. Fallon, C. D. Luu, P. J. Allen, G. D. Rathbone, *et al.*, "Visual cortex responses to suprachoroidal electrical stimulation of the retina: effects of electrode return configuration," *Journal of Neural Engineering,* vol. 9, p. 036009, 2012.

[30] A. Branner and R. A. Normann, "A multielectrode array for intrafascicular recording and stimulation in sciatic nerve of cats," *Brain Research Bulletin,* vol. 51, pp. 293-306, 3/1/ 2000.

[31] E. L. Foldes, D. M. Ackermann, N. Bhadra, K. L. Kilgore, and N. Bhadra, "Design, fabrication and evaluation of a conforming circumpolar peripheral nerve cuff electrode for acute experimental use," *Journal of Neuroscience Methods,* vol. 196, pp. 31-37, 3/15/ 2011.

[32] B. Howell and W. M. Grill, "Design of electrodes for stimulation and recording," in *Implantable Neuroprostheses for Restoring Function*, K. Kilgore, Ed., 1 ed Cambridge: Woodhead Publishing, 2015, pp. 59-93.

[33] A. Norlin, J. Pan, and C. Leygraf, "Investigation of interfacial capacitance of Pt, Ti and TiN coated electrodes by electrochemical impedance spectroscopy," *Biomolecular Engineering,* vol. 19, pp. 67-71, 8// 2002.

[34] T. L. Rose, E. M. Kelliher, and L. S. Robblee, "Assessment of capacitor electrodes for intracortical neural stimulation," *Journal of Neuroscience Methods,* vol. 12, pp. 181-193, 1// 1985.

[35] S. F. Cogan, "Neural stimulation and recording electrodes," *Annu Rev Biomed Eng,* vol. 10, pp. 275-309, 2008.

[36] R. Pendekanti and C. S. Henriquez, "Spatial potential and current distributions along transvenous defibrillation electrodes: variation of electrode characteristics," *Ann Biomed Eng,* vol. 24, pp. 156-67, Jan-Feb 1996.

[37] X. F. Wei and W. M. Grill, "Current density distributions, field distributions and impedance analysis of segmented deep brain stimulation electrodes," *J Neural Eng,* vol. 2, pp. 139-47, Dec 2005.

[38] B. Howell and W. M. Grill, "Evaluation of high-perimeter electrode designs for deep brain stimulation," *Journal of Neural Engineering,* vol. 11, p. 046026, 2014.

[39] F. Rattay, "Analysis of models for external stimulation of axons," *IEEE Transactions on Biomedical Engineering,* vol. 33, pp. 974-977, 1986.

[40] C. Gabriel, A. Peyman, and E. H. Grant, "Electrical conductivity of tissue at frequencies below 1 MHz," *Phys Med Biol,* vol. 54, pp. 4863-78, Aug 21 2009.

[41] J. Holsheimer, "Which neuronal elements are activated directly by spinal cord stimulation," *Neuromodulation,* vol. 5, pp. 25-31, Jan 2002.

[42] J. J. Struijk, J. Holsheimer, and H. B. Boom, "Excitation of dorsal root fibers in spinal cord stimulation: a theoretical study," *IEEE Transactions on Biomedical Engineering,* vol. 40, pp. 632-9, Jul 1993.

[43] F. Rattay and S. Resatz, "Effective electrode configuration for selective stimulation with inner eye prostheses," *Biomedical Engineering, IEEE Transactions on,* vol. 51, pp. 1659-1664, 2004.

[44] M. A. Schiefer and W. M. Grill, "Sites of neuronal excitation by epiretinal electrical stimulation," *Neural Systems and Rehabilitation Engineering, IEEE Transactions on,* vol. 14, pp. 5-13, 2006.

[45] J. Holsheimer, "Computer modelling of spinal cord stimulation and its contribution to therapeutic efficacy," *Spinal Cord,* vol. 36, pp. 531-40, Aug 1998.

[46] J. Holsheimer, J. J. Struijk, and W. A. Wesselink, "Analysis of spinal cord stimulation and design of epidural electrodes by computer modeling," *Neuromodulation: Technology at the Neural Interface,* vol. 1, pp. 14-18, 1998.

[47] L. Manola and J. Holsheimer, "Technical performance of percutaneous and laminectomy leads analyzed by modeling," *Neuromodulation: Technology at the Neural Interface,* vol. 7, pp. 231-241, 2004.

[48] R. A. Kent and M. W. Grill, "Model-based analysis and design of nerve cuff electrodes for restoring bladder function by selective stimulation of the pudendal nerve," *Journal of Neural Engineering,* vol. 10, p. 036010, 2013.

[49] J. D. Sweeney, D. A. Ksienski, and J. T. Mortimer, "A nerve cuff technique for selective excitation of peripheral nerve trunk regions," *IEEE Trans Biomed Eng,* vol. 37, pp. 706-15, Jul 1990.

[50] M. Keane, S. Deyo, A. Abosch, J. A. Bajwa, and M. D. Johnson, "Improved spatial targeting with directionally segmented deep brain stimulation leads for treating essential tremor," *J Neural Eng,* vol. 9, p. 046005, Aug 2012.

[51] Z. P. Fang and J. T. Mortimer, "A method to effect physiological recruitment order in electrically activated muscle," *Biomedical Engineering, IEEE Transactions on,* vol. 38, pp. 175-179, 1991.

[52] Z. P. Fang and J. T. Mortimer, "Selective activation of small motor axons by quasitrapezoidal current pulses," *Biomedical Engineering, IEEE Transactions on,* vol. 38, pp. 168-174, 1991.

[53] Z. Lertmanorat and M. D. Durand, "Extracellular voltage profile for reversing the recruitment order of peripheral nerve stimulation: a simulation study," *Journal of Neural Engineering,* vol. 1, p. 202, 2004.

[54] Z. Lertmanorat, K. Gustafson, and D. Durand, "Electrode Array for Reversing the Recruitment Order of Peripheral Nerve Stimulation: Experimental Studies," *Annals of Biomedical Engineering,* vol. 34, pp. 152-160, 2006/01/01 2006.

[55] J. A. Murray and W. F. Blakemore, "The relationship between internodal length and fibre diameter in the spinal cord of the cat," *Journal of the Neurological Sciences,* vol. 45, pp. 29-41, 1980.

[56] M. J. Birdno, A. M. Kuncel, A. D. Dorval, D. A. Turner, R. E. Gross, and W. M. Grill, "Stimulus features underlying reduced tremor suppression with temporally patterned deep brain stimulation," *Journal of Neurophysiology,* vol. 107, pp. 364-383, January 1, 2012 2012.

[57] V. Gradinaru, M. Mogri, K. R. Thompson, J. M. Henderson, and K. Deisseroth, "Optical Deconstruction of Parkinsonian Neural Circuitry," *Science,* vol. 324, pp. 354-359, April 17, 2009 2009.

[58] D. Chaudhury, J. J. Walsh, A. K. Friedman, B. Juarez, S. M. Ku, J. W. Koo, *et al.*, "Rapid regulation of depression-related behaviours by control of midbrain dopamine neurons," *Nature,* vol. advance online publication, 12/12/online 2012.

[59] C. McIntyre and W. Grill, "Selective Microstimulation of Central Nervous System Neurons," *Annals of Biomedical Engineering,* vol. 28, pp. 219-233, 2000/03/01 2000.

[60] Q. Wang, D. C. Millard, H. J. Zheng, and G. B. Stanley, "Voltage-sensitive dye imaging reveals improved topographic activation of cortex in response to manipulation of thalamic microstimulation parameters," *J Neural Eng,* vol. 9, p. 026008, Apr 2012.

[61] K. M. Alo, M. J. Yland, D. L. Kramer, J. H. Charnov, and V. Redko, "Computer Assisted and Patient Interactive Programming of Dual Octrode Spinal Cord Stimulation in the Treatment of Chronic Pain," *Neuromodulation,* vol. 1, p. 30, Winter98 1998.

[62] K. Gosalia, J. Weiland, M. Humayun, and G. Lazzi, "Thermal elevation in the human eye and head due to the operation of a retinal prosthesis," *Biomedical Engineering, IEEE Transactions on,* vol. 51, pp. 1469-1477, 2004.

[63] M. M. Elwassif, A. Datta, A. Rahman, and M. Bikson, "Temperature control at DBS electrodes using a heat sink: experimentally validated FEM model of DBS lead architecture," *Journal of Neural Engineering,* vol. 9, p. 046009, 2012.

[64] M. M. Elwassif, Q. Kong, M. Vazquez, and M. Bikson, "Bio-heat transfer model of deep brain stimulation-induced temperature changes," *Journal of Neural Engineering,* vol. 3, p. 306, 2006.

[65] L. S. Goldstein, M. W. Dewhirst, M. Repacholi, and L. Kheifets, "Summary, conclusions and recommendations: adverse temperature levels in the human body," *International Journal of Hyperthermia,* vol. 19, pp. 373-384, // 2003.

[66] H. H. Pennes, "Analysis of Tissue and Arterial Blood Temperatures in the Resting Human Forearm," *Journal of Applied Physiology,* vol. 1, pp. 93-122, August 1, 1948 1948.

[67] D. R. Merrill, M. Bikson, and J. G. Jefferys, "Electrical stimulation of excitable tissue: design of efficacious and safe protocols," *J Neurosci Methods,* vol. 141, pp. 171-98, Feb 15 2005.

[68] D. B. McCreery, W. F. Agnew, T. G. H. Yuen, and L. Bullara, "Charge density and charge per phase as cofactors in neural injury induced by electrical stimulation," *Biomedical Engineering, IEEE Transactions on,* vol. 37, pp. 996-1001, 1990.

[69] R. V. Shannon, "A model of safe levels for electrical stimulation," *Biomedical Engineering, IEEE Transactions on,* vol. 39, pp. 424-426, 1992.

[70] C. C. McIntyre, W. M. Grill, D. L. Sherman, and N. V. Thakor, "Cellular effects of deep brain stimulation: model-based analysis of activation and inhibition," *J Neurophysiol,* vol. 91, pp. 1457-69, Apr 2004.

[71] C. Beurrier, B. Bioulac, J. Audin, and C. Hammond, "High-frequency stimulation produces a transient blockade of voltage-gated currents in subthalamic neurons," *Journal of neurophysiology,* vol. 85, pp. 1351-1356, 2001.

[72] C. R. Butson, S. E. Cooper, J. M. Henderson, and C. C. McIntyre, "Patient-specific analysis of the volume of tissue activated during deep brain stimulation," *Neuroimage,* vol. 34, pp. 661-70, Jan 15 2007.

[73] A. Chaturvedi, C. R. Butson, S. F. Lempka, S. E. Cooper, and C. C. McIntyre, "Patient-specific models of deep brain stimulation: influence of field model

complexity on neural activation predictions," *Brain Stimul,* vol. 3, pp. 65-7, Apr 2010.

[74] S. N. Sotiropoulos and P. N. Steinmetz, "Assessing the direct effects of deep brain stimulation using embedded axon models," *Journal of Neural Engineering,* vol. 4, p. 107, 2007.

[75] X. F. Wei and W. M. Grill, "Analysis of high-perimeter planar electrodes for efficient neural stimulation," *Front Neuroeng,* vol. 2, p. 15, 2009.

[76] T. J. R. Hughes, *The Finite Element Method*, 2000.

[77] C. R. Butson, C. B. Maks, and C. C. McIntyre, "Sources and effects of electrode impedance during deep brain stimulation," *Clin Neurophysiol,* vol. 117, pp. 447-54, Feb 2006.

[78] C. R. Butson and C. C. McIntyre, "Tissue and electrode capacitance reduce neural activation volumes during deep brain stimulation," *Clin Neurophysiol,* vol. 116, pp. 2490-500, Oct 2005.

[79] N. Yousif, R. Bayford, P. G. Bain, and X. Liu, "The peri-electrode space is a significant element of the electrode–brain interface in deep brain stimulation: A computational study," *Brain Research Bulletin,* vol. 74, pp. 361-368, 2007.

[80] X. F. Wei and W. M. Grill, "Impedance characteristics of deep brain stimulation electrodes in vitro and in vivo," *J Neural Eng,* vol. 6, pp. 1741-2560, Aug 2009.

[81] B. Howell, S. Naik, and W. M. Grill, "Influences of interpolation error, electrode geometry, and the electrode-tissue interface on models of electric fields produced by deep brain stimulation," *IEEE Transactions on Biomedical Engineering,* vol. 61, pp. 297-307, 2014.

[82] C. A. Bossetti, M. J. Birdno, and W. M. Grill, "Analysis of the quasi-static approximation for calculating potentials generated by neural stimulation," *J Neural Eng,* vol. 5, pp. 44-53, Mar 2008.

[83] P. W. Nicholson, "Specific impedance of cerebral white matter," *Exp Neurol,* vol. 13, pp. 386-401, Dec 1965.

[84] N. T. Carnevale and M. L. Hines, *The NEURON Book*. Cambridge: Cambridge University Press, 1997.

[85] J. Sweeney, J. Mortimer, and D. Durand, "Modeling of mammalian myelinated nerve for functional neuromuscular stimulation," in *IEEE 9th Annual Conference of the Engineering in Medicine and Biology Society*, 1987, pp. 1577-1578.

[86] J. Schwarz, G. Reid, and H. Bostock, "Action potentials and membrane currents in the human node of Ranvier," *Pflügers Archiv,* vol. 430, pp. 283-292, 1995/06/01 1995.

[87] S. Dong and G. E. Karniadakis, "P-refinement and P-threads," *Computer methods in applied mechanics and engineering,* vol. 192, pp. 2191-2201, 2003.

[88] C. Haberler, F. Alesch, P. R. Mazal, P. Pilz, K. Jellinger, M. M. Pinter, *et al.*, "No tissue damage by chronic deep brain stimulation in Parkinson's disease," *Ann Neurol,* vol. 48, pp. 372-6, Sep 2000.

[89] J. Moss, T. Ryder, T. Z. Aziz, M. B. Graeber, and P. G. Bain, "Electron microscopy of tissue adherent to explanted electrodes in dystonia and Parkinson's disease," *Brain,* vol. 127, pp. 2755-63, Dec 2004.

[90] C. R. Butson and C. C. McIntyre, "Role of electrode design on the volume of tissue activated during deep brain stimulation," *J Neural Eng,* vol. 3, pp. 1-8, Mar 2006.

[91] M. R. Behrend, A. K. Ahuja, and J. D. Weiland, "Dynamic current density of the disk electrode double-layer," *IEEE Trans Biomed Eng,* vol. 55, pp. 1056-62, Mar 2008.

[92] D. R. Cantrell, S. Inayat, A. Taflove, R. S. Ruoff, and J. B. Troy, "Incorporation of the electrode-electrolyte interface into finite-element models of metal microelectrodes," *J Neural Eng,* vol. 5, pp. 54-67, Mar 2008.

[93] A. J. Bard and L. R. Faulkner, *Electrochemical Methods - Fundamentals and Applications*, 2nd ed.: Wiley, 2000.

[94] A. R. Kent and W. M. Grill, "Neural origin of evoked potentials during deep brain stimulation," *Journal of neurophysiology,* 2013.

[95] I. Babuska, B. A. Szabo, and I. N. Katz, "The p-version of the finite element method," *SIAM journal on numerical analysis,* vol. 18, pp. 515-545, 1981.

[96] P. F. Grant and M. M. Lowery, "Effect of Dispersive Conductivity and Permittivity in Volume Conductor Models of Deep Brain Stimulation," *Biomedical Engineering, IEEE Transactions on,* vol. 57, pp. 2386-2393, 2010.

[97] A. R. Kent and W. M. Grill, "Instrumentation to record evoked potentials for closed-loop control of deep brain stimulation," in *Engineering in Medicine and Biology Society, EMBC, 2011 Annual International Conference of the IEEE*, 2011, pp. 6777-6780.

[98] A. Kuhn, T. Keller, M. Lawrence, and M. Morari, "A model for transcutaneous current stimulation: simulations and experiments," *Medical & Biological Engineering & Computing,* vol. 47, pp. 279-289, 2009/03/01 2009.

[99] T. L. Rose and L. S. Robblee, "Electrical stimulation with Pt electrodes. VIII. Electrochemically safe charge injection limits with 0.2 ms pulses," *IEEE Trans Biomed Eng,* vol. 37, pp. 1118-20, Nov 1990.

[100] M. Astrom, J. D. Johansson, M. I. Hariz, O. Eriksson, and K. Wardell, "The effect of cystic cavities on deep brain stimulation in the basal ganglia: a simulation-based study," *J Neural Eng,* vol. 3, pp. 132-8, Jun 2006.

[101] K. B. Oldham, "The RC time "constant" at a disk electrode," *Electrochemistry Communications,* vol. 6, pp. 210-214, 2004.

[102] C. C. McIntyre, A. G. Richardson, and W. M. Grill, "Modeling the excitability of mammalian nerve fibers: influence of afterpotentials on the recovery cycle," *Journal of Neurophysiology,* vol. 87, pp. 995-1006, 2002.

[103] I. Babuška and M. Suri, "The p and h-p versions of the finite element method, basic principles and properties," *SIAM review,* vol. 36, pp. 578-632, 1994.

[104] S. Chiu, J. Ritchie, R. Rogart, and D. Stagg, "A quantitative description of membrane currents in rabbit myelinated nerve," *The Journal of Physiology,* vol. 292, pp. 149-166, 1979.

[105] M. Åström, J.-J. Lemaire, and K. Wårdell, "Influence of heterogeneous and anisotropic tissue conductivity on electric field distribution in deep brain stimulation," *Medical & biological engineering & computing,* vol. 50, pp. 23-32, 2012.

[106] R. Nieuwenhuyis, H. J. ten Donkelaar, and C. Nicholson, *The Central Nervous System of Vertebrates: With Posters* vol. 1: Springer, 1998.

[107] W. G. Ondo, C. Meilak, and K. D. Vuong, "Predictors of battery life for the Activa Soletra 7426 Neurostimulator," *Parkinsonism Relat Disord,* vol. 13, pp. 240-2, May 2007.

[108] C. H. Halpern, K. R. McGill, G. H. Baltuch, and J. L. Jaggi, "Longevity Analysis of Currently Available Deep Brain Stimulation Devices," *Stereotactic and Functional Neurosurgery,* vol. 89, pp. 1-5, 2011.

[109] C. K. Lam and J. M. Rosenow, "Patient Perspectives on the Efficacy and Ergonomics of Rechargeable Spinal Cord Stimulators," *Neuromodulation: Technology at the Neural Interface,* vol. 13, pp. 218-223, 2010.

[110] C. C. McIntyre and W. M. Grill, "Extracellular Stimulation of Central Neurons: Influence of Stimulus Waveform and Frequency on Neuronal Output," *Journal of Neurophysiology,* vol. 88, pp. 1592-1604, October 1, 2002 2002.

[111] S. F. Cogan, "In vivo and In vitro Differences in the Charge-injection and Electrochemical Properties of Iridium Oxide Electrodes," in *Conf Proc IEEE Eng Med Bio Soc*, 2006, pp. 882-885.

[112] L. M. Fischer, M. Tenje, A. R. Heiskanen, N. Masuda, J. Castillo, A. Bentien*, et al.*, "Gold cleaning methods for electrochemical detection applications," *Microelectronic Engineering,* vol. 86, pp. 1282-1285, 2009.

[113] E. M. Hudak, J. T. Mortimer, and H. B. Martin, "Platinum for neural stimulation: voltammetry considerations," *Journal of Neural Engineering,* vol. 7, p. 026005, 2010.

[114] T. Izumi, I. Watanabe, and Y. Yokoyama, "Activation of a gold electrode by electrochemical oxidation-reduction pretreatment in hydrochloric acid," *Journal of Electroanalytical Chemistry and Interfacial Electrochemistry,* vol. 303, pp. 151-160, 1991.

[115] E. G. Duerden, K. W. Finnis, T. M. Peters, and A. F. Sadikot, "Three-dimensional somatotopic organization and probabilistic mapping of motor responses from the human internal capsule," *J Neurosurg,* vol. 114, pp. 1706-14, Jun 2011.

[116] R. S. Snider and W. T. Niemer, *A stereotaxic Atlas of the Cat Brain*: University of Chicago Press, 1961.

[117] D. A. Gutman, P. E. Holtzheimer, T. E. Behrens, H. Johansen-Berg, and H. S. Mayberg, "A tractography analysis of two deep brain stimulation white matter targets for depression," *Biol Psychiatry,* vol. 65, pp. 276-82, Feb 15 2009.

[118] M. J. Birdno and W. M. Grill, "Mechanisms of deep brain stimulation in movement disorders as revealed by changes in stimulus frequency," *Neurotherapeutics,* vol. 5, pp. 14-25, Jan 2008.

[119] J. L. Lujan, A. Chaturvedi, and C. C. McIntyre, "Tracking the mechanisms of deep brain stimulation for neuropsychiatric disorders," *Frontiers in bioscience: a journal and virtual library,* vol. 13, p. 5892, 2008.

[120] T. J. Foutz and C. C. McIntyre, "Evaluation of novel stimulus waveforms for deep brain stimulation," *Journal of Neural Engineering,* vol. 7, p. 066008, 2010.

[121] M. Sahin and Y. Tie, "Non-rectangular waveforms for neural stimulation with practical electrodes," *Journal of Neural Engineering,* vol. 4, p. 227, 2007.

[122] A. Wongsarnpigoon and W. M. Grill, "Energy-efficient waveform shapes for neural stimulation revealed with a genetic algorithm," *Journal of Neural Engineering,* vol. 7, p. 046009, 2010.

[123] L. Golestanirad, C. Pollo, and S. J. Graham, "Analysis of fractal electrodes for efficient neural stimulation," in *Engineering in Medicine and Biology Society (EMBC), 2013 35th Annual International Conference of the IEEE*, 2013, pp. 791-794.

[124] J. Buhlmann, L. Hofmann, P. A. Tass, and C. Hauptmann, "Modeling of a segmented electrode for desynchronizing deep brain stimulation," *Front Neuroeng,* vol. 4, p. 15, 2011.

[125] H. C. F. Martens, E. Toader, M. M. J. Decré, D. J. Anderson, R. Vetter, D. R. Kipke, *et al.*, "Spatial steering of deep brain stimulation volumes using a novel lead design," *Clinical Neurophysiology,* vol. 122, pp. 558-566, 3// 2011.

[126] B. Howell and W. M. Grill, "Model-based optimization of electrode designs for deep brain stimulation," in *Neural Engineering (NER), 2013 6th International IEEE/EMBS Conference on*, 2013, pp. 154-157.

[127] W. M. Grill and J. T. Mortimer, "Electrical properties of implant encapsulation tissue," *Ann Biomed Eng,* vol. 22, pp. 23-33, Jan-Feb 1994.

[128] J. Holsheimer and W. A. Wesselink, "Optimum electrode geometry for spinal cord stimulation: The narrow bipole and tripole," *Medical and Biological Engineering and Computing,* vol. 35, pp. 493-497, 1997/09/01 1997.

[129] R. B. North, D. H. Kidd, J. C. Olin, and J. M. Sieracki, "Spinal cord stimulation electrode design: Prospective, randomized, controlled trial comparing percutaneous and laminectomy electrodes—part I: technical outcomes," *Neurosurgery,* vol. 51, pp. 381-390, 2002.

[130] V. Sankarasubramanian, J. R. Buitenweg, J. Holsheimer, and P. Veltink, "Electrode alignment of transverse tripoles using a percutaneous triple-lead approach in spinal cord stimulation," *Journal of Neural Engineering,* vol. 8, pp. 1741-2560, Jan 19 2011.

[131] J. T. Rubinstein, "Axon termination conditions for electrical stimulation," *IEEE Trans Biomed Eng,* vol. 40, pp. 654-63, Jul 1993.

[132] F. Rattay, "The basic mechanism for the electrical stimulation of the nervous system," *Neuroscience,* vol. 89, pp. 335-46, Mar 1999.

[133] H. Lu, C. A. Chestek, K. M. Shaw, and H. J. Chiel, "Selective extracellular stimulation of individual neurons in ganglia," *Journal of Neural Engineering,* vol. 5, p. 287, 2008.

[134] R. N. Lemon, "Descending Pathways in Motor Control," *Annual Review of Neuroscience,* vol. 31, pp. 195-218, 2008.

[135] K. V. Slavin, K. R. Thulborn, C. Wess, and H. Nersesyan, "Direct Visualization of the Human Subthalamic Nucleus with 3T MR Imaging," *AJNR Am J Neuroradiol,* vol. 27, pp. 80-84, January 1, 2006 2006.

[136] W. M. Grill, Jr. and J. T. Mortimer, "Quantification of recruitment properties of multiple contact cuff electrodes," *Rehabilitation Engineering, IEEE Transactions on,* vol. 4, pp. 49-62, 1996.

[137] A. M. M. Frankemolle, J. Wu, A. M. Noecker, C. Voelcker-Rehage, J. C. Ho, J. L. Vitek*, et al.*, "Reversing cognitive–motor impairments in Parkinson's disease patients using a computational modelling approach to deep brain stimulation programming," *Brain,* vol. 133, pp. 746-761, March 1, 2010 2010.

[138] B. F. Walker, "The prevalence of low back pain: A systematic review of the literature from 1966 to 1998," *Journal of Spinal Disorders & Techniques,* vol. 13, pp. 205-217, 2000.

[139] A. Simpson, J. Cholewicki, and J. Grauer, "Chronic low back pain," *Current Pain and Headache Reports,* vol. 10, pp. 431-436, 2006/11/01 2006.

[140] S. Dagenais, J. Caro, and S. Haldeman, "A systematic review of low back pain cost of illness studies in the United States and internationally," *The Spine Journal,* vol. 8, pp. 8-20, 2008.

[141] K. Kumar, C. Toth, R. Nath, and P. Laing, "Epidural spinal cord stimulation for treatment of chronic pain—some predictors of success. A 15-year experience," *Surgical Neurology,* vol. 50, pp. 110-121, 1998.

[142] R. Melzack and P. D. Wall, "Pain mechanisms: a new theory," *Science,* vol. 150, pp. 971-979, Nov 9 1965.

[143] T. C. Zhang, J. J. Janik, and W. M. Grill, "Modeling the effects of spinal cord stimulation on wide dynamic range dorsal horn neurons: influence of stimulation frequency and GABAergic inhibition," *Journal of Neurophysiology,* p. in press, 2014.

[144] S. A. Prescott and S. Ratté, "Pain processing by spinal microcircuits: afferent combinatorics," *Current Opinion in Neurobiology,* vol. 22, pp. 631-639, 2012.

[145] A. J. Todd, "Neuronal circuitry for pain processing in the dorsal horn," *Nature Reviews Neuroscience,* vol. 11, pp. 823-836, 2010.

[146] J. Zheng, Y. Lu, and E. R. Perl, "Inhibitory neurones of the spinal substantia gelatinosa mediate interaction of signals from primary afferents," *The Journal of Physiology,* vol. 588, pp. 2065-2075, June 15, 2010 2010.

[147] T. C. Zhang, J. J. Janik, and W. M. Grill, "Mechanisms and models of spinal cord stimulation for the treatment of neuropathic pain," *Brain Research,* vol. 1569, pp. 19-31, June 20 2014.

[148] G. Barolat, G. Barolat, S. Zeme, S. Zeme, B. Ketcik, and B. Ketcik, "Multifactorial analysis of epidural spinal cord stimulation," *Stereotactic and Functional Neurosurgery,* vol. 56, pp. 77-103, 1991.

[149] R. B. North, D. H. Kidd, M. Zahurak, C. S. James, and D. M. Long, "Spinal cord stimulation for chronic, intractable pain: Experience over two decades," *Neurosurgery,* vol. 32, pp. 384-395, 1993.

[150] K. M. Aló and J. Holsheimer, "New Trends in Neuromodulation for the Management of Neuropathic Pain," *Neurosurgery,* vol. 50, pp. 690-704, 2002.

[151] J. M. Rosenow, M. Stanton-Hicks, A. R. Rezai, and J. M. Henderson, "Failure modes of spinal cord stimulation hardware," *Journal of Neurosurgery: Spine,* vol. 5, pp. 183-190, 2006.

[152] J. C. Oakley, F. Espinosa, H. Bothe, J. McKean, P. Allen, K. Burchiel, *et al.*, "Transverse tripolar spinal cord stimulation: results of an international multicenter study," *Neuromodulation: Technology at the Neural Interface,* vol. 9, pp. 192-203, 2006.

[153] J. J. Struijk, J. Holsheimer, G. H. J. Spincemaille, F. L. H. Gielen, and R. Hoekema, "Theoretical performance and clinical evaluation of transverse tripolar spinal cord stimulation," *IEEE Transactions on Rehabilitation Engineering,* vol. 6, pp. 277-285, 1998.

[154] V. Sankarasubramanian, J. R. Buitenweg, J. Holsheimer, and P. H. Veltink, "Staggered transverse tripoles with quadripolar lateral anodes using percutaneous and surgical leads in spinal cord stimulation," *Neurosurgery,* vol. 72, pp. 483-91, Mar 2013.

[155] M. A. Howard, M. Utz, T. J. Brennan, B. D. Dalm, S. Viljoen, N. D. Jeffery, *et al.*, "Intradural approach to selective stimulation in the spinal cord for treatment of intractable pain: design principles and wireless protocol," *Journal of Applied Physics,* vol. 110, pp. 1-12, 2011.

[156] Q. Huang, H. Oya, O. Flouty, C. Reddy, M. Howard, III, G. Gillies, *et al.*, "Comparison of spinal cord stimulation profiles from intra- and extradural electrode arrangements by finite element modelling," *Medical & Biological Engineering & Computing,* vol. 52, pp. 531-538, 2014/06/01 2014.

[157] D. M. Long, "The current status of electrical stimulation of the nervous system for the relief of chronic pain," *Surgical Neurology,* vol. 49, pp. 142-144, 1998.

[158] R. Babu, M. A. Hazzard, K. T. Huang, B. Ugiliweneza, C. G. Patil, M. Boakye, *et al.*, "Outcomes of percutaneous and paddle lead implantation for spinal cord stimulation: a comparative analysis of complications, reoperation rates, and health-care costs," *Neuromodulation: Technology at the Neural Interface,* vol. 16, pp. 418-427, 2013.

[159] J. Latikka, T. Kuurne, and H. Eskola, "Conductivity of living intracranial tissues," *Physics in Medicine and Biology,* vol. 46, p. 1611, 2001.

[160] B. Howell, S. P. Lad, and W. M. Grill, "Evaluation of Intradural Stimulation Efficiency and Selectivity in a Computational Model of Spinal Cord Stimulation," *PloS one,* vol. 9, p. e114938, 2014.

[161] H. C. Elliott, "Cross-sectional diameters and areas of the human spinal cord," *The Anatomical Record,* vol. 93, pp. 287-293, 1945.

[162] I. Gilad and M. Nissan, "Sagittal evaluation of elemental geometrical dimensions of human vertebrae," *Journal of Anatomy,* vol. 143, p. 115, 1985.

[163] H. Y. Ko, J. H. Park, Y. B. Shin, and S. Y. Baek, "Gross quantitative measurements of spinal cord segments in human," *Spinal Cord,* vol. 42, pp. 35-40, Jan 2004.

[164] C. E. Tschirhart, J. A. Finkelstein, and C. M. Whyne, "Biomechanics of vertebral level, geometry, and transcortical tumors in the metastatic spine," *Journal of Biomechanics,* vol. 40, pp. 46-54, // 2007.

[165] J. B. Ranck Jr and S. L. BeMent, "The specific impedance of the dorsal columns of cat: An anisotropic medium," *Experimental Neurology,* vol. 11, pp. 451-463, 4// 1965.

[166] S. B. Baumann, D. R. Wozny, S. K. Kelly, and F. M. Meno, "The electrical conductivity of human cerebrospinal fluid at body temperature," *IEEE Transactions on Biomedical Engineering,* vol. 44, pp. 220-223, 1997.

[167] J. J. Struijk, J. Holsheimer, G. Barolat, H. Jiping, and H. B. K. Boom, "Paresthesia thresholds in spinal cord stimulation: a comparison of theoretical results with clinical data," *IEEE Transactions on Rehabilitation Engineering,* vol. 1, pp. 101-108, 1993.

[168] D. Miklavčič, N. Pavšelj, and F. X. Hart, "Electric properties of tissues," *Wiley encyclopedia of biomedical engineering,* vol. . doi: 10.1002/9780471740360.ebs0403, 2006.

[169] J. D. Kosterich, K. R. Foster, and S. R. Pollack, "Dielectric permittivity and electrical conductivity of fluid saturated bone," *IEEE Transactions on Biomedical Engineering,* vol. 30, pp. 81-86, 1983.

[170] A. Jackson, H. Yao, M. D. Brown, and W. Yong Gu, "Anisotropic ion diffusivity in intervertebral disc: an electrical conductivity approach," *Spine,* vol. 31, pp. 2783-2789, 2006.

[171] F. L. H. Gielen, W. Wallinga-de Jonge, and K. L. Boon, "Electrical conductivity of skeletal muscle tissue: Experimental results from different musclesin vivo," *Medical and Biological Engineering and Computing,* vol. 22, pp. 569-577, 1984/11/01 1984.

[172] J. Holsheimer, G. Barolat, J. J. Struijk, and J. He, "Significance of the spinal cord position in spinal cord stimulation," in *Advances in Stereotactic and Functional Neurosurgery 11*. vol. 64, B. Meyerson and C. Ostertag, Eds., ed: Springer Vienna, 1995, pp. 119-124.

[173] J. Holsheimer, J. J. Struijk, and N. R. Tas, "Effects of electrode geometry and combination on nerve fibre selectivity in spinal cord stimulation," *Medical and Biological Engineering and Computing,* vol. 33, pp. 676-682, 1995/09/01 1995.

[174] J. J. Struijk, J. Holsheimer, G. G. van der Heide, and H. B. K. Boom, "Recruitment of dorsal column fibers in spinal cord stimulation: influence of collateral branching," *IEEE Transactions on Biomedical Engineering,* vol. 39, pp. 903-912, 1992.

[175] H. K. P. Feirabend, H. Choufoer, S. Ploeger, J. Holsheimer, and J. D. van Gool, "Morphometry of human superficial dorsal and dorsolateral column fibres: significance to spinal cord stimulation," *Brain,* vol. 125, pp. 1137-1149, May 1, 2002 2002.

[176] M. C. Smith and P. Deacon, "Topographical anatomy of the posterior columns of the spinal cord in man: the long ascending fibers," *Brain,* vol. 107, pp. 671-698, September 1, 1984 1984.

[177] W. A. Wesselink, J. Holsheimer, B. Nuttin, H. B. K. Boom, G. W. King, J. M. Gybels, *et al.*, "Estimation of fiber diameters in the spinal dorsal columns from clinical data," *IEEE Transactions on Biomedical Engineering,* vol. 45, pp. 1355-1362, 1998.

[178] A. Ohnishi, P. C. O'Brien, H. Okazaki, and P. J. Dyck, "Morphometry of myelinated fibers of fasciculus gracilis of man," *Journal of the Neurological Sciences,* vol. 27, pp. 163-172, 1976.

[179] P. Kreis and S. Fishman, *Spinal cord stimulation implantation: percutaneous implantation techniques*, 1 ed. New York: Oxford University Press, 2009.

[180] D. H. Szarowski, M. D. Andersen, S. Retterer, A. J. Spence, M. Isaacson, H. G. Craighead, *et al.*, "Brain responses to micro-machined silicon devices," *Brain Research*, vol. 983, pp. 23-35, 9/5/ 2003.

[181] A. T. Villavicencio, J.-C. Leveque, L. Rubin, K. Bulsara, and J. P. Gorecki, "Laminectomy versus percutaneous electrode placement for spinal cord stimulation," *Neurosurgery,* vol. 46, p. 399, 2000.

[182] S. R. Cajal, "Structure of the white matter of the spinal cord," in *Texture of the nervous system of man and the vertebrates*. vol. 1, P. Pasik and T. Pasik, Eds., ed: Springer, 1999, pp. 263-307.

[183] D. S. Tuch, V. J. Wedeen, A. M. Dale, J. S. George, and J. W. Belliveau, "Conductivity tensor mapping of the human brain using diffusion tensor MRI," *Proceedings of the National Academy of Sciences,* vol. 98, pp. 11697-11701, September 25, 2001 2001.

[184] T. E. J. Behrens, S. N. Sotiropoulos, and S. Jbabdi, "Chapter 19 - MR Diffusion Tractography," in *Diffusion MRI (Second Edition)*, H. Johansen-Berg and T. E. J. Behrens, Eds., ed San Diego: Academic Press, 2014, pp. 429-451.

[185] K. K. Seunarine and D. C. Alexander, "Chapter 6 - Multiple Fibers: Beyond the Diffusion Tensor," in *Diffusion MRI (Second Edition)*, H. Johansen-Berg and T. E. J. Behrens, Eds., ed San Diego: Academic Press, 2014, pp. 105-123.

[186] S. Mori and J.-D. Tournier, "Chapter 8 - Moving Beyond DTI: High Angular Resolution Diffusion Imaging (HARDI)," in *Introduction to Diffusion Tensor Imaging (Second Edition)*, S. M.-D. Tournier, Ed., ed San Diego: Academic Press, 2014, pp. 65-78.

[187] S. Mori and J.-D. Tournier, "Chapter 9 - Fiber-Tracking: 3-Dimensional Tract Reconstruction," in *Introduction to Diffusion Tensor Imaging (Second Edition)*, S. M.-D. Tournier, Ed., ed San Diego: Academic Press, 2014, pp. 79-96.

[188] E. A. Kiyatkin, "Brain Hyperthermia During Physiological and Pathological Conditions: Causes, Mechanisms, and Functional Implications," *Current Neurovascular Research,* vol. 1, pp. 77-90, 2004.

[189] J. Viventi, D.-H. Kim, L. Vigeland, E. S. Frechette, J. A. Blanco, Y.-S. Kim, *et al.*, "Flexible, foldable, actively multiplexed, high-density electrode array for mapping brain activity in vivo," *Nat Neurosci,* vol. 14, pp. 1599-1605, 2011.

[190] R. Plonsey, "Reciprocity Applied to Volume Conductors and the ECG," *Bio-medical Electronics, IEEE Transactions on,* vol. 10, pp. 9-12, 1963.

[191] D. A. Robinson, "The electrical properties of metal microelectrodes," *Proceedings of the IEEE,* vol. 56, pp. 1065-1071, 1968.

[192] A. Priori, G. Foffani, L. Rossi, and S. Marceglia, "Adaptive deep brain stimulation (aDBS) controlled by local field potential oscillations," *Experimental Neurology,* vol. 245, pp. 77-86, 2013.

[193] D. Humphrey and E. Schmidt, "Extracellular Single-Unit Recording Methods," in *Neurophysiological Techniques*. vol. 15, A. Boulton, G. Baker, and C. Vanderwolf, Eds., ed: Humana Press, 1991, pp. 1-64.

[194] R. Rieger, D. Pal, J. Taylor, C. Clarke, P. Langlois, and N. Donaldson, "10-channel very low noise ENG amplifier system using CMOS technology," in *Circuits and Systems, 2005. ISCAS 2005. IEEE International Symposium on*, 2005, pp. 748-751 Vol. 1.

[195] J. Sacristan and M. T. Oses, "Low noise amplifier for recording ENG signals in implantable systems," in *Circuits and Systems, 2004. ISCAS '04. Proceedings of the 2004 International Symposium on*, 2004, pp. IV-33-6 Vol.4.

[196] G. Buzsáki, C. A. Anastassiou, and C. Koch, "The origin of extracellular fields and currents — EEG, ECoG, LFP and spikes," *Nat Rev Neurosci,* vol. 13, pp. 407-420, 06//print 2012.

[197] G. Buzsáki and A. Draguhn, "Neuronal Oscillations in Cortical Networks," *Science,* vol. 304, pp. 1926-1929, June 25, 2004 2004.

[198] J. B. Johnson, "Thermal Agitation of Electricity in Conductors," *Physical Review,* vol. 32, pp. 97-109, 1928.

[199] M. B. I. Reaz, M. S. Hussain, and F. Mohd-Yasin, "Techniques of EMG signal analysis: detection, processing, classification and applications," *Biological Procedures Online,* vol. 8, pp. 11-35, 2006/12/01 2006.

[200] J. Perez-Orive and D. M. Durund, "Modeling study of peripheral nerve recording selectivity," *Rehabilitation Engineering, IEEE Transactions on,* vol. 8, pp. 320-329, 2000.

[201] M. A. Schiefer, R. J. Triolo, and D. J. Tyler, "A Model of Selective Activation of the Femoral Nerve With a Flat Interface Nerve Electrode for a Lower Extremity Neuroprosthesis," *Neural Systems and Rehabilitation Engineering, IEEE Transactions on,* vol. 16, pp. 195-204, 2008.

[202] M. Rahal, J. Taylor, and N. Donaldson, "The effect of nerve cuff geometry on interference reduction: a study by computer modeling," *Biomedical Engineering, IEEE Transactions on,* vol. 47, pp. 136-138, 2000.

[203] M. Rahal, J. Winter, J. Taylor, and N. Donaldson, "An improved configuration for the reduction of EMG in electrode cuff recordings: a theoretical approach," *Biomedical Engineering, IEEE Transactions on,* vol. 47, pp. 1281-1284, 2000.

[204] B. Sadeghlo, "Design of a Peripheral Nerve Electrode for Improved Neural Recording of the Cervical Vagus Nerve," Masters of Applied Science, Department of Electrical & Computer Engineering, University of Toronto, Toronto, 2013.

[205] A. Gilletti and J. Muthuswamy, "Brain micromotion around implants in the rodent somatosensory cortex," *Journal of Neural Engineering,* vol. 3, p. 189, 2006.

[206] M. R. Neuman, "Biopotential Electrodes," in *The Biomedical Engineering Handbook*, D. J. Bronzino, Ed., ed Boca Raton: CRC Press, 2000.

[207] L. A. Geddes and R. Roeder, "Criteria for the selection of materials for implanted electrodes," *Ann Biomed Eng,* vol. 31, pp. 879-90, Jul-Aug 2003.

[208] J. D. Stroncek and W. M. Reichert, "Overview of Wound Healing in Different Tissue Types," in *Indwelling Neural Implants: Strategies for Contending with the In Vivo Environment*, W. M. Reichert, Ed., ed Boca Raton: CRS Press, 2007, pp. 3-38.

[209] J. M. Anderson, "BIOLOGICAL RESPONSES TO MATERIALS," *Annual Review of Materials Research,* vol. 31, pp. 81-110, 2001.

[210] S. Sunderland, "Nerve grafting and related methods of nerve repair," *Nerve Injuries and Their Repair: A Critical Appraisal,* pp. 467-497, 1991.

[211] M. Norenberg, "The reactive astrocyte," *The Role of Glia in Neurotoxicity,* vol. 2, pp. 73-93, 2005.

[212] J. Silver and J. H. Miller, "Regeneration beyond the glial scar," *Nat Rev Neurosci,* vol. 5, pp. 146-156, 02//print 2004.

[213] J. N. Turner, W. Shain, D. H. Szarowski, M. Andersen, S. Martins, M. Isaacson, *et al.*, "Cerebral Astrocyte Response to Micromachined Silicon Implants," *Experimental Neurology,* vol. 156, pp. 33-49, 3// 1999.

[214] W. M. Grill and J. T. Mortimer, "Neural and connective tissue response to long-term implantation of multiple contact nerve cuff electrodes," *J Biomed Mater Res,* vol. 50, pp. 215-26, May 2000.

[215] M. M. Lowery, R. F. Weir, and T. A. Kuiken, "Simulation of Intramuscular EMG Signals Detected Using Implantable Myoelectric Sensors (IMES)," *Biomedical Engineering, IEEE Transactions on,* vol. 53, pp. 1926-1933, 2006.

[216] M. A. Moffitt and C. C. McIntyre, "Model-based analysis of cortical recording with silicon microelectrodes," *Clinical Neurophysiology,* vol. 116, pp. 2240-2250, 2005.

[217] D. J. Edell, V. V. Toi, V. M. McNeil, and L. D. Clark, "Factors influencing the biocompatibility of insertable silicon microshafts in cerebral cortex," *Biomedical Engineering, IEEE Transactions on,* vol. 39, pp. 635-643, 1992.

[218] K. A. Ludwig, J. D. Uram, J. Yang, D. C. Martin, and D. R. Kipke, "Chronic neural recordings using silicon microelectrode arrays electrochemically deposited with a poly(3,4-ethylenedioxythiophene) (PEDOT) film," *Journal of Neural Engineering,* vol. 3, p. 59, 2006.

[219] D. R. Merrill and P. A. Tresco, "Impedance characterization of microarray recording electrodes in vitro," *Biomedical Engineering, IEEE Transactions on,* vol. 52, pp. 1960-1965, 2005.

[220] G. C. McConnell, H. D. Rees, A. I. Levey, C. A. Gutekunst, R. E. Gross, and R. V. Bellamkonda, "Implanted neural electrodes cause chronic, local inflammation that is correlated with local neurodegeneration," *J Neural Eng,* vol. 6, p. 056003, Oct 2009.

[221] W. He and R. V. Bellamkonda, "A Molecular Perspective on Understanding and Modulating the Performance of Chronic Central Nervous Sytem (CNS) Recording Electrodes," in *Indwelling Neural Implants: Strategies for Contending with the In Vivo Environment*, W. M. Reichert, Ed., ed Boca Raton: CRC Press, 2007, pp. 151-175.

[222] T. Lefurge, E. Goodall, K. Horch, L. Stensaas, and A. Schoenberg, "Chronically implanted intrafascicular recording electrodes," *Annals of Biomedical Engineering,* vol. 19, pp. 197-207, 1991/03/01 1991.

[223] G. L. Pearson, W. T. Read Jr, and W. L. Feldmann, "Deformation and fracture of small silicon crystals," *Acta Metallurgica,* vol. 5, pp. 181-191, 4// 1957.

[224] A. K. Ommaya, "Mechanical properties of tissues of the nervous system," *Journal of Biomechanics,* vol. 1, pp. 127-138, 7// 1968.

[225] X. Cui and D. C. Martin, "Electrochemical deposition and characterization of poly(3,4-ethylenedioxythiophene) on neural microelectrode arrays," *Sensors and Actuators B: Chemical,* vol. 89, pp. 92-102, 3/1/ 2003.

[226] P. M. George, A. W. Lyckman, D. A. LaVan, A. Hegde, Y. Leung, R. Avasare, *et al.*, "Fabrication and biocompatibility of polypyrrole implants suitable for neural prosthetics," *Biomaterials,* vol. 26, pp. 3511-3519, 6// 2005.

[227] J. Yang, D. H. Kim, J. L. Hendricks, M. Leach, R. Northey, and D. C. Martin, "Ordered surfactant-templated poly(3,4-ethylenedioxythiophene) (PEDOT) conducting polymer on microfabricated neural probes," *Acta Biomaterialia,* vol. 1, pp. 125-136, 1// 2005.

[228] K. A. Ludwig, N. B. Langhals, M. D. Joseph, S. M. Richardson-Burns, J. L. Hendricks, and D. R. Kipke, "Poly(3,4-ethylenedioxythiophene) (PEDOT) polymer coatings facilitate smaller neural recording electrodes," *Journal of Neural Engineering,* vol. 8, p. 014001, 2011.

[229] A. W. Bridges and A. J. García, "Biocompatibility of Implanted Diabetes Devices: Part 2: Anti-Inflammatory Polymeric Coatings for Implantable Biomaterials and Devices," *Journal of diabetes science and technology (Online),* vol. 2, p. 984, 2008.

[230] R. Wadhwa, C. F. Lagenaur, and X. T. Cui, "Electrochemically controlled release of dexamethasone from conducting polymer polypyrrole coated electrode," *Journal of Controlled Release,* vol. 110, pp. 531-541, 2/21/ 2006.

[231] D.-H. Kim, M. Abidian, and D. C. Martin, "Conducting polymers grown in hydrogel scaffolds coated on neural prosthetic devices," *Journal of Biomedical Materials Research Part A,* vol. 71A, pp. 577-585, 2004.

[232] J. M. Anderson and M. S. Shive, "Biodegradation and biocompatibility of PLA and PLGA microspheres," *Advanced Drug Delivery Reviews,* vol. 64, Supplement, pp. 72-82, 12// 2012.

[233] T. D. B. Nguyen-Vu, H. Chen, A. M. Cassell, R. Andrews, M. Meyyappan, and J. Li, "Vertically Aligned Carbon Nanofiber Arrays: An Advance toward Electrical–Neural Interfaces," *Small,* vol. 2, pp. 89-94, 2006.

[234] E. de Asis, Jr., T. D. B. Nguyen-Vu, P. Arumugam, H. Chen, A. Cassell, R. Andrews, *et al.*, "High efficient electrical stimulation of hippocampal slices with vertically aligned carbon nanofiber microbrush array," *Biomedical Microdevices,* vol. 11, pp. 801-808, 2009/08/01 2009.

[235] E. d. Asis, Andrews, R.J., Li, J., *Nanomedicine and the Nervous System*. New York: CRC Press, 2012.

[236] S. K. Smart, A. I. Cassady, G. Q. Lu, and D. J. Martin, "The biocompatibility of carbon nanotubes," *Carbon,* vol. 44, pp. 1034-1047, 5// 2006.

[237] P. R. Kennedy, "The cone electrode: a long-term electrode that records from neurites grown onto its recording surface," *Journal of Neuroscience Methods,* vol. 29, pp. 181-193, 1989.

[238] P. R. Kennedy, S. S. Mirra, and R. A. E. Bakay, "The cone electrode: Ultrastructural studies following long-term recording in rat and monkey cortex," *Neuroscience Letters,* vol. 142, pp. 89-94, 1992.

[239] P. Kennedy, "Reliable neural interface: The first quarter century of the Neurotrophic Electrode," in *Engineering in Medicine and Biology Society (EMBC), 2012 Annual International Conference of the IEEE*, 2012, pp. 3332-3335.

[240] G. Häggqvist, "Analyse der faserverteilung in einem Rückenmarkquerschnitt (Th 3)," *Z Mikrosk Anat Forsch,* vol. 39, pp. 1-34, 1936.

[241] M. R. Dimitrijevic, J. Faganel, P. C. Sharkey, and A. M. Sherwood, "Study of sensation and muscle twitch responses to spinal cord stimulation," *Disability and Rehabilitation,* vol. 2, pp. 76-81, 1980.

[242] B. Nashold, G. Somjen, and H. Friedman, "Paresthesias and EEG potentials evoked by stimulation of the dorsal funiculi in man," *Experimental Neurology,* vol. 36, pp. 273-287, 1972.

[243] R. A. Davidoff, "The dorsal columns," *Neurology,* vol. 39, p. 1377, October 1, 1989 1989.

[244] J. C. Brumberg, L. G. Nowak, and D. A. McCormick, "Ionic Mechanisms Underlying Repetitive High-Frequency Burst Firing in Supragranular Cortical Neurons," *The Journal of Neuroscience,* vol. 20, pp. 4829-4843, July 1, 2000 2000.

Biography

Bryan Howell was born in McAllen, TX, USA, in 1986. He received the B.S. degree (with honors) in biomedical engineering and the Minor in mathematics from The University of Michigan (Ann Arbor, MI, USA) in 2009, and obtained the Ph.D. degree in biomedical engineering at Duke University (Durham, NC, USA) in 2015. Bryan has published the following peer-reviewed journal articles and book chapters:

Journal Articles:

Howell B, Huynh B, Grill WM. (2015) Design and in vivo evaluation of optimal deep brain stimulation electrodes. Journal of Neural Engineering; in review.

Howell B, Lad SP, Grill WM. (2015) Evaluation of intradural stimulation efficiency and selectivity in a computational model of spinal cord stimulation. PloS ONE 9 (12): e114938. doi:10.1371/journal.pone.0114938

Howell B, Grill WM. (2014) Evaluation of high-perimeter electrode designs for deep brain stimulation. Journal of Neural Engineering; 11(4): 1741-2560.

Howell B, Naik S, Grill WM. (2014) Influences of interpolation error, electrode geometry, and the electrode-tissue interface on models of electric fields produced by deep brain stimulation. Biomedical Engineering, IEEE Transactions on; 61(2): 297-307.

Jovic A, **Howell B**, Cote M, et al. (2010) Phase-locked signals elucidate circuit architecture of an oscillatory pathway. PloS Computational Biology; 6(12)

Jovic A, **Howell B**, Takayama S. (2009) Timing is everything: using fluidics to understand the role of temporal dynamics in cellular systems. Microfluidics and Nanofluidics; 6(6): 717-729.

Book Chapters:

Howell B, Grill WM. (2015) Design of electrodes for stimulation and recording. Kilgore K., ed. Implantable Neuroprostheses for Restoring Function; Woodhead Publishing, Oxford, in press.

In addition, while at Duke University, Bryan obtained the following awards:

Recipient, the National Institutes of Health Predoctoral (F31) Kirschstein Fellowship, 2012-2015

Dean's Graduate Fellowship, 2009-2014